

UCSF

UC San Francisco Electronic Theses and Dissertations

Title

Opposing forces and torques provide robustness in the human mitotic spindle

Permalink

<https://escholarship.org/uc/item/3dg9v3v1>

Author

Neahring, Lila

Publication Date

2023

Peer reviewed|Thesis/dissertation

Opposing forces and torques provide robustness in the human mitotic spindle

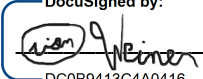
by
Lila Neahring

DISSERTATION
Submitted in partial satisfaction of the requirements for degree of
DOCTOR OF PHILOSOPHY

in
Developmental and Stem Cell Biology

in the
GRADUATE DIVISION
of the
UNIVERSITY OF CALIFORNIA, SAN FRANCISCO

Approved:


DocuSigned by:

DC0B9413C4A0416... Orion Weiner
Chair

DocuSigned by:

Wallace Marshall

DocuSigned by:

Jeffrey Bush

DocuSigned by:

8305715E0D454DC... Sophie Dumont

Committee Members

Dedicated to my parents, Jenni Neahring and Rick Neahring

Acknowledgements

I am forever grateful to the many scientists, friends, and family members that I relied upon throughout my PhD. First, I thank my advisor Sophie Dumont for her truly world-class mentorship. Sophie has guided me at every step as I learned how to frame questions, handle risks and setbacks, communicate my findings, and develop independence. I thank her for her unwavering support and faith in me.

I am also grateful to the members of the Dumont Lab, past and present, who have taught, inspired, and encouraged me. Thank you to Mary Elting, Jon Kuhn, Christina Hueschen, Alex Long, Andrea Serra Marques, Josh Guild, Pooja Suresh, Meelad Amouzgar, Manuela Richter, Miquel Rosas Salvans, Renaldo Sutanto, Ronja Houtekamer, Megan Chong, Nathan Cho, Carly Garrison, Caleb Rux, Vanna Tran, Zack Mullin-Bernstein, Jinghui Tao, Matt Keefe, Tania Singh, Trase Aguigam, and Camille Derderian. Collaborating, traveling, and relaxing with the lab have provided many of the highlights of graduate school.

My thesis committee members Orion Weiner, Jeff Bush, and Wallace Marshall provided invaluable experimental and career planning advice across many years. I thank them for their encouragement and the time they invested in me. Thank you also to the Developmental & Stem Cell Biology student community, current and former DSCB directors Jeremy Reiter, Robert Blelloch, and Todd Nystul, and program coordinator Demian Sainz for making UCSF such a welcoming and fun place to be a graduate student.

I was fortunate to work with many wonderful collaborators during graduate school. I thank Pranav Vyas, Vivek Prakash, Scott Coyle, Andrei Goga, Ahmet Yildiz, Yifei He,

Jon Fernandes, Radhika Subramanian, Srigokul Upadhyayula, Gaoxiang Liu, Shalin Mehta, Ivan Ivanov, Talon Chandler, Sabine Petry, and Venecia Valdez for sharing their expertise and their time. I am deeply grateful to Manu Prakash for welcoming me into his lab for many months and sharing his enthusiasm for curiosity-driven science. I am still fascinated by the research questions we worked on together, and they serve as a reminder of the big open questions that are alive and well in biology.

I am indebted to Phil Beachy and Ben Myers, my PI and postdoc mentor while I was an undergraduate at Stanford University, for kindling my love of science. Phil and Ben saw potential in me long before I deserved their confidence, and their advice guided me through the process of applying to and navigating graduate school.

My sister Aja has celebrated my successes and helped me through many difficult moments over the past years. I thank the Alejandre family for providing me another home, and for showing me so many examples of lives well lived. Jakob Alejandre, my husband, has been by my side through all the highs and lows of college and graduate school, and brings joy to everything I do. I am more grateful than I can express for his love and support.

Finally I thank my parents, Rick and Jenni, for their unconditional love and for all the sacrifices they made for me. My parents gave me a world full of possibility, and instilled in me the desire to make it a better place.

Contributions

Chapter 1 of this dissertation contains material that was previously published: Valdez, V. A.*, Neahring, L.*, Petry, S.*, and Dumont, S.* (2023). Mechanisms underlying spindle assembly and robustness. *Nature Reviews Molecular Cell Biology* (*equal contribution). I wrote the sections of the review article and created the figures that were adapted in Chapter 1, under the supervision of Sophie Dumont, PhD. Co-authors Venecia Valdez and Sabine Petry, PhD (Princeton University) contributed equally by writing other sections, creating other figures, and in discussing and editing the entire review.

Chapter 2 of this dissertation is a reprint of work that was previously published: Neahring, L., Cho, N. H., and Dumont, S. (2021). Opposing motors provide mechanical and functional robustness in the human spindle. *Developmental Cell* 56(21):3006-3018. I performed the experiments described herein, analyzed the data, and wrote the manuscript under the guidance of Sophie Dumont, PhD.

Chapter 3 of this dissertation comprises unpublished material that is a work in progress. I performed the studies described in this chapter under the guidance of Sophie Dumont, PhD. I collaborated with Gaoxiang Liu, PhD, Srigokul Upadhyayula, PhD (UC Berkeley) and Caleb Rux (UCSF) to perform the lattice light sheet imaging. I also collaborated with Ivan Ivanov, PhD, Talon Chandler, PhD, and Shalin Mehta, PhD (Chan Zuckerberg Biohub) on preliminary polarization microscopy experiments not included here. Yifei He (UC Berkeley), Ahmet Yildiz, PhD (UC Berkeley), and Radhika Subramanian, PhD (Harvard) also contributed in vitro experiments, not included here, to this project. Nathan Cho (UCSF) assisted with experiments not included here in this project.

Chapter 4 of this dissertation contains unpublished material that is a work in progress: Sutanto, R.*, Neahring, L.*, Serra Marques, A., Kilinc, S., Goga, A., and Dumont, S. The oncogene cyclin D1 promotes bipolar spindle integrity under compressive force. (Manuscript in preparation, *equal contribution). I performed preliminary validation and optimization experiments, helped to design the experiments presented here, performed data analysis, and wrote the manuscript under the guidance of Sophie Dumont, PhD and Andrei Goga, PhD. Andrea Serra Marques, PhD and Renaldo Sutanto performed immunofluorescence and live imaging experiments, and Seda Kilinc, PhD provided technical advice.

Opposing forces and torques provide robustness in the human mitotic spindle

Lila Neahring

Abstract

At each cell division, nanometer-scale motors and microtubules give rise to the micron-scale spindle. Although the biophysical properties of many individual motors are well studied, it is not fully understood how these molecular components push, pull, and twist microtubules to build a spindle with emergent mechanics and robust function, or how these processes are subverted in disease. We first focus on the contractile motor dynein and the extensile motor Eg5. Although these motors are individually required to build the human spindle, typical bipolar spindles form when both are inhibited together, raising the question of what roles these opposing motors play. Using quantitative live imaging, we find that co-inhibiting Eg5 and dynein's targeting factor NuMA generates spindles that attain a normal metaphase shape and undergo anaphase. However, these spindles exhibit reduced microtubule dynamics, mechanical fragility, and error-prone chromosome segregation. Thus, although these opposing motors are not required for spindle assembly, they are essential to the spindle's mechanical and functional robustness. Unexpectedly, we also find that spindles lacking NuMA/dynein and Eg5 activity display strong left-handed twist at anaphase, leading us to ask how molecular torques generated by chiral mitotic motors are balanced to regulate global spindle twist. We find that the midzone motors KIF4A and MKLP1 contribute to left-handed twist at anaphase, as does the actin cytoskeleton. Depletion of LGN or dynein, which generate force at the cell cortex, counteracts these left-handed torques. Thus, competing torques are balanced to

establish the spindle's global twist, and torques acting from the outside of the spindle balance those generated within it. Finally, we investigate how oncogenic transformation affects spindle architecture and mechanics. We find that cyclin D1 overexpression increases the incidence of spindles with extra poles, centrioles, and chromosomes, but that it also protects spindle poles from fracturing under compressive forces. We propose that cyclin D1 overexpression may be adaptive in stiff solid tumors, contributing to its prevalence in cancer by allowing continued proliferation in mechanically challenging environments. Together, this work reveals design principles by which the spindle achieves robustness, and how they are rewired in disease.

Table of Contents

Chapter 1: Introduction.....	1
Spindle assembly: From molecular parts to robust machine.....	2
Molecular components of the spindle.....	3
Architectural features of the spindle.....	4
Emergent properties of the spindle.....	6
Objectives of thesis.....	12
Figures and figure legends.....	14
Chapter 2: Opposing motors provide mechanical and functional robustness in the human spindle.....	17
Abstract.....	18
Introduction.....	19
Results.....	22
Discussion.....	30
Figures and figure legends.....	36
Supplemental figures and figure legends.....	47
Materials and methods.....	54
Acknowledgements.....	64
Chapter 3: Torques within and outside the human spindle balance twist at anaphase.....	65
Abstract.....	66
Introduction.....	67
Results.....	70

Discussion	76
Figures and figure legends	80
Supplemental figures and figure legends	87
Materials and methods	89
Acknowledgements	94
Chapter 4: The oncogene cyclin D1 promotes bipolar spindle integrity under compressive force	95
Abstract	96
Introduction	97
Results	100
Discussion	103
Figures and figure legends	106
Materials and methods	111
Acknowledgements	115
Chapter 5: Conclusions and future directions	116
References	122

List of Figures

Chapter 1

- Figure 1.1.** Overview of spindle assembly, from molecular parts to cellular-scale properties. 14
- Figure 1.2.** Motor-driven stresses in the spindle. 16

Chapter 2

- Figure 2.1.** Eg5 inhibition allows turbulent spindles to recover bipolarity and progress to anaphase. 37
- Figure 2.2.** Doubly inhibited spindles are sensitized to changes in microtubule organization, dynamics, and motor-based forces. 38
- Figure 2.3.** Microtubule organization and dynamics are disrupted in doubly inhibited spindles. 40
- Figure 2.4.** Doubly inhibited spindles are structurally unstable in response to mechanical force. 42
- Figure 2.5.** Spindles with reduced opposing motor activity exhibit twist and functional defects in anaphase. 45
- Figure 2.6.** Model for opposing active stresses providing mechanical and functional robustness to the human spindle. 46
- Figure 2.7.** Additional analysis of NuMA- and Eg5-doubly inhibited spindles, related to Figure 2.1. 48
- Figure 2.8.** Validation of RNAi depletions, related to Figure 2.2. 49
- Figure 2.9.** Dynein- and Eg5-doubly inhibited spindles, but not Eg5-inhibited spindles, are mechanically fragile, related to Figure 2.4. 50

Figure 2.10. Comparison of anaphase movements in control and doubly inhibited spindles, related to Figure 2.5.	51
Figure 2.11. Additional analysis of spindle twist in control and doubly inhibited spindles, related to Figure 2.5.	52
Chapter 3	
Figure 3.1. MCF10A cells exhibit high baseline twist that peaks in late metaphase and anaphase.	80
Figure 3.2. The midzone motors KIF4A and MKLP1 redundantly promote left-handed twist in the anaphase spindle.	82
Figure 3.3. The cortical force-generating machinery counteracts left-handed twist in the anaphase spindle.	83
Figure 3.4. The actin cytoskeleton, but not actomyosin contractility, are required for left-handed twist at anaphase.	85
Figure 3.5. Validation of RNAi depletions and drug treatments.	88
Chapter 4	
Figure 4.1. Characterization of cells overexpressing cyclin D1.	106
Figure 4.2. Cyclin D1 overexpression promotes aberrant spindle architectures.	108
Figure 4.3. The cell compression assay is quantitatively reproducible.	109
Figure 4.4. Cyclin D1 overexpression protects against spindle fracture during compression.	110

Chapter 1: Introduction

Spindle assembly: From molecular parts to robust machine

The spindle is the microtubule-based machine that divides the genome at each cell division, a process that has fascinated biologists for over a century [1]. During assembly of the mammalian spindle, hundreds of thousands of nanometer-scale proteins interact to give rise to a cellular-scale ensemble. While a nearly complete inventory of the spindle's molecular components has been achieved [2], how these components give rise to the spindle's emergent mechanical and functional properties that are more than the sum of their parts (i.e. spatially varying viscoelasticity, accurate chromosome segregation) remains incompletely understood.

In addition to providing an excellent case study for the principles of self-organization, the spindle is also fundamentally important to human health. There are an estimated 10^{16} cell divisions in a human lifespan [3], yet errors in chromosome segregation can lead to birth defects [4] and cancer [5, 6]. Thus, it is critical that chromosomes are faithfully segregated despite biochemical and mechanical noise, such as variations in gene expression or forces from surrounding cells. Indeed, the spindle is robust to a wide variety of experimental perturbations: it can rapidly re-establish its shape and size after laser ablation of microtubule bundles [7-9], deformation with a microneedle [10], and even after complete spindle depolymerization with nocodazole followed by drug washout [11].

In this dissertation, I ask which molecular components give rise to the spindle's emergent robustness, and how these mechanisms are co-opted in disease. In Chapter 2, I investigate the roles of opposing contractile and extensile motor activity in establishing the spindle's structural integrity and accurate function. In Chapter 3, I describe molecular

torque generators that are balanced to set the spindle's global twist. In Chapter 4, I ask how the oncogene cyclin D1 modifies spindle architecture and mechanics to model spindle adaptations in a disease state. Finally, in Chapter 5, I discuss open questions about the spindle's emergent robustness.

Molecular components of the spindle

At the start of mitosis, the interphase microtubule network is broken down into tubulin subunits, and thousands of microtubules must be rapidly reformed to build the spindle (Figure 1.1A). Several pathways of spatially regulated microtubule nucleation are employed to accomplish this task, including centrosome-, microtubule-, and kinetochore-mediated nucleation pathways. Once nucleated, spindle microtubules are organized into structural modules that fulfill distinct roles such as generating force at kinetochores (k-fibers), providing structural stability (bridging fibers and other non-kinetochore microtubules) and positioning the spindle (astral microtubules). Microtubules must also be assembled into a bipolar structure with two focused poles to guide chromosome segregation into two daughter cells (Figure 1.1B).

This modular organization is mediated by a variety of motor and non-motor microtubule-associated proteins (MAPs) [12], which bundle, slide and focus microtubules. Mitotic motors include cytoplasmic dynein and members of several kinesin families. Many of these motors bind to microtubules through both a motor domain and a second microtubule-binding domain, allowing them to bridge two microtubules and thereby crosslink and slide them in an ATP-dependent manner. Non-motor MAPs include passive microtubule crosslinkers, which consume no energy but function in an ATP-independent

fashion to regulate bundling, elasticity, and friction within the spindle. Microtubule polymerases and depolymerases also localize to specific structural modules, fine-tuning the dynamics of these modules as they arise during spindle assembly.

Architectural features of the spindle

Focused spindle poles

Motors and MAPs generate several key architectural features of the spindle, in addition to the structural modules described above. Microtubules belonging to several classes (including kinetochore microtubules, non-kinetochore microtubules, and astral microtubules) are focused into a point on each side of the spindle, and these poles serve as a regulatory hub for microtubule nucleation and dynamics. Although spindle poles contain centrosomes in most cells, the formation of focused poles in acentrosomal oocytes [13-15] and somatic cells after centrosome ablation [16-21] has established that centrosomes are not necessary for the formation of focused spindle poles. Instead, pole focusing is driven by minus-end-directed motors that are able to dwell at microtubule minus ends and transport these minus end cargos along neighboring microtubules — the same mechanism that forms microtubule asters in vitro [22].

Dynein and its cofactors dynactin and NuMA are key players in pole focusing, and their inhibition leads to unfocused barrel-shaped or turbulent spindles [14, 23-28]. NuMA localizes to minus ends, where it recruits dynactin and dynein to walk along neighboring microtubules, facilitating the end-dwelling behavior [29] (Figure 1.2). The large and multifunctional NuMA likely contributes to pole focusing in many ways: in addition to localizing dynein, it is a putative activating adaptor of dynein motility [30, 31] and may

have auxiliary roles in organizing microtubules via passive crosslinking [32] and/or phase separating at spindle poles [33, 34]. The kinesin-14 family of motors, including *Xenopus* XCTK2, *Drosophila* Ncd, and human HSET, also contributes to pole focusing, although the exact mechanisms by which these motors organize spindle poles remain unclear. The relative importance of dynein and kinesin-14 varies between species, with Ncd playing a dominant role in *Drosophila* [26] whereas HSET depletion has only mild phenotypes in human mitotic spindles [35, 36].

Functionally, poles and the motors that focus them are important in concentrating minus end regulatory factors like γ -tubulin. As γ -tubulin accumulates during pole maturation, it enhances microtubule nucleation and stabilizes the focused pole, even in acentrosomal spindles that initially lack nucleation at poles [37, 38]. Pole focusing also functions to maintain a steady-state spindle shape, thereby ensuring that growing and shrinking microtubules are confined to the spindle region without interacting with organelles or generating cytoplasmic flows [27].

Spindle bipolarity

The assembly of a spindle with two poles is critical to segregate chromosomes into two daughter cells. Monopolar, aster-shaped spindles are often the result of failed spindle assembly, and multipolar spindles are associated with genomic instability and cancer [39]. The bipolar homotetrameric kinesin-5 motors (Eg5 in humans) play a central role in establishing spindle bipolarity in both acentrosomal and centrosome-containing spindles [40, 41], due to their ability to crosslink and slide antiparallel microtubules apart [42, 43] (Figure 1.2).

In prophase, spindle bipolarity is templated by the sliding apart of duplicated centrosomes to opposite sides of the nucleus. This movement is driven by the pulling forces of dynein attached to the nuclear envelope [44] and by Eg5-mediated antiparallel sliding of centrosomal microtubules. After nuclear envelope breakdown, microtubules from opposite centrosomes form additional antiparallel overlaps on which Eg5 can localize. Nascent k-fibers also promote bipolarity, potentially due to an outward pushing force on centrosomes from k-fiber polymerization at kinetochores [45, 46]. In metaphase, spindles in many mammalian cell types remain bipolar even if Eg5 is inhibited due to the partially redundant activity of the kinesin-12 KIF15 [47-50], which allows maintenance though not initial generation of spindle bipolarity. Thus, the cooperation of multiple motor-based and nucleation pathways between prophase and metaphase promotes the robust assembly of a bipolar spindle, setting the stage for chromosome biorientation and equal segregation into two daughter cells.

Emergent properties of the spindle

The spindle exhibits many cellular-scale emergent properties that are qualitatively different from those of its individual components and that enable the spindle to segregate chromosomes accurately. These include dynamic features such as microtubule flux and continuous self-repair, mechanical features such as spatially varying viscoelasticity, and architectural features such as helical twist.

Poleward flux

Poleward flux is a phenomenon in which spindle microtubules continuously treadmill towards poles, undergoing net polymerization at plus ends and depolymerization at minus ends [51]. Eg5 was the first known driver of flux, identified in *Xenopus* egg extract [52], but it plays only a minor role in flux in mammalian spindles [53, 54]. Instead, flux in mammalian spindles appears to be driven by Eg5 and KIF15 acting in coordination with CENP-E in prometaphase and KIF4A in metaphase, with the depolymerase KIF2A acting at minus ends and kinetochore-localized CLASPs promoting plus-end polymerization [54, 55]. These motors exert poleward forces on non-KMTs, which are only partially transmitted to k-fibers through crosslinkers such as NuMA and HSET [54, 56], explaining why non-KMTs flux faster than k-fibers [37, 54, 57]. While the function of flux is not entirely clear, it appears that flux is required to maintain dynamic kinetochore-microtubule attachments [56, 58], and thus that it supports accurate chromosome segregation in anaphase [56, 58, 59].

Spindle material properties

Although the biophysical properties of microtubules and many individual MAPs are well understood in vitro, far less is known about the material properties of the spindle — its deformation, remodeling and structural failure under force — as an ensemble. The spindle must respond to forces generated both internally (by motors and dynamic microtubules) and externally (by cortical motors and by neighboring cells), and mechanical forces regulate many aspects of cell division including chromosome movement, spindle positioning, and error correction at kinetochores [60-62]. Rheological

studies using microneedles, force-sensing cantilevers and cell confinement have demonstrated that invertebrate, mammalian and *Xenopus* egg extract spindles are stiffer in their long axes compared to their short axes [63-65]. This may be functionally important in permitting efficient longitudinal movements during chromosome congression, oscillation, and segregation, while allowing chromosomes to deform their surroundings laterally. The dynamic and complex microstructure of the spindle also mediates distinct responses at different timescales of force application. In *Xenopus* egg extract spindles, the short axis deforms elastically on short (<10 s) or long (>100 s) timescales but is more viscous on intermediate timescales [66]. On the long axis, stiffness is highest at the pole and equator but the spindle is softer between them [67]. These behaviors allow maximal structural plasticity on the timescale at which chromosomes move through the spindle, with minimal deformability near microtubule connections to chromosomes and poles. Microneedle manipulation of mammalian PtK2 cells has revealed that similar principles of spatially heterogeneous mechanics apply to spindles with prominent k-fibers [10, 68].

The molecular components of the spindle constantly dissipate energy in the form of GTP (microtubule dynamics) and ATP (motor proteins such as dynein), meaning that although the spindle reaches a steady-state structure at metaphase, it does not reach thermodynamic equilibrium. Accordingly, the full complexity of the spindle cannot be fully captured by the rheological models described above. Additional insight into spindle material properties has been gained from active matter theories that model non-equilibrium systems. The microtubule architecture and dynamics of *Xenopus* egg extract spindles have been described by active liquid crystal theory, modelling the spindle as a droplet of microtubules that is shaped by microtubule turnover, mutual alignment, surface

tension and motor-driven active stresses [69]. Active matter theory has also been applied to the human spindle, where the cell membrane provides boundary conditions absent in the *Xenopus* egg extract system. In human cells, unchecked extensile sliding by Eg5 results in the bending and buckling of microtubules against the cell cortex, leading to chaotic, turbulent microtubule networks. This effect is opposed by dynein-mediated contractile stress that allows the spindle to maintain a steady-state shape [27, 70] (Figure 1.2).

Spindle twist

The regulation and function of spindle twist is a new area of research, sparked by a recent report that metaphase human U2OS and HeLa spindles are slightly left-handed on average [71]. Many mitotic motors have an off-axis component to their stepping behavior in vitro, resulting in helical motion around the microtubule track. Since plus-end-directed motors studied thus far have a left-handed bias [72-74] and minus-end-directed motors have a right-handed bias [75-77], how the spindle resists these additive torques to maintain its relatively untwisted global architecture is not known. So far it appears that twist varies between cell types, with HeLa and U2OS cells having more twisted spindles than RPE1 cells [59, 71, 78], and between mitotic stages, peaking in early anaphase [78]. The inhibition of several motors and MAPs, including Eg5, Kif18A, and augmin, each has a small impact on spindle twist, but each contributes to left-handed twist in the expected direction [71, 78]. Notable exceptions are that spindles of the amoeba *Naegleria* are right-handed [79], suggesting that the left-handed bias may not be a highly conserved feature of the spindle across evolution, and that deletion of NuMA results in strong left-handed

twist [59], suggesting that NuMA/dynein motor activity or crosslinking may be important contributors to counteracting left-handed twist. Although the function, if any, of spindle twist remains unknown, a recent study proposed that twist allows the spindle to bear mechanical load along the pole-pole axis (e.g. from neighboring cells) without buckling [78]. Further research is required to determine whether maintaining spindle twist within a specific range is important for spindle function.

Robustness

The spindle can repair itself after a range of experimental perturbations, and several classes of failsafe mechanisms have been identified that allow the spindle to maintain its architecture and accurate function in the face of biochemical and mechanical fluctuations. Redundancy exists in many spindle processes, including microtubule nucleation pathways and motor activities that establish spindle architecture. Several pairs of partially redundant motors cooperate to promote correct spindle architecture. KIF15 maintains bipolarity when Eg5 is inhibited in metaphase [47, 48], and when overexpressed, can fully compensate for Eg5 in bipolar spindle assembly [46, 47]. Further, kinesin-14 motors focus poles in a manner partially redundant with dynein, making the human kinesin-14 HSET nonessential for normal mitosis [35, 36] but important in the context of dynein inhibition [80]. Motor redundancy has important implications for the therapeutic targeting of cell division; for example, KIF15 is essential for the evolution of resistance to Eg5 inhibitors [81].

Robustness in the spindle is also mediated by specialized mechanisms that reinforce and repair key spindle connections at both the plus and minus ends of k-fibers.

The NuMA–dynein–dynactin complex acts at minus ends to anchor k-fibers in the spindle. Not only does this complex transport KMT minus ends poleward during k-fiber formation, it is also sufficient to re-establish k-fiber connections to the poles after acute perturbations such as laser severing [7, 8]. Recent studies have also identified mechanisms that anchor the first few microns near k-fiber plus ends within the spindle microtubule network, protecting kinetochore–microtubule attachments from acute perturbation [10, 82-84]. PRC1 provides short-lived-reinforcement in this region [10, 83], presumably by crosslinking KMTs with nearby antiparallel non-KMTs, thus preventing microtubule pivoting near kinetochores in response to external force supplied by a microneedle [10]. NuMA has also been shown to support k-fiber anchorage near the plus end [84], an effect that may reflect crosslinking between KMTs and the minus ends of short microtubules in the center of the spindle. On the longer (~minutes) timescale, these reinforcements are relaxed [10], allowing spindle remodeling and chromosome movement. Together, these mechanisms ensure that k-fibers remain robustly attached at kinetochores and anchored at poles.

Tension regulates microtubule dynamics at both plus and minus ends, enhancing the spindle's robustness to mechanical perturbation. Tension on microtubules decreases the catastrophe rate and increases rescue frequency of microtubules at purified yeast kinetochores, stabilizing kinetochore-microtubule attachments under force [85, 86]. In microneedle manipulation experiments in newt epithelial cells [87], grasshopper spermatocytes [88], and more recently mammalian PtK2 cells [68], individual k-fibers elongated under applied force, demonstrating that similar principles apply to bundled k-fibers composed of many microtubules. At minus ends, depolymerization is inhibited when

tension is applied to k-fibers either globally via cell compression [64] or individually via a microneedle [68]. The molecular mechanisms underlying these responses remain unknown, and they present an exciting opportunity to identify how the spindle physically and biochemically remodels under force. Collectively, these mechanisms allow the spindle to accommodate local deformations while limiting force propagation in space and time, suggesting a strategy to preserve global architecture and connectivity.

Objectives of thesis

Although the molecular bases of many of the spindle's emergent, cellular-scale properties have begun to be unraveled, conceptual and technical gaps remain in our understanding of spindle self-organization. In this dissertation, I use quantitative live imaging and physical perturbations in human cells to ask how the spindle attains its mechanical and functional robustness, and how these properties are co-opted in disease.

In Chapter 2, I find that the opposing motors NuMA/dynein and Eg5—mediating contractile and extensile stress, respectively—are not required for bipolar spindle architecture, but that they are essential for the spindle's mechanical integrity and accuracy in segregating chromosomes. In Chapter 3, I find that spindle architecture is maintained by opposing torques in addition to opposing stresses in the pole-to-pole axis. Focusing on the anaphase spindle, I show that the spindle contains both factors that promote left-handed helical twist and factors that counteract these torques. Lastly, in Chapter 4, I find that overexpression of the oncogene cyclin D1 protects spindle poles from fracturing under compressive force. This suggests that cyclin D1 may adapt cell

division to stiff tumor environments, and thus that spindle mechanical robustness can serve as a double-edged sword in pathological states.

Together, these studies reveal new design principles at work in spindle self-organization. The spindle is built and maintained by opposing force generators in the pole-to-pole axis as well as opposing torques, and this antagonism between active, energy-consuming motors allows the spindle to respond more effectively to biochemical and mechanical perturbations. Secondly, the spindle's structural integrity can be strengthened by oncogenic transformation, potentially providing a selective advantage to error-prone spindles in altered mechanical environments. These principles may provide insight into the robustness of other force-generating cellular structures.

B) Spatial scales of spindle assembly. Spindle assembly requires formation of microtubules from tubulin dimers. Individual spindle microtubules assemble into structural modules through the action of crosslinkers and motor proteins. The spindle is characterized by emergent properties—characteristics of the ensemble that are not exhibited by its component parts—such as its material properties and poleward microtubule flux.

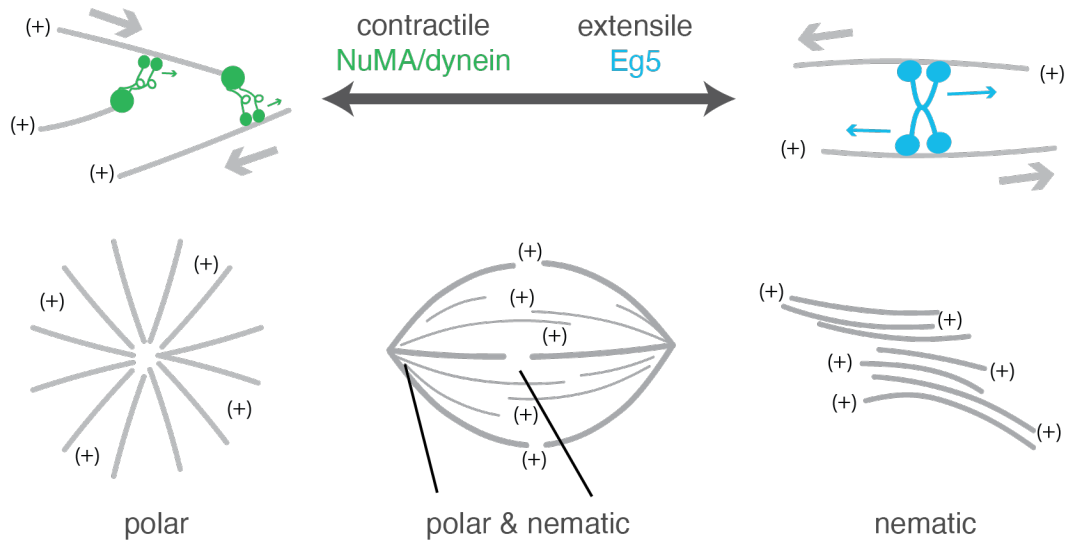


Figure 1.2. Motor-driven stresses in the spindle.

Dynein and its cofactors NuMA and dynactin generate contractile stress in vitro and in the spindle, clustering minus ends together. Eg5 mediates extensile stress, giving rise to nematic motifs of aligned, mixed-polarity microtubules. These opposing motor activities are balanced in bipolar spindles, while an excess of contractile activity leads to monopolar spindles and an excess of extensile sliding produces turbulent microtubule networks.

**Chapter 2: Opposing motors provide mechanical and functional robustness in the
human spindle**

Abstract

At each cell division, the spindle self-organizes from microtubules and motors. In human spindles, the motors dynein and Eg5 generate contractile and extensile stress, respectively. Inhibiting dynein or its targeting factor NuMA leads to unfocused, turbulent spindles and inhibiting Eg5 leads to monopoles, yet bipolar spindles form when both are inhibited together. What, then, are the roles of these opposing motors? Here, we generate NuMA/dynein- and Eg5-doubly inhibited spindles that not only attain a typical metaphase shape and size, but also undergo anaphase. However, these spindles have reduced microtubule dynamics and are mechanically fragile, fracturing under force. Further, they exhibit lagging chromosomes and dramatic left-handed twist at anaphase. Thus, while these opposing motors are not required for spindle shape, they are essential to its mechanical and functional robustness. This work suggests a design principle whereby opposing active stresses provide robustness to force-generating cellular structures.

Introduction

At each cell division, the spindle self-organizes from dynamic microtubules, crosslinkers, and motors [89, 90]. Together, these molecular-scale force generators give rise to a cellular-scale structure with emergent properties such as a steady-state shape in metaphase and the ability to accurately segregate chromosomes at anaphase. The mammalian spindle's molecular components have been extensively cataloged [2], and the biophysical properties of many individual motors are now known. However, it remains poorly understood how combinations of motor activities—many of which act redundantly or in opposition to each other—give rise to the mammalian spindle's emergent architecture, mechanics, and function.

The motors Eg5 and dynein are key determinants of spindle architecture. Both generate directional forces between pairs of microtubules that they crosslink, building distinct cellular-scale motifs that coexist in the spindle's microtubule network. The kinesin-5 Eg5 (KIF11) is a bipolar homotetrameric motor that slides antiparallel microtubules apart, generating extensile stress in the spindle and maintaining pole separation [41, 43, 70]. Conversely, dynein is recruited to microtubule minus ends by its targeting factor NuMA, where it generates contractile stress by carrying minus end cargoes towards the minus ends of neighboring microtubules (Figure 2.1A) [91-93]. The activities of Eg5 and dynein are multifaceted and complex; for example, Eg5 also exerts braking forces in certain velocity regimes and between parallel microtubule pairs [94], and dynein-mediated end-clustering may require cooperative motor accumulation at microtubule minus ends [95]. However, at the length scale of the spindle, these motors have opposing loss-of-function phenotypes that are deleterious for the dividing cell. When Eg5 is inhibited,

spindles form as monopoles with minus ends clustered into a single aster [96], whereas NuMA or dynein deletion leads to turbulent, disordered spindles with no steady-state shape and with microtubule bundles extending against the cell cortex [27].

Despite their importance to spindle architecture, when dynein and Eg5 are co-depleted, human spindles form as typical bipoles [27, 80, 97, 98]. Similar phenomena have been reported in yeast, *Drosophila*, *Xenopus laevis* extract, and pig spindles when the homologous kinesin-5 and the dominant end-clustering motor (dynein or a kinesin-14) are inhibited [11, 99-102]. These observations suggest that the balance of contractile and extensile stress in the spindle is more important than the specific magnitude of these stresses. This raises the question: what are the functions of opposing, energy-consuming motor activities in the spindle if the same structure can be formed without them? Previous work in *Xenopus* extract spindles has suggested a role for opposing activities of dynein and Eg5 in establishing the spindle's microtubule organization, mechanical integrity, and heterogeneity [67, 101, 103], but it is unknown if this applies to other spindles, whose architectures differ and whose mechanics are challenging to probe. In human cells, the primary defect in dynein- and Eg5-doubly inhibited spindles is reported to be in kinetochore-microtubule attachments [80]. However, dynein performs multiple functions at the kinetochore in addition to its role in minus end clustering [104, 105], complicating the interpretation of dynein- and Eg5-doubly inhibited phenotypes in metaphase and limiting their study in anaphase. Thus, antagonistic contractile and extensile stress generation is a highly conserved feature of the spindle, but its mechanical and functional roles throughout the spindle's lifetime remain unclear.

Here, we show that while the opposing motor activities of NuMA/dynein and Eg5 are not required to build the human spindle, they are instead essential to its robustness—the spindle's ability to tolerate mechanical and biochemical fluctuations while maintaining its integrity and functional accuracy. Without these opposing motor activities, we find that spindles are more fragile when mechanically challenged in metaphase, and highly twisted and error-prone in anaphase. More broadly, these findings suggest a design principle by which opposing active force generators make self-organizing cellular structures robust.

Results

Eg5 inhibition allows turbulent spindles to recover bipolarity and progress to anaphase

To generate human spindles lacking the opposing motor activities of NuMA/dynein and Eg5, we used an inducible CRISPR knockout (KO) approach [106] to delete either dynein heavy chain (DHC) or NuMA in RPE1 cells (Figures 2.7A-D). This results in chaotic, turbulent spindles that lose their long-range nematic order and constantly remodel, akin to active nematic materials in vitro [27, 107]. This phenotype differs from the barrel-shaped spindles resulting from RNAi depletion of DHC [97] and from multipolar spindles, both of which reach a steady-state shape. We induced Cas9 expression for 4 days to knock out DHC or NuMA, synchronized cells with the Cdk1 inhibitor RO-3306, and released cells into mitosis before live imaging labeled microtubules and chromosomes to ensure that turbulent spindles did not accumulate defects during an extended mitotic arrest (Figure 2.1B). As previously reported, spindles with DHC and NuMA deleted exhibited a very similar turbulent phenotype, consistent with NuMA and dynein's acting as a complex to cluster microtubule minus ends [27, 91]. After confirming knockout in each cell via spindle turbulence, we acutely inhibited Eg5 with S-trityl-L-cysteine (STLC), leading both DHC-KO and NuMA-KO spindles to recover into steady-state metaphase bipoles (Figures 2.1C-D; Figure 2.7E). Many doubly inhibited spindles exhibited local defects that dynamically arose and repaired (Figure 2.7F), but in contrast to expanded turbulent NuMA-KO spindles, global metaphase spindle shape and size was indistinguishable from controls (Figures 2.1E-H). The rescue and maintenance of bipolarity were highly reproducible and dependent on Eg5 inhibition (Figure 2.1I; Figure 2.7G).

A key advantage of this experimental system was that many (60.3%) of the bipolar NuMA-KO+STLC spindles progressed to anaphase within 90 min of STLC addition. The rest remained in metaphase after 90 min, with no detectable sister chromatid separation or spindle elongation. In contrast, few (3.3%) of the DHC-KO+STLC spindles entered anaphase (Figure 2.1J). Consistent with dynein's NuMA-independent roles at the kinetochore in attachment formation and silencing the spindle assembly checkpoint (SAC) [105, 108], bypassing the SAC using the MPS1 inhibitor reversine caused almost all NuMA- and DHC-KO+STLC cells to enter anaphase (Figure 2.1J). Due to these dynein-associated kinetochore defects, and their confounding effects in previous studies of DHC- and Eg5-doubly inhibited spindles [80], we used NuMA-KO cells for the remainder of our experiments to isolate dynein's minus end clustering role. This approach provided us a system for probing the contributions of opposing motors to spindle mechanics and function in both metaphase and anaphase, independently of spindle architecture.

Doubly inhibited spindles are sensitized to changes in microtubule organization, dynamics, and motor-based forces

We next asked what mechanisms allow turbulent spindles to establish bipolarity in the absence of NuMA/dynein and Eg5. We tested the contributions of additional candidate spindle factors, representing several functional classes, in the context of our live-imaged double inhibition experiment. Partially depleting the kinesin-12 KIF15 in doubly inhibited spindles led to an increase in monopolar spindle formation (46%; Figures 2.2A-B; Figure 2.8A), consistent with KIF15's known role in extensile stress generation [46, 80]. Similarly, depleting the microtubule crosslinker PRC1 or destabilizing microtubules with a low dose

(30 nM) of nocodazole increased the frequency of monopolar spindles (Figures 2.2A-B; Figure 2.8B). In all three conditions, spindles that did achieve bipolarity were shorter on average than controls (Figure 2.2C). Abrogating kinetochore-fiber (k-fiber) formation via Nuf2 depletion did not significantly impact the frequency of bipolarization in doubly inhibited spindles, but we observed a variety of defects including bent, over-bundled, and narrow spindles (Figures 2.2A-B; Figure 2.8C). None of these perturbations prevents bipolar spindle assembly in control cells [47, 48, 109, 110], yet these data suggest that KIF15, PRC1, and dynamic microtubules all generate extensile stresses that are necessary for bipolarity in the absence of Eg5.

Conversely, depleting the kinesin-14 HSET caused more spindles to remain turbulent (44%; Figures 2.2A-B; Figure 2.8A), indicating that it performs contractile minus end clustering redundantly with NuMA/dynein. F-actin was not required to focus minus ends during bipolarization, despite its importance in clustering supernumerary centrosomes [111]. Together, these triple inhibition experiments reveal that redundant motors and crosslinkers can generate bipolar spindles in the absence of NuMA and Eg5. However, these spindles are sensitized to changes in motor activity, microtubule organization and dynamics—biochemical fluctuations to which the wild-type spindle is robust.

Microtubule organization and dynamics are disrupted in doubly inhibited spindles

Given that NuMA- and Eg5-doubly inhibited spindles are less robust to perturbations in microtubule organization and dynamics, we tested the hypothesis that internal architecture is disrupted in doubly inhibited spindles. We examined microtubule

organization by quantifying the distribution of tubulin intensity along the spindle's pole-to-pole axis. As expected [112], control cells had strongest tubulin intensity near the two poles and lower intensity near the spindle equator. In contrast, tubulin intensity was more uniform in NuMA- and Eg5-doubly inhibited spindles (Figures 2.3A-B). This pattern was not due to a difference in chromosome alignment, as the intensity profile of the DNA stain Hoechst overlapped between the two conditions (Figure 2.3C). Thus, doubly inhibited spindles have altered microtubule organization, indicating that microtubule transport, nucleation, and/or length regulation in the spindle is disrupted without NuMA and Eg5.

Because both dynein and Eg5 are known to contribute to the continuous transport of non-kinetochore microtubules in the spindle [37], we next asked whether the altered spatial distribution of microtubules in doubly inhibited spindles was associated with perturbed microtubule dynamics. We expressed photoactivatable-GFP-tubulin in NuMA-KO cells, co-labeled spindles with SiR-tubulin, and photoactivated stripes near the metaphase plate (Figure 2.3D). Tracking photomark movements on individual k-fibers revealed that the poleward flux rate was halved in doubly inhibited spindles compared to controls ($0.9 \pm 0.5 \mu\text{m}/\text{min}$ compared to $1.8 \pm 0.6 \mu\text{m}/\text{min}$; Figure 2.3E). While outward sliding by Eg5 drives microtubule flux in *Xenopus laevis* extract spindles [52], k-fiber flux in mammalian spindles is thought to be largely powered by mechanisms other than Eg5 [53, 58, 113]. However, our findings indicate that NuMA and Eg5 are together key to microtubule flux in the human spindle. We conclude that redundant motors and crosslinkers can establish the spindle's global shape and size without the opposing stresses generated by NuMA/dynein and Eg5 (Figure 2.2), but they cannot recapitulate its locally specialized microtubule organization and dynamics.

Doubly inhibited spindles are structurally unstable in response to mechanical force

We next tested the hypothesis that opposing motors contribute to the spindle's ability to maintain its structure under force. Loss of opposing NuMA/dynein and Eg5 activities could give rise to mechanical defects through reduced microtubule organization and dynamics (Figure 2.3), or through changes to the spindle's material properties as a result of altered local force generation. To probe the mechanics of NuMA- and Eg5-doubly inhibited spindles, we reproducibly confined metaphase cells in PDMS devices [114], forcing them into a flattened 5 μm -high geometry (Figure 2.4A). Doubly inhibited spindles exhibited a different characteristic response to confinement than controls, both in their deformation over time and in their loss of structural integrity (Figure 2.4B). Although all spindles widened and lengthened during confinement, controls reached a new steady-state size after the first few minutes [64] while doubly inhibited spindles continued to expand, failing to reach a new steady-state size in our observation period. During initial expansion, spindles in both conditions widened similarly but doubly inhibited spindles lengthened more slowly, consistent with a role of NuMA/dynein in spindle elongation [115]. However, doubly inhibited spindles continued to grow in both dimensions throughout the perturbation, ultimately surpassing the new steady-state mean length and width of controls (Figures 2.4C-D). As another metric of spindle shape evolution, we calculated the 2-D correlation coefficient between binarized masks of the same spindle at multiple timepoint pairs. The shape correlation of doubly inhibited spindles was lower than that of controls at increasing lag times, and exponential fits revealed that shape correlation decayed to a lower minimum value for doubly inhibited spindles (Figure 2.4E). Thus,

under force, doubly inhibited spindles not only deform more but have a weaker “shape memory” than controls.

Strikingly, the impaired ability of doubly inhibited spindles to stabilize their shapes was associated with increased structural failure. By 20 minutes after confinement onset, k-fibers had detached from poles in 91% of doubly inhibited spindles, compared to 25% of controls (Figures 2.4B and 2.4F). Although control spindle poles can split during sustained confinement [116], failure in doubly inhibited spindles began sooner and occurred more frequently (Figure 2.4F). Dynein- and Eg5-doubly inhibited spindles, but not Eg5-inhibited spindles, also failed during confinement more often than controls (Figures 2.9A-C), indicating that the observed loss of mechanical integrity is due to a loss of opposing motor activity rather than due to Eg5 inhibition alone or any dynein-independent functions of NuMA. Moreover, the mode of failure qualitatively differed between doubly inhibited and control spindles: detached k-fibers in control spindles remained clustered into acentrosomal foci, but k-fibers in both NuMA- and DHC-KO doubly inhibited spindles splayed as individual bundles. Thus, while unperturbed doubly inhibited spindles maintain a similar geometry to controls (Figures 2.1F-H), their reduced structural integrity becomes evident upon mechanical challenge. Together, the larger deformation, lack of new steady-state establishment, and structural fragility of doubly inhibited spindles under force indicate that the opposing motor activities of NuMA/dynein and Eg5 are essential to the spindle’s mechanical robustness.

Spindles with reduced opposing motor activity exhibit twist and functional defects in anaphase

Given that NuMA/dynein and Eg5 are together required for the metaphase spindle's internal organization, dynamics (Figure 2.3) and mechanical robustness (Figure 2.4), we next sought to determine whether they are important to anaphase spindle structure and function. Our finding that NuMA-KO+STLC spindles efficiently undergo anaphase (Figure 2.1), in contrast to DHC-KO+STLC spindles, allowed us to address this question. In the first 3 minutes of anaphase doubly inhibited spindles elongated, and chromosomes segregated, at rates indistinguishable from controls (Figures 2.5A-C; Figures 2.10A-B). However, in doubly inhibited cells, spindle elongation and chromosome segregation continued at these rates for extended durations, causing spindle poles to often hit the cortex and chromosomes to segregate to greater distances (Figure 2.5C; Figures 2.10C-D). Although cortical NuMA/dynein complexes generate anaphase pulling forces in other systems [117, 118], and although Eg5 has been reported to contribute to outward sliding during human spindle elongation [119], our results indicate that NuMA- and Eg5-doubly inhibited spindles are not deficient in elongation but instead over-elongate in anaphase. Thus, either doubly inhibited spindles are subject to increased outward forces in anaphase, or they resist them less strongly.

Unexpectedly, we observed that in contrast with control spindles and Eg5-inhibited spindles, doubly inhibited spindles were highly twisted in anaphase. Interpolar microtubule bundles followed a left-handed helical path around the spindle (Figure 2.5D). While doubly inhibited spindles exhibited twist to a small degree at metaphase (Figures 2.11A-B), the phenotype was much more pronounced and consistently left-handed after

anaphase onset. To quantify this effect, we imaged z-stacks of anaphase spindles and tracked interpolar microtubule bundles in three-dimensional space. Viewing these trajectories along the pole-to-pole axis, interpolar bundles in doubly inhibited spindles had a helicity of -6.3 ± 3.4 °/ μm , a 17-fold increase over control bundles' helicity of -0.4 ± 2.0 °/ μm (mean \pm s.d.; Figures 2.5E-F; Figure 2.11C). Mean helicity was not correlated with anaphase spindle length ($r = -0.04$, Figure 2.11D), suggesting that spindle twist does not markedly increase or decrease as anaphase progresses. Together, these findings reveal an unexpected role for the opposing motor activities of NuMA/dynein and Eg5: although not required for linear force balance in the pole-to-pole axis (Figure 2.1F), they are required for rotational force balance in the anaphase spindle.

Finally, we asked whether chromosome segregation fidelity was preserved in doubly inhibited spindles. The incidence of chromosome segregation errors—defined here as lagging chromosomes or chromosome bridges—was significantly higher in NuMA-KO+STLC spindles than in controls (45.7% vs 7.1%; Figures 2.5G-H). Thus, while NuMA and Eg5 are not required for efficient spindle elongation, they are instead required at anaphase for the spindle's straight long-range architecture and for accurate chromosome segregation.

Discussion

The conserved presence of opposing extensile and contractile force-generators, despite their expendability for bipolar spindle formation, presents a long-standing paradox in spindle assembly. Our use of direct mechanical perturbations, as well as our approach of deleting NuMA to preserve dynein's functions at the kinetochore, reveal key roles of this opposing motor activity. Although NuMA- and Eg5-doubly inhibited spindles appear strikingly similar to controls, they are mechanically fragile at metaphase as well as dramatically twisted and error-prone at anaphase, defects that we propose stem from their altered dynamics, organization, and material properties (Figure 2.6). While partially redundant motors can establish spindle shape and support anaphase progression, the opposing activities of NuMA/dynein and Eg5 are required to build a spindle that can maintain its structure and accurate function despite internal and external pushes, pulls, and torques.

We show that mechanistically, the bipolarization of turbulent spindles after Eg5 inhibition requires the motors KIF15 and HSET, crosslinking by PRC1, and dynamic microtubules (Figure 2.2). KIF15 is known to compensate for the loss of Eg5 in forming and maintaining bipolar spindles, generating extensile stress through a mechanism distinct from that of Eg5 [46-48, 80]. Although HSET has a mild loss-of-function phenotype in human cells [36], it forms microtubule asters in vitro [35, 120] and clusters centrosomes in cancer cells [111], and our data suggests that it has a minus end clustering role that is unmasked in the absence of NuMA/dynein. Interestingly, fission yeast lacking all mitotic motors can form bipolar spindles that require the PRC1 homolog Ase1 and microtubule polymerization [102]. That we observe similar requirements in the absence of NuMA and

Eg5 may reflect a conserved pathway for spindle assembly, based on microtubule bundling and polymerization, that complements the spindle's motor-driven microtubule sorting and that becomes essential when motor activity is reduced.

NuMA and Eg5 are together essential to establishing the spindle's locally specialized microtubule organization and dynamics (Figure 2.3), roles that may explain the spindle's sensitivity to further molecular perturbations in their absence. The spindle's microtubule organization is established by spatially non-uniform distributions of microtubule nucleation and transport, and inhibition of Eg5 and NuMA/dynein could affect both activities. Eg5 and dynein are required to transport the nucleation factor TPX2 polewards in the mammalian spindle [121], and in their absence, microtubule nucleation may be shifted towards chromosomes. Eg5 and dynein both transport non-centrosomal microtubules towards poles [37, 103], polarity-sorting them and incorporating them into the spindle. Thus, in the absence of NuMA/dynein and Eg5, we propose that the spindle's tubulin intensity distribution is homogenized due to both deregulated microtubule nucleation and transport towards poles. K-fiber flux in the human spindle is thought to arise from imperfect coupling of k-fibers to these non-kinetochore microtubules [56, 113], a model that would explain why we observe reduced k-fiber flux in doubly inhibited spindles.

We find that spindles are more mechanically fragile without opposing NuMA/dynein and Eg5 activity (Figure 2.4). This could stem from lower microtubule enrichment at poles (Figure 2.3B) [67], a less dynamic spindle (Figure 2.3E), reduced passive crosslinking, or decreased active stresses throughout the spindle. All of these are ways in which reduced opposing motor activity could impair the spindle's ability to distribute and dissipate force,

and thereby change the magnitude and timescale of the spindle's deformation under force. Motors broadly regulate the material properties of microtubule networks, such as their elasticity and viscosity [66, 69]. Looking forward, combining the experimental system used here with approaches such as microneedle manipulation [66, 67, 122, 123] will enable us to understand how opposing motors quantitatively tune the spindle's emergent mechanical properties.

Our anaphase observations indicate that spindles have structural as well as functional defects without NuMA and Eg5. The efficient elongation of doubly inhibited spindles supports a model where Eg5-independent sliding within the spindle can generate the bulk of the force required for chromosome segregation [9, 119, 124]. However, in contrast to controls, doubly inhibited anaphase spindles exhibit strong left-handed twist, suggesting that they have an imbalance in torques. Multiple mitotic motors have an intrinsic chirality to their stepping motion in vitro [72, 77, 125, 126], which can twist microtubules around each other [76]. At the cellular scale, left-handed helicity of a smaller magnitude (approximately $-2^\circ/\mu\text{m}$) exists in metaphase and anaphase human spindles, but this twist is reduced by Eg5 inhibition [71, 127]. Thus, as Eg5 is inhibited in the anaphase spindles probed here, a different mechanism must produce the left-handed torque. One possibility is that spindles lacking NuMA/dynein and Eg5 activity are twisted due to abnormally high torques generated by the motors that compensate for their absence. However, because doubly inhibited spindles are more mechanically deformable (Figure 2.4) and because they over-elongate in anaphase (Figure 2.5B), we favor a model in which they are instead more torsionally compliant. Regardless of its molecular origin, the appearance of twist upon inhibition of NuMA and Eg5 raises the question of how the

cell builds a micron-scale, near-achiral spindle from nanometer-scale chiral events. This requires a balancing of three-dimensional rotational forces over large length scales, through mechanisms that remain poorly understood. The doubly inhibited spindles we generate here may provide a system to uncover these mechanisms, and to address the functional impact of twist in the anaphase spindle.

Doubly inhibited spindles exhibit a 6-fold increase in chromosome segregation errors. Decreased flux has been linked to attachment errors and lagging chromosomes in anaphase, through a mechanism that remains incompletely understood [56, 58]; this phenomenon could be at play in doubly inhibited spindles, given their drastically reduced flux. Alternatively, lagging chromosomes could arise due to the assembly pathway of doubly inhibited spindles in our assay. Since the NuMA- or DHC-KO spindles begin as turbulent networks before Eg5 inhibition, the minus end clustering process could lead to an elevated rate of merotelic attachment formation, similar to the attachment errors that arise during the clustering of supernumerary centrosomes [39]. In addition to either or both of these mechanisms, anaphase twist in doubly inhibited spindles could contribute to segregation errors. For example, segregating chromosomes might follow more complex, entangled trajectories, or the elongating spindle could generate an increased non-productive force component that diminishes the spindle's ability to resolve merotelic attachments.

Overall, our findings indicate that the opposing activities of NuMA/dynein and Eg5 are critical for the spindle's mechanical and functional robustness, allowing the spindle to withstand force and accurately segregate chromosomes despite its dynamic molecular parts. An energy-accuracy tradeoff has been demonstrated experimentally and

theoretically in biochemical networks: for instance, repeated energy-consuming cycles of kinase and phosphatase activity synchronize cell cycle timing in zebrafish embryos [128], and phase coherence scales with energy dissipation in a variety of biochemical oscillators [129]. We propose that opposing spindle motors provide a mechanical analog, where the spindle's structural integrity and functional accuracy incur an energetic cost beyond that required to establish spindle structure. Opposing active force generators may constitute a physical design principle that underlies robustness in other dynamic, self-organizing cellular structures, such as cell-cell junctions.

Limitations of the study

NuMA/dynein and Eg5 actively transport microtubules to generate contractile and extensile stresses in the spindle, but also contribute to passive crosslinking by virtue of interacting with microtubule pairs. Eliminating this motor-mediated crosslinking, in addition to reducing opposing active stresses, could play a role in the defects we observe in doubly inhibited spindles. However, we find that STLC treatment alone increases mechanical robustness (Figure 2.9) and does not change anaphase twist (Figure 2.11C) compared to control spindles, rather than producing phenotypes intermediate between controls and doubly inhibited spindles. NuMA has also been proposed to have a dynein-independent passive crosslinking role [130]. While further work is required to define NuMA's contributions to passive and dynein-dependent crosslinking, we observe similar responses to confinement in doubly inhibited spindles generated via knockout of NuMA or dynein heavy chain (Figure 2.4F; Figures 2.9B-C). Thus, reduced crosslinking

mediated by Eg5 or NuMA alone does not appear to play a substantial role in the mechanical fragility or anaphase twist we report in doubly inhibited spindles.

Figures and figure legends

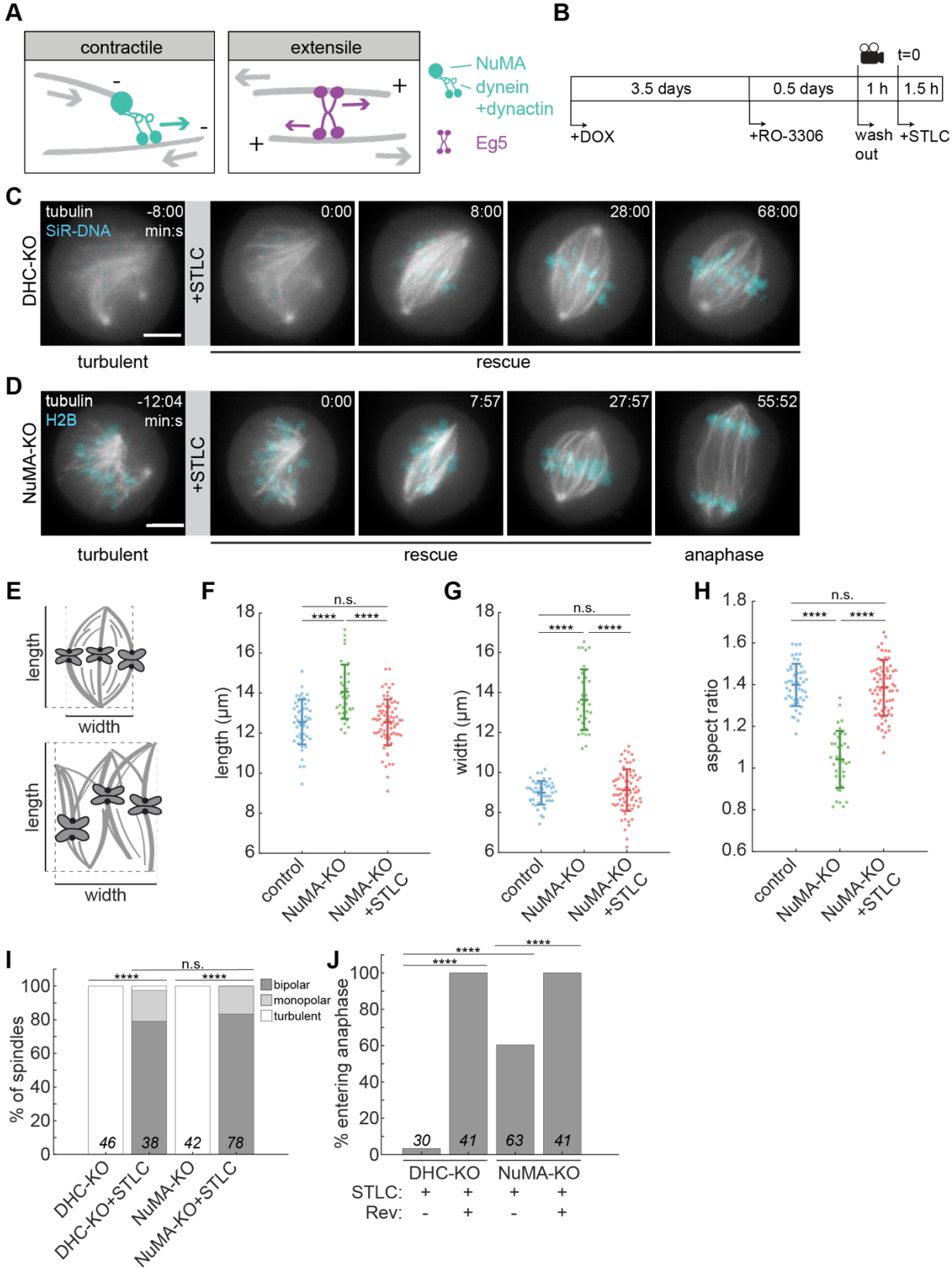


Figure 2.1. Eg5 inhibition allows turbulent spindles to recover bipolarity and progress to anaphase.

A) Schematic illustrations of contractile microtubule (gray filament) minus end clustering by dynein, dynactin, and NuMA (left, green), and extensile sliding of antiparallel microtubules by Eg5 (right, purple) in the human spindle. Dynein/dynactin, targeted to minus end cargoes by NuMA, walks towards microtubule minus ends (denoted by “-“). Eg5 walks towards microtubule plus ends (denoted by “+”). Direction of motor stepping is indicated by green and purple arrows, and contractile and extensile stresses are indicated by gray arrows.

B) Schematic diagram of opposing motor (NuMA/dynein and Eg5) inhibition experiment in human spindles. Cas9 expression was induced by doxycycline addition (+DOX) for 4 days to knock out dynein heavy chain or NuMA. Cells were synchronized in G2 (with Cdk1 inhibitor RO-3306) for 0.5 days before imaging, released into mitosis, and Eg5 was acutely inhibited during imaging with 5 μ M STLC. See also Figure 2.7.

C) Representative timelapse confocal images of an RPE1 DHC-KO cell stably expressing GFP-tubulin (gray, maximum intensity projection of 5 planes) with SiR-DNA labeling chromosomes (cyan, single plane), starting as a turbulent spindle. After 5 μ M STLC addition to inhibit Eg5 (time 0:00), the turbulent spindle recovers bipolarity, but does not progress to anaphase. Scale bar = 5 μ m.

D) Representative timelapse confocal images of an RPE1 NuMA-KO cell stably expressing GFP-tubulin (gray, maximum intensity projection of 5 planes) and mCherry-H2B (cyan, single plane), starting as a turbulent spindle. After 5 μ M STLC addition to inhibit Eg5 (time 0:00), the turbulent spindle recovers bipolarity and progresses to anaphase. Scale bar = 5 μ m.

E) Schematic illustrations of spindle length and width measurements.

F-H) Length (F), width (G), and aspect ratio (length/width; (H)) of control (-DOX), turbulent NuMA-KO, and bipolar NuMA-KO+STLC spindles. Spindle dimensions were measured after establishment of bipolarity (control, NuMA-KO+STLC) or 45 min after the start of imaging (NuMA-KO). Data in (F)-(H) include the same 49 (control), 36 (NuMA-KO), and 75 (NuMA-KO+STLC) spindles pooled from ≥ 3 independent experiments. ****, $p < 0.00005$; n.s. = not significant, two-sample t-test. Error bars represent mean \pm s.d.

I) Outcomes 90 min post-STLC addition to NuMA- and DHC-KO turbulent spindles. Without STLC addition, DHC-KO and NuMA-KO spindles remain turbulent. After STLC addition, most spindles establish bipolarity.

J) Percentage of bipolar spindles entering anaphase within 90 min of STLC addition, with and without 500 nM of the MPS1 inhibitor reversine to bypass the SAC. DHC-KO+STLC cells enter anaphase after reversine addition, consistent with DHC-KO+STLC cells experiencing a SAC-dependent metaphase arrest. For (I)-(J), number of spindles is indicated on each bar; cells pooled from ≥ 3 independent experiments. ****, $p < 0.00005$, n.s. = not significant, Fisher’s exact test.

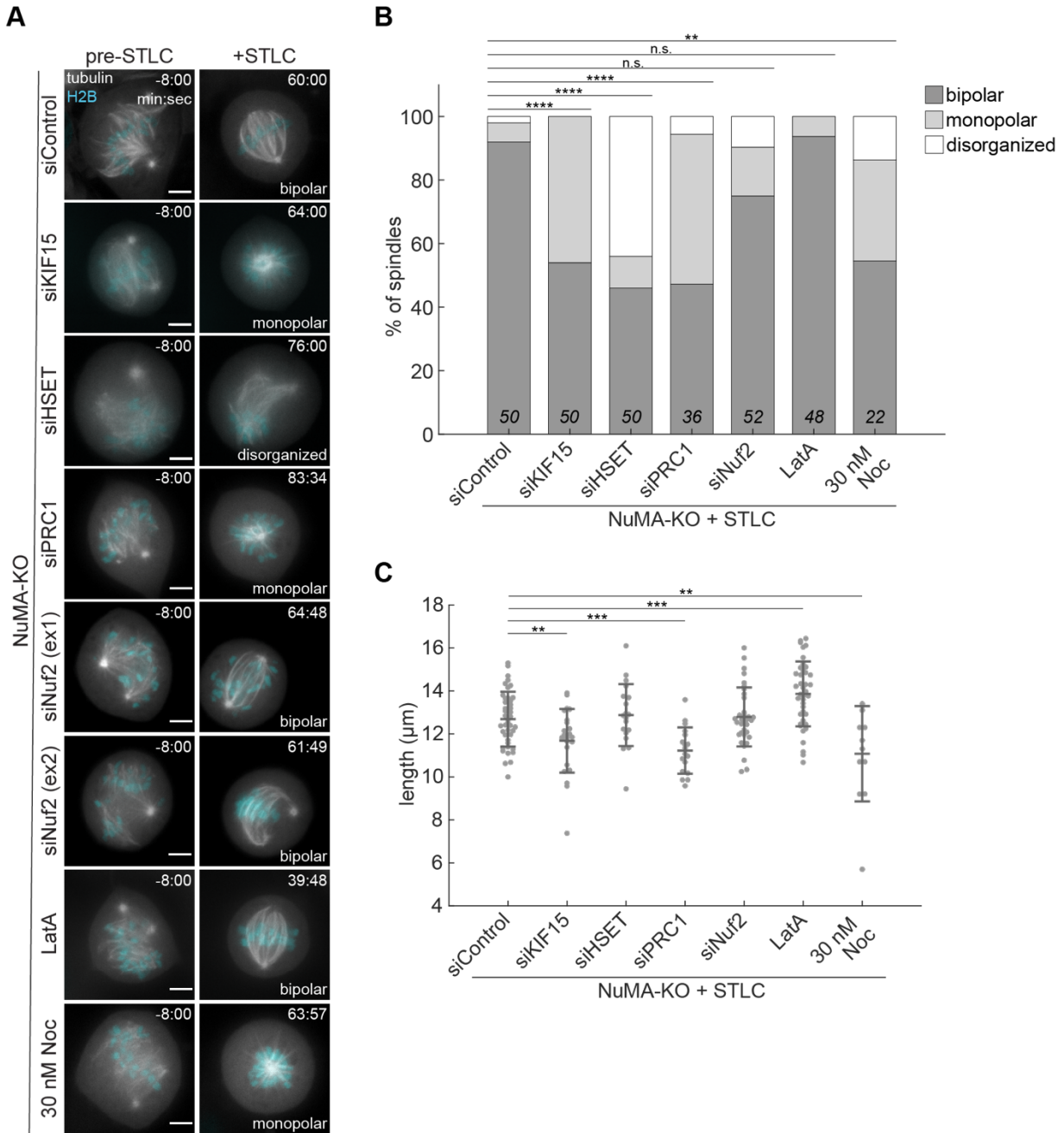


Figure 2.2. Doubly inhibited spindles are sensitized to changes in microtubule organization, dynamics, and motor-based forces.

A) Representative timelapse confocal images of RPE1 NuMA-KO cells, stably expressing GFP-tubulin (gray, maximum intensity projection of 5 planes) and mCherry-H2B (cyan, single plane), and transfected with the indicated siRNA or treated with the indicated drug. 5 μ M STLC was added at time 0:00 in each case, and 500 nM LatA and 30 nM nocodazole were added at time 0:00 where indicated. Scale bars = 5 μ m. See also Figure 2.8.

B) Spindle outcomes in NuMA-KO cells 90 min after STLC addition, with luciferase (Control), KIF15, HSET, PRC1, or Nuf2 knockdown, 500 nM latrunculin A to disrupt actin,

or 30 nM nocodazole to destabilize microtubules. Depletion of KIF15 or PRC1 and microtubule destabilization using low-dose nocodazole result in more monopolar spindles, while depletion of HSET causes more spindles to remain disorganized. Number of spindles is indicated on each bar; cells pooled from ≥ 3 independent experiments. ****, $p < 0.00005$; **, $p < 0.005$; n.s., not significant, Fisher's exact test.

C) Length of NuMA-KO + STLC spindles, transfected with the indicated siRNA or treated with the indicated drug, after the establishment of bipolarity. Data include the same spindles as (B), restricted to those scored as bipolar. Doubly inhibited bipoles are shorter on average after KIF15 or PRC1 depletion or treatment with low-dose nocodazole, and are longer on average after disruption of F-actin with latrunculin A. ***, $p < 0.0005$; **, $p < 0.005$, two-sample t-test. Error bars represent mean \pm s.d.

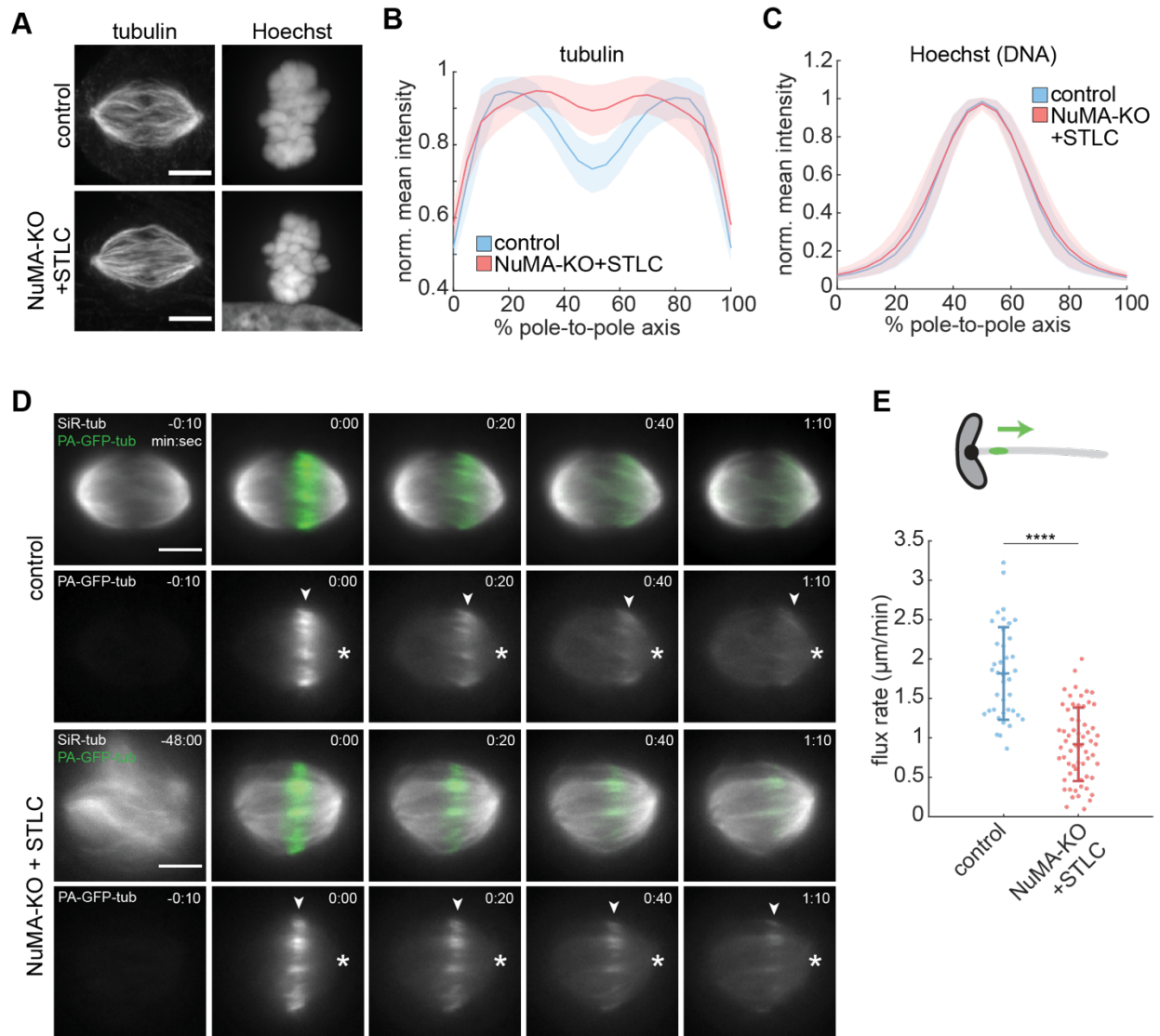


Figure 2.3. Microtubule organization and dynamics are disrupted in doubly inhibited spindles.

A) Representative immunofluorescence images (maximum intensity projections) of control and NuMA-KO+STLC RPE1 cells, stained for tubulin (left) and with Hoechst (right). Scale bar = 5 μm .

B-C) Distributions of mean tubulin (B) and Hoechst (C) intensity at each point along the spindle's pole-to-pole axis, quantified from sum intensity projections of immunofluorescence images and normalized to the maximum value in each spindle (see Methods). Doubly inhibited spindles have defects in microtubule organization. (B) and (C) include the same 335 control and 336 NuMA-KO+STLC cells pooled from 8 independent experiments. Plots represent mean \pm s.d.

D) Representative timelapse widefield images of RPE1 control and NuMA-KO+STLC cells stably expressing photoactivatable (PA)-GFP-tubulin (green), co-labeled with 100 nM SiR-tubulin (gray) and photomarked near the spindle equator ($t = 0:00$). The PA-GFP-

tubulin channel alone is shown below the merged images. Arrowheads track the photomark position, and asterisks mark the spindle pole. Scale bars = 5 μ m.

E) Poleward flux rates in control and NuMA-KO+STLC cells, showing reduced microtubule transport in doubly inhibited spindles. Each dot represents an individual k-fiber. $n = 39$ k-fibers pooled from 14 cells in 1 experiment (control), $n = 61$ k-fibers pooled from 25 cells in 5 independent experiments (NuMA-KO+STLC). ****, $p < 0.00005$, two-sample t-test. Error bars represent mean \pm s.d.

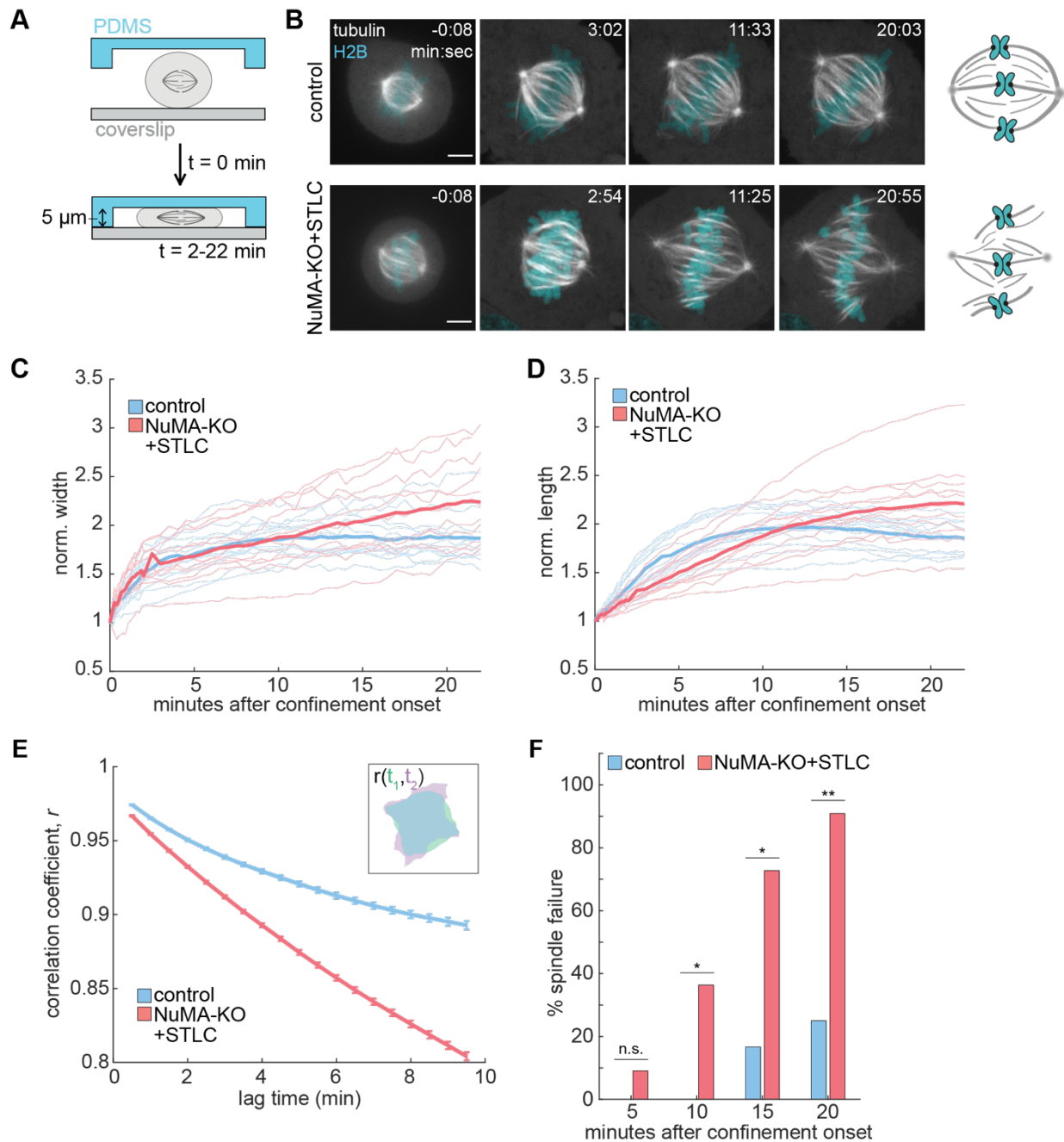


Figure 2.4. Doubly inhibited spindles are structurally unstable in response to mechanical force.

A) Schematic illustration of cell confinement experiment to probe spindle mechanical robustness. Confinement to 5 μm was applied over a period of 2 min, and the confined geometry was sustained for an additional 20 min.

B) Timelapse confocal images of control and NuMA-KO+STLC RPE1 cells stably expressing GFP-tubulin (gray) and H2B (cyan) during confinement (begins at $t = 0:00$).

K-fibers detach from poles in the doubly inhibited spindle, while the control spindle remains intact, as cartooned (right). Scale bars = 5 μ m.

C-D) Spindle width (C) and length (D) during confinement of control and NuMA-KO+STLC RPE1 cells, normalized to the initial length and width of each spindle. Mean values shown in bold lines. $n = 12$ control and 11 NuMA-KO+STLC cells, pooled from 5 and 4 independent experiments, respectively.

E) Mean \pm s.e.m. of spindle shape correlation coefficient between all pairs of two binary, segmented frames (green t_1 , purple t_2 in inset), as a function of the time elapsed between the two frames (t_2-t_1). Shape correlation was fit to the exponential function $r = a * e^{(-\frac{1}{\tau}) * lag\ time} + b$, where $b = 0.87$ for controls and $b = 0.58$ for NuMA-KO+STLC. Analysis includes the same cells as (C-D).

F) Percentage of spindles that structurally fail under confinement, defined qualitatively as a loss of continuity between k-fibers and poles. Doubly inhibited spindles begin to fail earlier, and fail more frequently, than controls. *, $p < 0.05$; **, $p < 0.005$; n.s., not significant; Fisher's exact test. Analysis includes the same cells as (C-E). See also Figure 2.9.

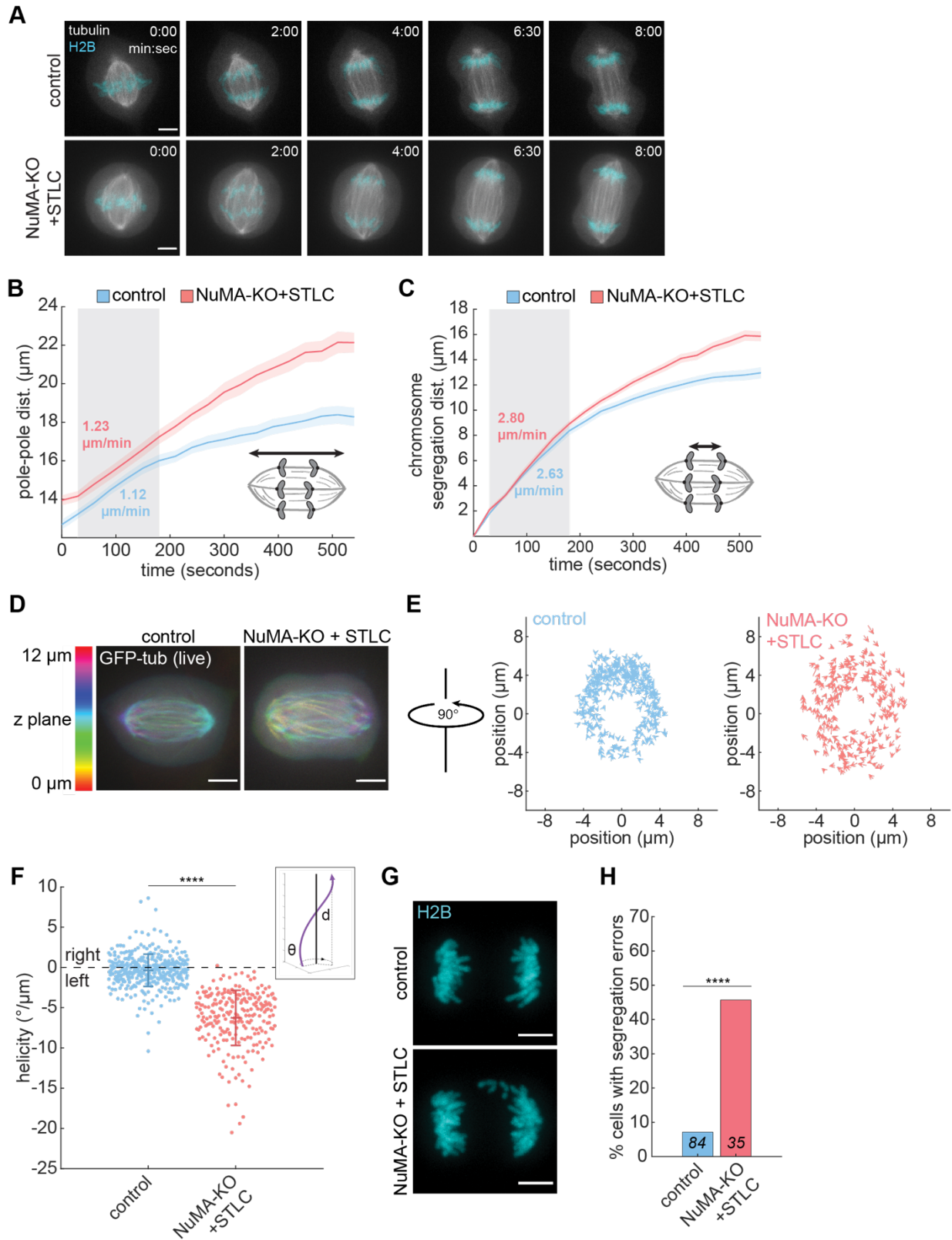


Figure 2.5. Spindles with reduced opposing motor activity exhibit twist and functional defects in anaphase.

A) Representative timelapse confocal images of control and NuMA-KO+STLC RPE1 cells, stably expressing GFP-tubulin (gray) and H2B (cyan), during anaphase (begins at $t = 0:00$). Images represent a single z-plane. Scale bars = 5 μm .

B) Spindle pole-to-pole distance during anaphase (aligned to anaphase onset at $t = 0$). Spindles initially elongate at indistinguishable rates (mean rates calculated over gray boxed area), but ultimately elongate more in doubly inhibited spindles. Lines and shaded regions indicate mean \pm s.e.m. of 20 cells (control) or 18 cells (NuMA-KO+STLC) pooled from 4 independent days. See also Figure 2.10.

C) Distance between the two segregating chromosome masses in anaphase (anaphase onset at $t = 0$), same cells as (B). Chromosomes initially segregate at indistinguishable rates (mean rates calculated over gray boxed area), but segregate a greater total distance in doubly inhibited spindles. Lines and shaded regions indicate mean \pm s.e.m. See also Figure 2.10.

D) Representative confocal images of GFP-tubulin-labeled control (left) and NuMA-KO+STLC (right) RPE1 anaphase cells, showing a single timepoint from live imaging. Spindles are colored by z-plane. Scale bars = 5 μm .

E) Spindle pole end-on views (90° rotation compared to view in (D)) of tracked interpolar microtubule bundles in control and NuMA-KO+STLC anaphase spindles. Arrow vectors represent the displacement of each bundle per μm traversed along the pole-to-pole axis, moving towards the viewer. $n = 370$ bundles, pooled from 40 cells in 5 independent experiments (control) and $n = 238$ bundles, pooled from 26 cells in 5 independent experiments (NuMA-KO+STLC).

F) Helicity of individual interpolar microtubule bundles, measured in degrees rotated (θ) around the pole-to-pole axis per μm traversed (d) along the pole-to-pole axis for each bundle. Schematic illustration of the helicity measurement shown in inset. Plot includes the same bundles tracked in (E). ****, $p < 0.00005$, two-sample t-test. Error bars represent mean \pm s.d. See also Figure 2.11.

G) Representative confocal images of control and NuMA-KO+STLC RPE1 anaphase cells stably expressing GFP-tubulin (not shown) and mCherry-H2B (cyan, maximum intensity projections, single frame from live imaging), showing lagging chromosomes in the NuMA-KO+STLC cell. Scale bars = 5 μm .

H) Percentage of anaphase cells with lagging chromosomes or chromosome bridges, showing increased segregation defects in NuMA-KO+STLC cells. $n = 84$ control cells pooled from 6 independent experiments; $n = 35$ NuMA-KO+STLC cells pooled from 5 independent experiments. ****, $p < 0.00005$, Fisher's exact test.

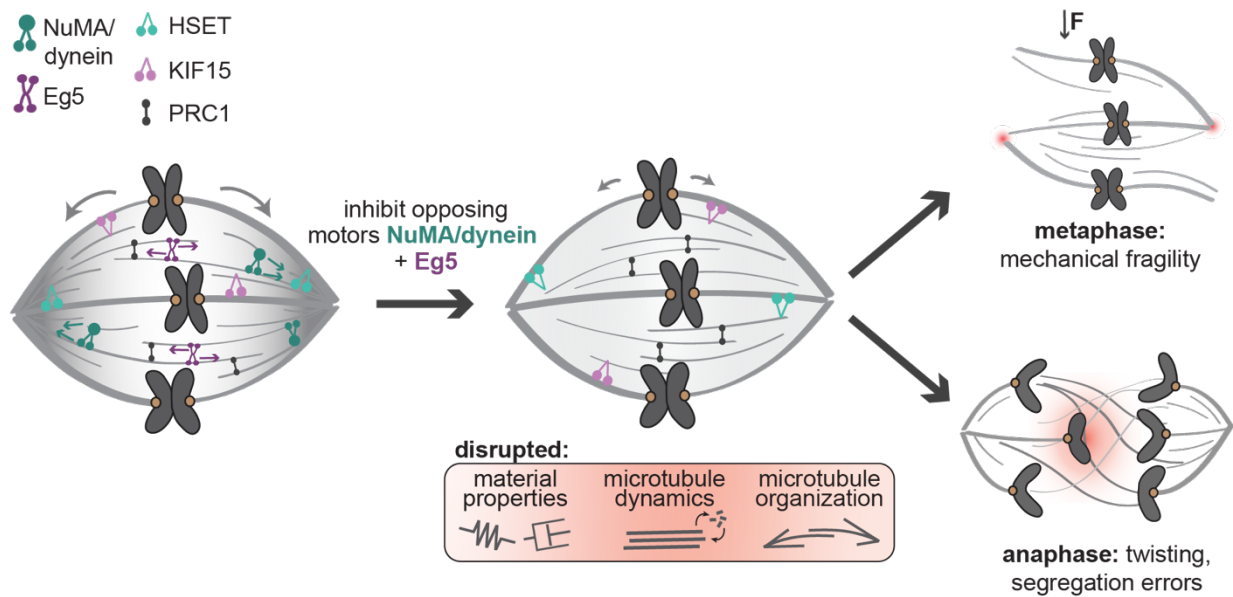


Figure 2.6. Model for opposing active stresses providing mechanical and functional robustness to the human spindle.

The spindle has opposing contractile and extensile stresses generated by NuMA/dynein (dark green) and Eg5 (dark purple), respectively. Without these opposing active stresses (center), the human spindle retains its steady-state shape and size, due in part to the activities of the motors HSET (light green) and KIF15 (light purple) and the crosslinker PRC1 (black). However, these doubly inhibited spindles have reduced internal organization (gray gradient) and dynamics (gray arrows). These spindles are more structurally fragile when subjected to force at metaphase (top right), become highly twisted at anaphase, and exhibit chromosome segregation errors (lower right). We propose that opposing active stresses give rise to mechanical and functional robustness by increasing the spindle's microtubule organization and dynamics, and by tuning its material properties (springs, elasticity; dashpots, viscosity) to limit the magnitude and timescale of allowed deformations. Together, this work suggests a design principle whereby opposing active force generators promote mechanical and functional robustness of cellular machines.

Supplemental figures and figure legends

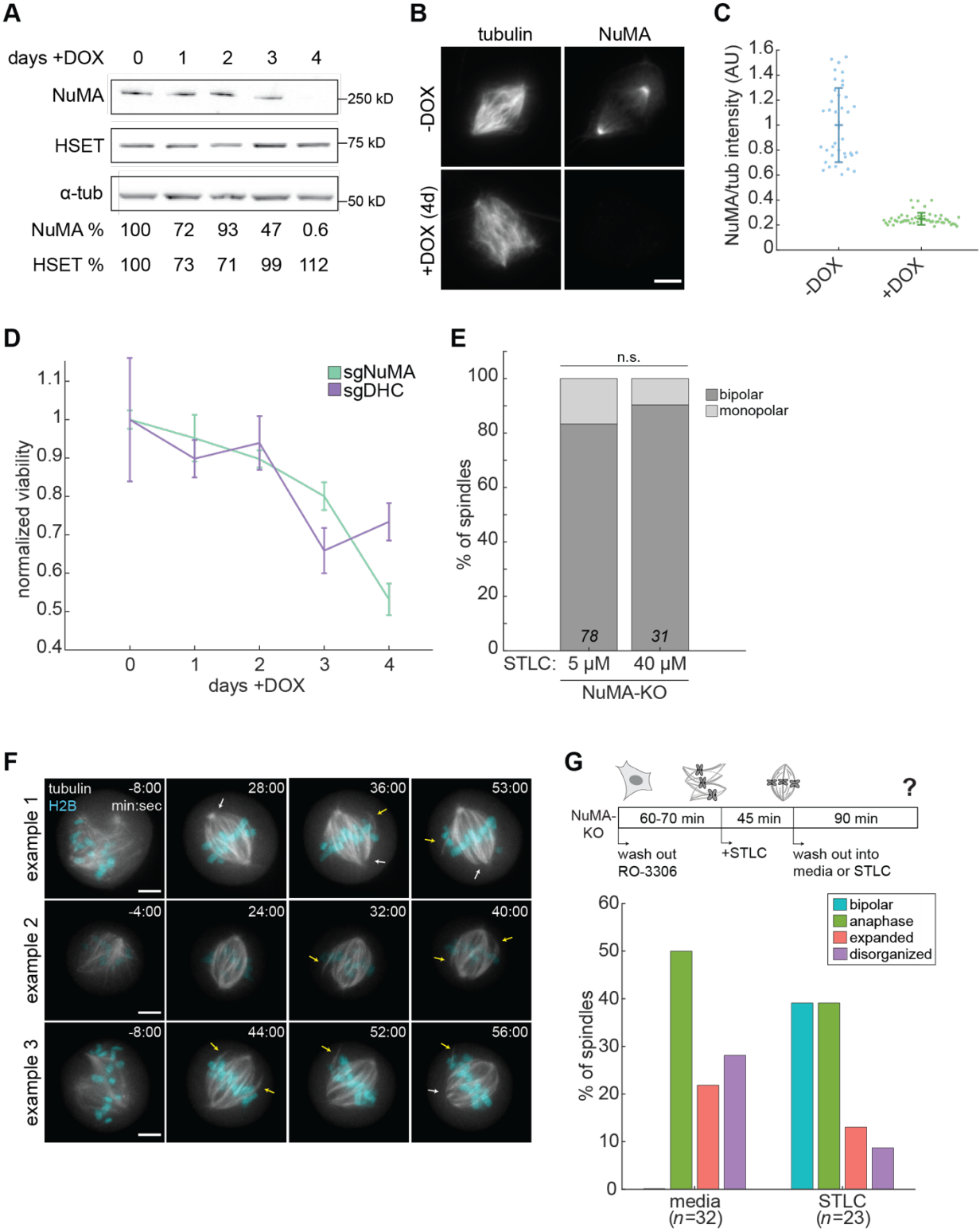


Figure 2.7. Additional analysis of NuMA- and Eg5-doubly inhibited spindles, related to Figure 2.1.

A) Western blot of NuMA and HSET levels in RPE1 cells after DOX-induced Cas9 expression for the indicated number of days. Although NuMA and HSET both perform microtubule minus end clustering in the spindle, HSET is not upregulated during NuMA knockout. Tubulin is shown as a loading control, and quantifications are normalized to the tubulin level in each lane.

B) Representative immunofluorescence images (sum projections) of inducible NuMA-KO RPE1 cells with or without DOX induction of Cas9 for 4 days. Cells are stained for tubulin (left) and NuMA (right). Scale bar = 5 μ m.

C) Quantification of NuMA intensity in immunofluorescence images (sum projections), normalized to tubulin intensity. Control (-DOX) metaphase cells were compared to NuMA-KO (+DOX) cells with turbulent spindles. $n = 39$ cells (-DOX) and 53 cells (+DOX) from one experiment. Error bars represent mean \pm s.d.

D) Cell viability after DOX-induced Cas9 expression for the indicated number of days, in the RPE1 NuMA-KO (green) and DHC-KO (purple) cell lines. The 4-day DOX treatment used throughout this study was chosen to optimize for full protein depletion while retaining adequate cell viability. Viability was measured using the CellTiter-Glo assay. Error bars represent mean \pm s.d.

E) Spindle outcomes in NuMA-KO cells, 90 minutes after addition of 5 or 40 μ M STLC. Number of spindles indicated on each bar, pooled from ≥ 3 independent experiments. n.s., not significant, Fisher's exact test.

F) Timelapse confocal images of RPE1 NuMA-KO+STLC cells, stably expressing GFP-tubulin (gray) and mCherry-H2B (cyan). Spindles recover bipolarity after 5 μ M STLC addition at time 0:00. White arrows indicate pole unfocusing, and yellow arrows indicate k-fibers that dynamically splay and reincorporate into the bipolar spindle. The tubulin channel shows maximum intensity projections of 5 planes spaced 0.5 μ m apart, while the H2B channel shows single z-planes. Scale bars = 5 μ m.

G) STLC washout experiment. NuMA-KO cells were synchronized overnight with RO-3306, released into mitosis to form turbulent spindles, and treated with 5 μ M STLC. After spindles established bipolarity, cells were washed 4 times at $t = 45$ min into plain media or media containing 5 μ M STLC, and spindle outcomes were scored 90 min later. In both conditions, many spindles progressed to anaphase within 90 min; the remainder became expanded or re-established turbulence in the absence of STLC (media) or mostly maintained their bipolar structures (STLC). Thus, continued inhibition of Eg5 is required for long-term maintenance of bipolarity. $n = 32$ spindles (media) and 23 spindles (STLC) pooled from 3 independent experiments.

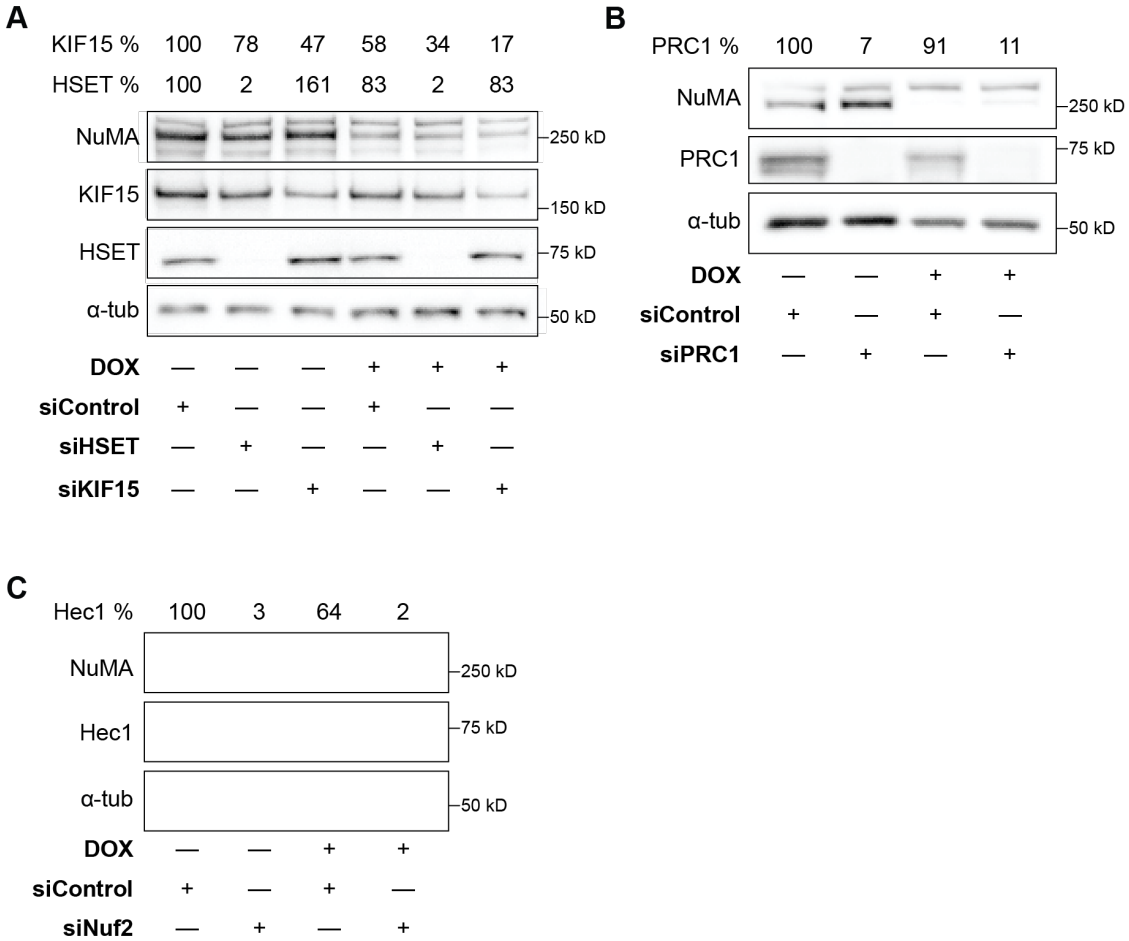


Figure 2.8. Validation of RNAi depletions, related to Figure 2.2.

A) Western blot of NuMA, KIF15, and HSET levels in RPE1 cells with or without DOX induction of Cas9 for 4 days, and transfected with siRNA targeting luciferase (Control) or HSET for 48 hours, or siRNA targeting KIF15 for 24 hours. Tubulin is shown as a loading control, and quantifications are normalized to the tubulin level in each lane. While NuMA-KO efficiency at the population level varied between experiments, NuMA-KO was verified in each individual cell, for all experiments, based on NuMA immunofluorescence or live imaging of the turbulent phenotype prior to STLC addition.

B) Western blot of NuMA and PRC1 levels in RPE1 cells with or without DOX induction of Cas9 for 4 days, and transfected with siRNA targeting luciferase (Control) or PRC1 for 24 hours. Tubulin is shown as a loading control, and quantifications are normalized to the tubulin level in each lane.

C) Western blot of NuMA and Hec1 levels in RPE1 cells with or without DOX induction of Cas9 for 4 days, and transfected with siRNA targeting luciferase (Control) or Nuf2 for 48 hours. RNAi targeting Nuf2 or Hec1 has been shown to result in the depletion of both proteins [131]. Tubulin is shown as a loading control, and quantifications are normalized to the tubulin level in each lane.

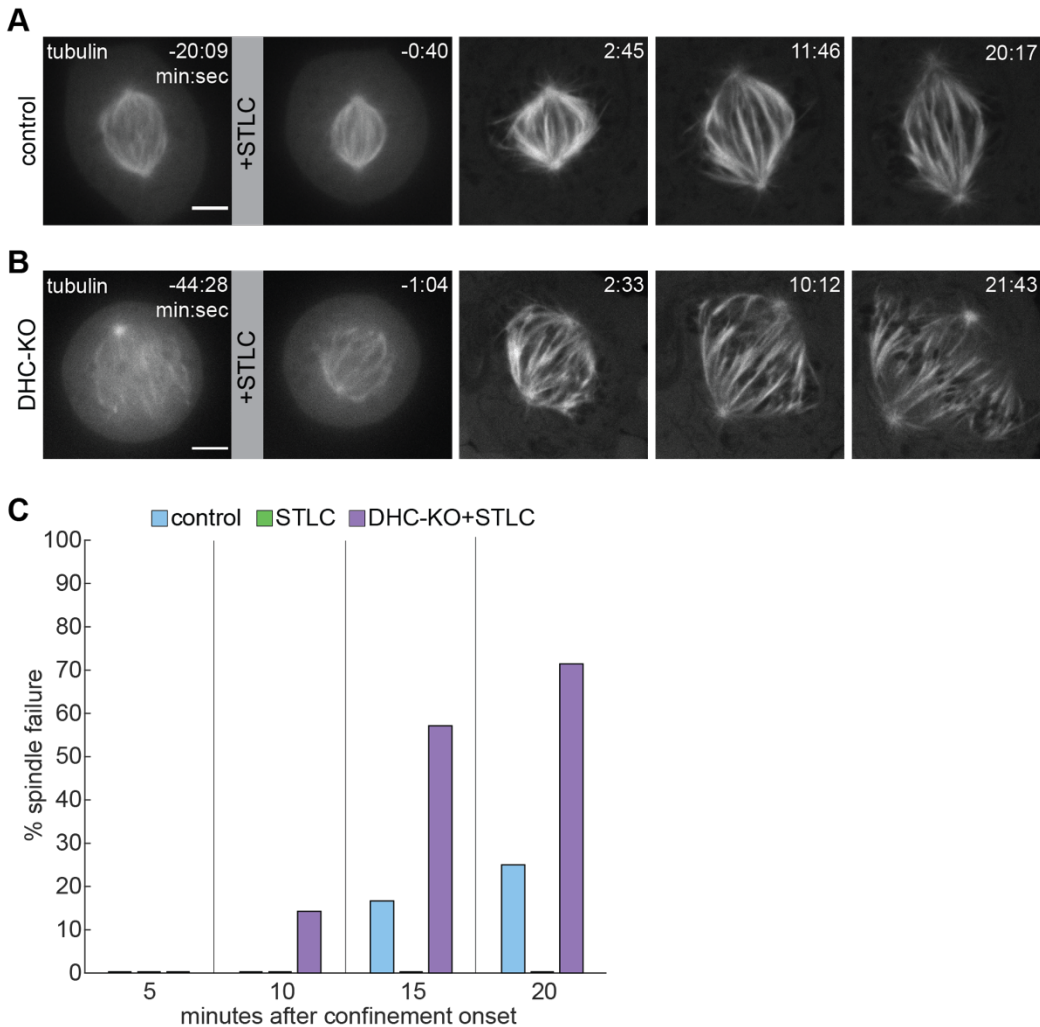


Figure 2.9. Dynein- and Eg5-doubly inhibited spindles, but not Eg5-inhibited spindles, are mechanically fragile, related to Figure 2.4.

A) Timelapse confocal images of a control RPE1 cell stably expressing GFP-tubulin (gray), treated with 5 μ M STLC during metaphase at t = -19:00 and confined beginning at t = 0:00. The spindle shrinks after Eg5 inhibition and then expands during confinement, but remains structurally intact. Cells that had not collapsed into monopoles by 15 min post-STLC addition were chosen to follow during confinement. Scale bar = 5 μ m.

B) Timelapse confocal images of a DHC-KO RPE1 cell stably expressing GFP-tubulin (gray), treated with 5 μ M STLC at t = -39:00 and confined beginning at t = 0:00. The spindle re-establishes bipolarity after Eg5 inhibition and then expands during confinement, and structurally fails as k-fibers detach from spindle poles. Scale bar = 5 μ m.

C) Percentage of spindles that structurally fail under confinement, defined qualitatively as a loss of continuity between k-fibers and poles. Similarly to NuMA-KO + STLC spindles, DHC-KO + STLC doubly inhibited spindles (purple) structurally fail earlier and more frequently than control spindles (blue). Spindles with only Eg5 inhibited (STLC; green) were never observed to fail. n = 12 control (same spindles as shown in Figure 2.4), 9 STLC, and 7 DHC-KO + STLC spindles pooled from ≥ 3 independent experiments.

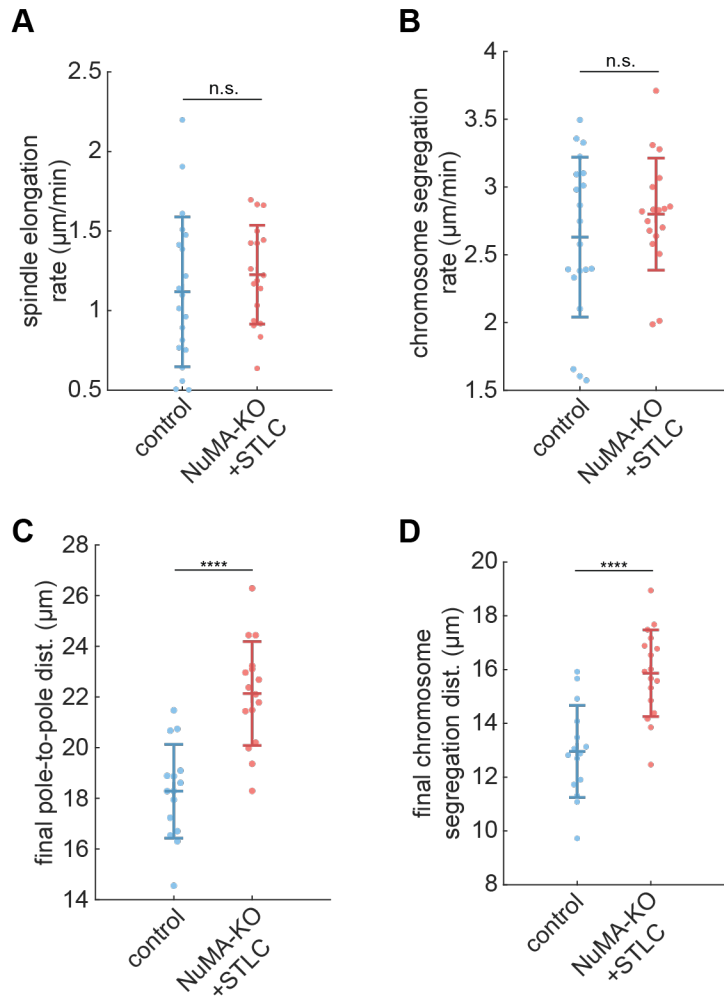


Figure 2.10. Comparison of anaphase movements in control and doubly inhibited spindles, related to Figure 2.5.

A) Average spindle elongation rate (change in pole-to-pole distance per min) in the period from 30-180 s after anaphase onset, corresponding to the gray shaded box in Figure 2.5B, in control and NuMA-KO+STLC RPE1 cells.

B) Average chromosome segregation rate (change in distance between chromosome masses per min) in the period from 30-180 s after anaphase onset, corresponding to the gray shaded box in Figure 2.5C, in control and NuMA-KO+STLC cells.

C) Pole-to-pole distance 9 min after anaphase onset, when spindle elongation has largely ceased, in control and NuMA-KO+STLC cells.

D) Chromosome segregation distance 9 min after anaphase onset, when chromosome segregation has largely ceased, in control and NuMA-KO+STLC cells. For (A)-(D), each dot represents one cell. Data include the same 20 control and 18 NuMA-KO+STLC cells shown in Figures 2.5B-C, pooled from 4 independent experiments. ****, $p < 0.00005$, n.s., not significant, two-sample t-test. Error bars indicate mean \pm s.d.

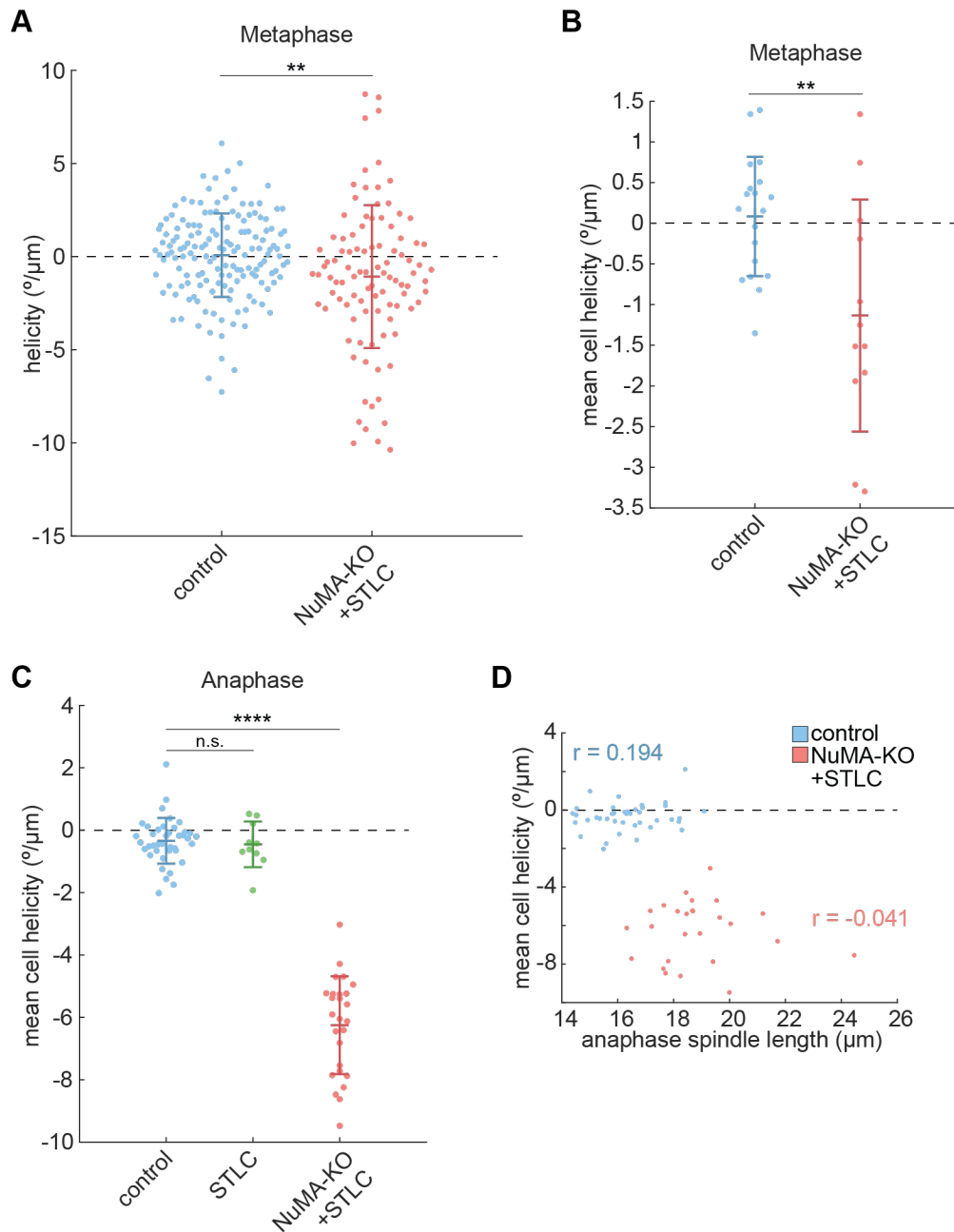


Figure 2.11. Additional analysis of spindle twist in control and doubly inhibited spindles, related to Figure 2.5.

A) Helicity of individual metaphase k-fibers, measured in degrees rotated around the pole-to-pole axis per μm traversed along the pole-to-pole axis. Each dot represents one k-fiber. The mean helicity of control k-fibers is $0.08^{\circ}/\mu\text{m}$, while NuMA-KO+STLC k-fibers have a left-handed average helicity of $-1.08^{\circ}/\mu\text{m}$. $n = 155$ k-fibers from 19 cells (control) and 99 k-fibers from 12 cells (NuMA-KO+STLC), pooled from 3 (control) or 2 (NuMA-KO+STLC)

independent experiments. **, $p = 0.0027$, two-sample t-test. Error bars indicate mean \pm s.d.

B) Mean helicity of metaphase k-fibers per cell (each dot represents one cell), including the same data as (A). Metaphase twist is not consistently left- or right-handed for control or NuMA-KO+STLC spindles. **, $p = 0.0039$, two-sample t-test. Error bars indicate mean \pm s.d.

C) Mean helicity of anaphase interpolar bundles per cell (each dot represents one cell), including the same control and NuMA-KO + STLC cells as Figures 2.5E-F. NuMA-KO+STLC spindles all exhibit left-handed twist, while twist in control and STLC-treated spindles is not consistently left- or right-handed. $n = 40$ cells (control), 10 cells (STLC), and 26 cells (NuMA-KO + STLC), pooled from 5 (control and NuMA-KO + STLC) or 3 independent experiments (STLC). ****, $p < 0.00005$; n.s., not significant; two-sample t-test. Error bars indicate mean \pm s.d.

D) Scatterplot of anaphase spindle length vs. mean helicity of interpolar bundles (each dot represents one cell), including the same data as (C) and Figures 2.5E-F. Mean helicity is not correlated with the extent of anaphase spindle elongation for either control or NuMA-KO+STLC cells, suggesting that spindles do not markedly twist or untwist as anaphase progresses.

Materials and methods

Experimental model details

All cell lines were generated from an hTERT-RPE1 cell line (female human retinal epithelial cells) stably expressing neomycin-resistant tet-on SpCas9, a gift from I. Cheeseman [106]. Cell lines additionally expressed a puromycin-selectable sgRNA targeting NuMA or dynein heavy chain [27]. All cell lines were cultured at 37° and 5% CO₂ in DMEM/F12 (11320, Thermo Fisher) supplemented with 10% tetracycline-screened FBS (PS-FB2, Peak Serum). Fluorescently tagged proteins were introduced by transduction with blasticidin-resistant GFP-tubulin, mCherry-H2B, or PA-GFP-tubulin lentivirus, produced in HEK293T cells, supplemented with 10 µg/ml polybrene. Cell lines were selected with 5 µg/ml puromycin and 5 µg/ml blasticidin. SpCas9 expression was induced by the addition of 1 µg/ml doxycycline hyclate 4 days before each experiment, refreshed after 24 and 48 h.

Transfection and small molecule treatments

For siRNA knockdowns, cells were transfected with 50 pmol siRNA targeting luciferase as a negative control (5'-CGUACGCGGAAUACUUCGA-3', 48 h), HSET (5'-UCAGAAGCAGCCCUGUCA-3', 48 h) [36], KIF15 (5'-GGACAUAAUUGCAAUAC-3', 24 h) [48], PRC1 (5'-GUGAUUGAGGCAAUUCGAG-3', 24h) [132], or Nuf2 (5'-AAGCATGCCGTGAAACGTATA-3', 48h) [133] using Lipofectamine RNAiMAX (13778075, Thermo Fisher) according to the manufacturer's recommendations. Chromosomes were labeled in the inducible DHC-KO cell line (Figures 2.1C, 2.1I, 2.1J) by incubating cells in 1 µM SiR-DNA and 10 µM verapamil (CY-SC007, Cytoskeleton Inc.)

for 60 min prior to imaging. For photomarking experiments (Figures 2.3D-E), microtubules were labeled by incubating cells with 100 nM SiR-tubulin and 10 μ M verapamil (CY-SC002, Cytoskeleton Inc.) for 60 min prior to imaging. For all experiments, cells were synchronized at the G2/M checkpoint by overnight treatment with 9 μ M of the Cdk1 inhibitor RO-3306. Cells were released into mitosis by 4 washes in warm media, after which cells were imaged from prometaphase (controls, approximately 30 min after washout) or from reaching the turbulent state (NuMA- or DHC-KO, approximately 60 min after washout). Eg5 motor activity was inhibited by addition of S-trityl-L-cysteine (final concentration 5 μ M or 40 μ M as indicated, 164739, Sigma). For experiments where Eg5 was inhibited in wild-type cells, 5 μ M STLC was added to metaphase bipoles (Figure 2.9) or added at anaphase onset (Figure 2.11C). To bypass the spindle assembly checkpoint (Figure 2.1J), the MPS1 inhibitor reversine (final concentration 500 nM, R3904, Sigma) was added 45 min after STLC. F-actin and microtubules were disrupted (Figure 2.2) using Latrunculin A (final concentration 500 nM, L12370, Invitrogen) or nocodazole (final concentration 30 nM, M1404, Sigma-Aldrich), added at the same time as STLC. To measure cell viability, cells were plated in black-walled 96-well plates at 700 cells/well on day 0, doxycycline hyclate (1 μ g/ml) was added to the media on the indicated days, and viability was measured on day 5 using the CellTiter-Glo assay (Promega) according to the manufacturer's instructions. Luminescence was detected using a Veritas Microplate Luminometer (Turner BioSystems).

Microscopy

For live imaging, cells were plated onto #1.5 glass-bottom 35 mm dishes coated with poly-D-lysine (P35G-1.5-20-C, MatTek Life Sciences) and imaged in a humidified stage-top incubator maintained at 37° and 5% CO₂ (Tokai Hit). Fixed and live cells were imaged on a spinning disk (CSU-X1, Yokogawa) confocal inverted microscope (Eclipse Ti-E, Nikon Instruments) with the following components: Di01-T405/488/561/647 head dichroic (Semrock); 405 nm (100 mW), 488 nm (150 mW), 561 nm (100 mW) and 642 nm (100 mW) diode lasers; ET455/50M, ET525/50M, ET630/75M, and ET705/72M emission filters (Chroma Technology); and a Zyla 4.2 sCMOS camera (Andor Technology). Images were acquired with a 100× 1.45 Ph3 oil objective using MetaMorph 7.10.3.279 (Molecular Devices). Photomarking experiments (Figures 2.3D-E) were performed on an OMX-SR inverted microscope (GE Healthcare) with the following components: three PCO Edge 5.5 sCMOS cameras; an environmental chamber maintained at 37° and 5% CO₂ (GE Healthcare); and a Plan ApoN 60× 1.42 oil objective. Photoactivation was performed with a single 20 ms pulse of 405 nm light targeted to a rectangular region of interest.

Immunofluorescence

For immunofluorescence, cells were plated onto acid-cleaned #1.5 25 mm coverslips coated with 0.1% gelatin solution. Cells were fixed in methanol at -20°C for 3 min, washed with TBST (0.05% Triton-X-100 in TBS), and blocked with 2% BSA in TBST. Antibodies were diluted in TBST + 2% BSA and incubated overnight at 4°C (primary antibodies) or 45 min at room temperature (secondary antibodies). DNA was labeled with 1 µg/ml Hoechst 33342 for 20 min, prior to mounting on slides with ProLong Gold Antifade

Mountant (P36934, Thermo Fisher). The following primary antibodies were used: mouse anti- α -tubulin (1:1,000, T6199, Sigma; RRID:AB_477583), rat anti- α -tubulin (1:500, MCA77G, Bio-Rad; RRID:AB_325003), rabbit anti-NuMA (1:300, NB500-174, Novus Biologicals; RRID:AB_10002562), and mouse anti- α -tubulin AlexaFluor 488 conjugate (1:50, added with secondary antibodies, 8058S, Cell Signaling Technology; RRID:AB_10860077). The following secondary antibodies were used at a 1:400 dilution: goat anti-rabbit AlexaFluor 568 and AlexaFluor 647 (A-11011 and A-21244, Thermo Fisher; RRID:AB_143157 and RRID:AB_2535812), goat anti-rat AlexaFluor 488 (A-11006, Thermo Fisher; RRID:AB_2534074), and goat anti-mouse AlexaFluor 488 (A-11001, Thermo Fisher; RRID:AB_2534069). Brightness/contrast for each channel was scaled identically within each immunofluorescence experiment shown.

Western blotting

Cells in 6-well plates were lysed, and protein extracts were collected after centrifugation at 4°C for 30 min. Protein concentrations were measured using a Bradford assay kit (Bio-Rad), and equal concentrations of each sample were separated on a 3-8% Tris-Acetate or 4-12% Bis-Tris gel (Invitrogen) by SDS-PAGE and transferred to a nitrocellulose membrane. Membranes were blocked with 4% milk, incubated in primary antibodies overnight at 4°C, and incubated with HRP-conjugated secondary antibodies for 1 h. Proteins were detected using SuperSignal West Pico or Femto chemiluminescent substrates (Thermo Fisher). The following primary antibodies were used: mouse anti- α -tubulin (1:5,000, T6199, Sigma; RRID:AB_477583), rabbit anti-NuMA (1:1,000, NB500-174, Novus Biologicals; RRID:AB_10002562), rabbit anti-KIF15 (1:500, A302-706A,

Bethyl Laboratories; RRID:AB_10748366), mouse anti-KifC1 (M-63; 1:500, sc-100947, Santa Cruz Biotechnology; RRID:AB_2132540), mouse anti-NDC80 (1:500, NB100-338, Novus Biologicals; RRID:AB_10000917), and mouse anti-PRC1 (1:300, 629002, Biologend; RRID:AB_2169531). The following secondary antibodies were used at a 1:10,000 dilution: goat anti-mouse IgG-HRP (sc-2005, Santa Cruz Biotechnology; RRID:AB_631736) and mouse anti-rabbit IgG-HRP (sc-2357, Santa Cruz Biotechnology; RRID:AB_628497).

Cell confinement

Cells were confined as described previously [115], using a suction cup device adapted from Le Berre et al. [114]. Briefly, PDMS pillars 5 μm in height (200 μm diameter, 700 μm spacing) were attached to a 10 mm-diameter coverslip, and were lowered onto cells using negative pressure generated manually using a 1 ml syringe. Pillars were gradually lowered onto cells over ~ 2 min, and maximum confinement (at a cell height of 5 μm) was sustained for an additional 20 min. Cells were excluded from analysis if the final confined height was >5 μm , suggesting that the cell's surroundings on the coverslip prevented full confinement, or if the separation between sister chromosomes became indistinguishable, suggesting chromosome decondensation, e.g. resulting from cell rupture.

Quantification of spindle shape and failure

Spindle length and width were measured manually using the line selection tool in FIJI (ImageJ version 2.0.0-rc-69/1.52p). For control and NuMA-KO+STLC cells, length

was measured as the distance between the two spindle poles, and width was measured at the widest part of the spindle across the metaphase plate. Aspect ratio was determined by dividing length by width. For turbulent NuMA-KO spindles and compressed spindles after structural failure, spindle axis directions were approximated from chromosome positions, and length and width were measured as the longest extent of spindle microtubules in these directions (see Figure 2.1E). For Figures 2.1F-H, spindle dimensions were measured after reaching a bipolar metaphase (control and NuMA-KO+STLC) or 45 min after the start of imaging (NuMA-KO). For Figures 2.1I, 2.1J, and 2.2B, spindle architecture and anaphase entry were scored at 90 min after STLC addition, and cells that were imaged for <90 min were excluded. Spindle failure (Figure 2.4F and Figure 2.9C) was defined as a loss of visible connectivity between k-fibers and the pole.

Quantification of NuMA levels

To compare NuMA intensity in control cells versus cells in which NuMA knockout had been induced, we quantified sum intensity projections of 21 z-planes spaced 0.35 μm apart. Using a custom MATLAB program (version R2020a), cell areas were segmented using a low tubulin threshold, and mean NuMA and tubulin intensities were measured within this region. NuMA intensities were normalized for each cell by dividing by the corresponding tubulin intensity. For the +DOX condition, only spindles with a disorganized phenotype (a single snapshot of a turbulent spindle) were analyzed, consistent with the criterion of spindle turbulence used for all live imaging experiments.

Fluorescence intensity profiles

Fluorescence intensity profiles along the pole-to-pole axis (Figures 2.3B-C) were quantified from sum intensity projections of 21 z-planes spaced 0.35 μm apart. Using a custom MATLAB program, images of tubulin fluorescence were passed through a median filter (3x3 pixels) and spindle areas were segmented using a tubulin intensity threshold. Based on the major axis angle of the segmented spindle, images were rotated so that the pole-to-pole axis was horizontal. At each of 21 positions (0%, 5%, 10%...100%) along the pole-to-pole axis, the mean tubulin and Hoechst intensities were calculated from the 1-pixel-wide column of all pixels contained within the spindle boundaries. Finally, these 21-point profiles were normalized to the maximum value for each spindle.

Flux rate

SiR-tubulin image sequences were aligned using a Rigid Body transformation, and the corresponding PA-GFP-tubulin image sequence was registered using the MultiStackReg plugin (version 1.45) to remove overall spindle drift. FIJI's segmented line selection tool with spline fitting was used to trace 2-3 k-fibers per spindle, and kymographs were generated from the PA-GFP-tubulin channel for each k-fiber using the Multi Kymograph plugin with a linewidth of 3 pixels. In MATLAB, the intensity values in each kymograph were smoothed with a moving mean calculated over a sliding 5-pixel window, and the position of maximum intensity was determined for each timepoint. Linear regression was performed on the positions of these maxima to determine the rate that the photomark moved polewards, using the MATLAB fit function of type 'poly1'.

Time correlation function of spindle shape

Timelapse image sequences were registered in FIJI using the Rigid Body option of the StackReg plugin [134]. Spindles were segmented in FIJI by smoothing, despeckling, background subtraction, and thresholding with Otsu's method. In MATLAB, thresholded binary image sequences were cropped to a 33x33 μm box centered at the spindle's centroid, and spindle masks were further refined by filling holes and removing small objects. The correlation coefficient was calculated, using the MATLAB corr2 function, between all pairs of binarized frames separated by lag time Δt , where $\Delta t = 0.5, 1, 1.5, \dots 9.5$ min. To determine shape correlation as a function of lag time, correlation coefficients were averaged for each lag time and fit to the exponential function $r = a * e^{(-\frac{1}{\tau}) * lag\ time} + b$ using MATLAB's curve fitting tool [27].

Anaphase segregation rates

Cells analyzed in Figures 2.5B, 2.5C, and 2.10 were imaged every 30 s from late metaphase through telophase. Anaphase onset was defined as the first frame with detectable chromosome separation. In each frame, the distance between the two spindle poles and the distance between the centers of the two chromosome masses were measured manually with the line selection tool in FIJI. Elongation and segregation rates were determined by linear regression of data between $t = 30$ s and $t = 180$ s, using the MATLAB fit function of type 'poly1'.

Microtubule bundle helicity

Helicity was analyzed similarly to the method described in Novak et al. [71]. We acquired z-stacks of GFP-tubulin-labeled spindles from live metaphase and anaphase cells. Z-axis calibration was performed using a FocalCheck slide #1 (F36909, Thermo Fisher), and the preservation of handedness throughout the optical train was validated by imaging a 3mm-diameter spring of known handedness with a 10× objective. Z-stacks were manually rotated in FIJI such that the pole-to-pole axis was horizontal. Image coordinates (x, y, z) were permuted to (z, x, y) in MATLAB, creating a series of spindle cross-sections as if viewed end-on from the pole. The rotated image stacks were background-subtracted and despeckled to facilitate bundle tracking. Spindle poles were marked and individual bundles were traced in FIJI using the MTrackJ plugin [135], with cursor snapping to the bright centroid of a 15x15 pixel box enabled. In MATLAB, tracked bundle and pole positions were transformed so that both poles lay on the x-axis, accounting for spindle tilt. Tracked points were excluded if they lay outside the central 30-70% of the pole-to-pole axis. Bundles were excluded from further analysis if their mean radial distance from the central pole-to-pole axis was $<2 \mu\text{m}$, or if they contained fewer than 20 points (corresponding to a minimum track length of $1.16 \mu\text{m}$). The angle between the first and last point in each bundle track was calculated with respect to the central pole-to-pole axis, and this angle was divided by the distance traversed along the pole-to-pole axis to calculate helicity.

Quantification of chromosome segregation errors

Segregation errors (Figures 2.5G and 2.5H) were determined from z-stacks of mCherry-H2B fluorescence, acquired with 1 μm spacing and covering the entire spindle height at a single timepoint during live imaging. Segregation errors included lagging chromosomes, defined here as one or more chromosomes completely separated from the rest of the chromosome mass, and chromosome bridges, defined here as an extended chromosome pair connecting the two segregating masses.

Statistical analysis

Details of statistical tests and sample sizes (number of cells and number of independent experiments) are provided in figure legends. Fisher's exact tests were performed to compare categorical datasets, using the fishertest function in MATLAB for 2x2 comparisons and the fisher.test function in R (version 4.0.1) for 2x3 comparisons. Two-sided two-sample t-tests were performed to compare continuous datasets using the ttest2 function in MATLAB, based on the assumption that spindle length and width, flux rate, anaphase segregation rate, and helicity are approximately normally distributed. We used $p < 0.05$ as the threshold for statistical significance. Linear regressions (Figures 2.3E, 2.5B, 2.5C, 2.10A, and 2.10B) and exponential decay fits (Figure 2.4E) were performed in MATLAB.

Acknowledgements

The work presented in Chapter 2 was conducted under the supervision of Sophie Dumont, PhD (UCSF). Additional experiments, not included here, were performed by Nathan Cho (UCSF). We thank Christina Hueschen and Andrea Serra-Marques for inducible RPE1 NuMA-KO and DHC-KO cell lines, Iain Cheeseman and Kara McKinley for reagents, and Dan Needleman and Margaret Gardel for helpful discussions. We thank Christina Hueschen, Rob Phillips, and members of the Dumont lab for critical reading of the manuscript. Photomarking experiments were performed at the UCSF Nikon Imaging Center with assistance from Kari Herrington and SoYeon Kim, on instruments obtained using funding from the NIH (5R35GM118119), the UCSF Program in Breakthrough Biomedical Research, the Sandler Foundation, the UCSF Research Resource Fund Award, and the Howard Hughes Medical Institute. This work was supported by NIH DP2GM119177, NIH R01GM134132, NIH R35GM136420, NSF CAREER 1554139, and NSF 1548297 Center for Cellular Construction (S.D.); the Chan Zuckerberg Biohub, Rita Allen Foundation and Searle Scholars' Program (S.D.); and an NSF Graduate Research Fellowship, Fannie and John Hertz Foundation Fellowship, and William K. Bowes Jr. & Ute Bowes Discovery Fellowship (L.N.).

**Chapter 3: Torques within and outside the human spindle balance twist at
anaphase**

Abstract

At each cell division, nanometer-scale motors, crosslinkers, and microtubules give rise to the cellular-scale spindle. Although many mitotic motors have been shown to walk in helical paths around microtubules in vitro, the human spindle exhibits only slight global twist. This raises the question of how molecular torques are balanced to build a nearly achiral spindle. Here, we define the mechanisms that generate and resist twist in the anaphase spindle. Live imaging of human MCF10A cells, using confocal and lattice light-sheet microscopy, reveals that their spindles have higher baseline twist than previously characterized cell lines and that it peaks at anaphase. The midzone motors KIF4A and MKLP1, which contribute to anaphase spindle elongation, redundantly contribute to left-handed twist, while LGN and dynein, components of the cortical force-generating machinery, counteract twist. Together, our results demonstrate that factors both within the spindle and at the cell periphery generate competing torques to maintain the spindle's slight left-handed twist during chromosome segregation.

Introduction

At each cell division, the cellular-scale spindle self-organizes from nanometer-scale molecular components to divide the genome. While the identities of nearly all these building blocks are known [2], many questions remain about how they together give rise to the architecture, mechanics, and function of the spindle as an ensemble. Mitotic motors, over a dozen species of which are present in the human spindle, illustrate this gap: although the motility and force-generating capacity of many motors have been closely studied *in vitro* [136, 137], it remains poorly understood how motors are regulated in the dense microtubule network of the spindle to give rise to larger-scale microtubule motifs.

Many motors have been found to side-step with a directional preference *in vitro*, resulting in helical motility around the microtubule track. The torque produced by the helical motility of Ncd, one of several mitotic kinesins that crosslink and slide microtubule pairs, is sufficiently strong to twist and coil two microtubules around each other [76]. The plus-end-directed mitotic kinesins Eg5 (a human kinesin-5) [72], Kip3 (a yeast kinesin-8) [74, 126], and ZEN-4 (the *Caenorhabditis elegans* ortholog of the kinesin-6 MKLP1) [73] have a left-handed stepping bias with short helical pitches on the order of $\sim 1 \mu\text{m}$. The minus-end-directed kinesin-14 Ncd [76, 77] as well as mammalian dynein-dynactin-BicD2 and dynein-dynactin-BicDR1 complexes [75], by contrast, have a right-handed stepping bias. These torques would be expected to additively twist the spindle in a left-handed direction, yet the human spindle exhibits only a weak left-handed twist on average [71, 78]. It is not known how these molecular-scale torques are balanced in the spindle.

The spindle's left-handed twist was first quantified in metaphase HeLa and U2OS cells [71]. Spindle twist has been proposed to allow the spindle to accommodate mechanical load along the pole-to-pole axis [78], although its functional importance for chromosome segregation remains to be shown. Twist differs between cell types, with spindles in RPE1 cells having weaker twist than HeLa or U2OS spindles, and between mitotic phases, peaking around anaphase onset [78]. Several motors have been demonstrated to contribute to spindle twist in the expected direction. Inhibiting Eg5 or depleting the kinesin-8 KIF18A reduces the spindle's left-handed twist, suggesting that torques generated by biased motor stepping are relevant to the twist of the spindle as a whole [71, 78]. Only one perturbation has been demonstrated to increase the spindle's left-handed twist: our previous work described in Chapter 2 revealed that in RPE1 spindles, knockout of dynein's targeting factor NuMA, combined with Eg5 inhibition to maintain spindle bipolarity, leads to strong left-handed twist at anaphase [59]. Although it remains unknown how NuMA deletion increases spindle twist, the finding that twist can be either strengthened or abrogated by depleting various spindle factors raises the question of how opposing torques are generated and resisted to set spindle twist.

Here, we ask how torques are balanced so that the spindle exhibits only slight global twist. We find that spindles in the human mammary epithelial cell line MCF10A exhibit stronger baseline twist than previously characterized cell lines, and show via lattice light-sheet microscopy that this twist peaks in anaphase. The motors KIF4A and MKLP1, which redundantly contribute to spindle elongation at anaphase, are also redundantly required for left-handed spindle twist, while the cortical force-generating machinery of LGN and dynein counteract this twist. Finally, we observe that the actin cytoskeleton is

required for the anaphase spindle's left-handed twist. Together, our results show that factors both within the spindle and at the cell periphery generate competing torques to maintain the spindle's slight left-handed twist at anaphase.

Results

MCF10A cells exhibit high baseline twist that peaks in late metaphase and anaphase

To investigate torque regulation in the spindle, we sought to identify a cell line in which spindles exhibited higher baseline twist than that observed in previously characterized cell lines. We reasoned that because twist differs between the human cell lines RPE1, HeLa, and U2OS [59, 71, 78], other human cell lines may exhibit stronger twist, and that this would allow us greater dynamic range to study factors that both increase and decrease twist. We quantified twist using the optical flow method [78] in which we live-imaged full spindle volumes, computationally rotated the images to view the spindle along the pole-to-pole axis, and calculated the displacement fields of pixel intensities between successive frames from 30% to 70% of the pole-to-pole axis (Figure 3.1A). These flow vectors were converted to polar coordinates and averaged to produce a single twist value per spindle. We found that the non-transformed mammary epithelial cell line MCF10A [138] met our criterion, with visually apparent left-handed twist in unperturbed cells at anaphase. Quantifying twist, we found that MCF10A cells labeled with either SiR-tubulin or overexpression of GFP-tubulin exhibited significant left-handed twist (negative helicity), while the twist of anaphase RPE1 and U2OS spindles did not significantly differ from 0 (Figure 3.1B). Although U2OS cells were previously reported to exhibit left-handed twist [71], our inability to detect twist here may be due to the difference in mitotic stage or to the reduced signal-to-noise ratio of the spindle midzone in horizontal spindles labeled with GFP-tubulin rather than GFP-PRC1.

Our comparison between different human cell lines was performed by live confocal imaging of a single timepoint per cell, leading us to wonder how twist changes during

mitotic progression in MCF10A spindles. To image dividing cells volumetrically at high time resolution, we used lattice light-sheet microscopy (Figure 3.1C). This imaging modality allowed us to obtain isotropic resolution with minimal phototoxicity, ideal for studying three-dimensional spindle architecture over time. Comparing the profiles of 16 cells revealed several novel features of spindle twist. There was an almost 3-fold cell-to-cell variability in twist magnitude, with peak helicities varying from -0.98 to $-2.75^\circ/\mu\text{m}$. Left-handed twist became stronger in the final minutes of metaphase, consistent with previous findings in HeLa and RPE1 cells [78]. Twist was maintained throughout early and mid-anaphase for approximately 3 minutes, before sharply dissipating in late anaphase. Given the sustained period of high twist in the first few minutes of anaphase, and given our previous findings in NuMA-KO and Eg5-inhibited RPE1 cells suggesting anaphase-specific mechanisms of twist regulation [59], we focused thereafter on studying torques in anaphase MCF10A cells.

The midzone motors KIF4A and MKLP1 redundantly promote left-handed twist in the anaphase spindle

We next asked what factors give rise to the spindle's left-handed twist at anaphase. Although the motors Eg5 and KIF18A have been shown to promote left-handed twist at metaphase [71, 78], many mitotic motors undergo changes in localization and function at anaphase, and the molecular basis of anaphase spindle twist has not been studied. As anaphase progresses, several motors and other microtubule-associated proteins become compacted in the spindle midzone where antiparallel microtubules overlap, and midzone-localized motors including KIF4A, Eg5, MKLP1, and MKLP2 redundantly power spindle

elongation [119] (Figure 3.2A). We hypothesized that these plus-end-directed kinesins may generate left-handed torques in the spindle, due to their localization at key microtubule overlaps and due to the left-handed torque generation demonstrated in vitro for the plus-end-directed kinesins tested to date. We first probed the contribution of KIF4A, but siRNA depletion of KIF4A did not significantly change spindle twist compared to a control knockdown (Figures 3.2B-C; Figures 3.5A-B). We also tested the role of MKLP1, since the *C. elegans* ortholog of this motor has been shown to have a left-handed stepping bias in vitro [73]. Although mean spindle helicity increased by $0.34^\circ/\mu\text{m}$ (towards the untwisted mean of $0^\circ/\mu\text{m}$) upon MKLP1 knockdown, this modest effect did not reach statistical significance (Figures 3.2B-C; Figures 3.5C-D). When we co-depleted KIF4A and MKLP1, however, spindles were significantly less twisted with a mean helicity of $-0.38^\circ/\mu\text{m}$ (Figures 3.2B-C; Figure 3.5E). This suggests that in addition to their redundant roles in spindle elongation, the midzone motors KIF4A and MKLP1 redundantly generate left-handed torques to twist the anaphase spindle.

The cortical force-generating machinery counteracts left-handed twist in the anaphase spindle

The torques generated by dynein and the kinesins studied to date should tend to additively twist the spindle in a left-handed direction, yet the spindle exhibits much weaker twist than the helical pitch of these individual motors. Thus, we sought to understand whether any factors are required to oppose left-handed torques in the spindle. Our previous work in RPE1 cells identified NuMA, a large coiled-coil protein that recruits dynein and dynactin to microtubule minus ends (Figure 3.3A) [29], as the first known

factor whose deletion increases the spindle's left-handed twist [59]. Based on this finding, we first tested the hypothesis that dynein regulates spindle twist in the opposite direction from the left-handed torques described above. Depleting dynein heavy chain indeed led to stronger left-handed twist in anaphase MCF10A spindles (Figures 3.3B-C; Figure 3.5F).

As described above, mammalian dynein-dynactin-BicD2 or -BicDR1 complexes have a slight right-handed stepping bias in vitro [75]. Given dynein's minus-end-directed motility, such a stepping bias within the spindle would be expected to add to the spindle's global left-handed twist. We thus considered the possibility that a different pool of dynein—the cortical complexes of NuMA-dynactin-dynein at the cell cortex—could give rise to the increased spindle twist we observed upon dynein depletion. These cortical complexes generate pulling forces on astral microtubules to position the spindle within the cell [139], and we reasoned that they might affect spindle twist in the opposite direction by generating torque from the opposite side of spindle poles. We probed the role of this pool of dynein by depleting LGN, a protein that interacts with membrane-anchored $G\alpha_i$ proteins and one of several factors that recruits NuMA to the cortex during mitosis [140-143]. LGN knockdown increased the spindle's left-handed twist to an average of $-1.21^\circ/\mu\text{m}$, significantly stronger twist than that of control-depleted cells and almost as strong as that of dynein-depleted cells (Figures 3.3B-C; Figure 3.5G). We conclude that the cortical spindle positioning machinery consisting of LGN, NuMA, and dynein counteracts left-handed twist in the anaphase spindle.

The actin cytoskeleton is required for left-handed twist at anaphase

Finally, we probed the contribution of the actin cytoskeleton to spindle twist. Chiral flows of cortical actin have been shown to bias spindle orientation in early embryos of the nematode *C. elegans* and the snail *Lymnaea stagnalis*, serving as the initiating event in left-right symmetry breaking for the developing body plan [144-147]. Furthermore, intrinsic chirality has been demonstrated for the actin cytoskeleton in cultured human fibroblasts [148], and we wondered whether chiral actin structures or flows could contribute to spindle twist. We disrupted F-actin by treating MCF10A cells with latrunculin A (LatA), and found that this abrogated the anaphase spindle's left-handed twist (Figures 3.4A-B). By contrast, treating cells with the ROCK inhibitor Y27632 or the myosin II inhibitor blebbistatin did not affect spindle twist (Figures 3.4A-B). We confirmed the activity of blebbistatin by imaging cells later in anaphase, when it blocked cytokinetic furrow ingression similarly to LatA (Figures 3.5H-I). These results suggest that the actin cytoskeleton, but not actomyosin contractility, are required for the anaphase spindle's left-handed twist, and that the contribution of actin to mammalian spindle twist is distinct from the myosin-dependent cortical flows that influence cellular chirality in some invertebrate embryos.

To gain insight into the actin cytoskeleton's influence on spindle twist, we labeled actin in dividing MCF10A cells with SPY-actin and determined its localization via live imaging. Despite a recent report that actin filaments accumulate around centrosomes in early anaphase [149], we could not detect centrosome-localized actin in anaphase MCF10A cells, and instead observed SPY-actin signal only at the cell periphery (Figure 3.4C). Since the dominant pool of actin was cortical, we tested the interaction between

the effects of actin and cortical force generators on spindle twist. Combining dynein heavy chain knockdown with LatA treatment, spindle twist was similar to that of controls and intermediate between the siDHC- and LatA-alone conditions (Figures 3.3C and 3.4B), suggesting that the left-handed contribution of actin and the right-handed contribution of the spindle positioning machinery are independent. Together, our results suggest that spindle twist is regulated both from the cell cortex and from within the spindle, and that it is controlled by both the actin and microtubule cytoskeletons.

Discussion

In this study we investigate how the spindle, a self-organizing cellular machine, attains its relatively untwisted architecture despite being built by chiral force-generators. Our work represents the first investigation of spindle twist at anaphase, the stage at which the spindle's strongest twist is sustained for minutes (Figure 3.1). We identify spindle components that promote left-handed twist (Figures 3.2 and 3.4) and that counteract it (Figure 3.3), and unexpectedly, we find that twist is controlled both by motors internal to the spindle and by microtubule-associated factors and actin at the cell periphery. Together, our results demonstrate that spindle twist is an emergent phenomenon that integrates inputs from the spindle's broader cellular environment.

We show that the midzone kinesins KIF4A and MKLP1 are redundantly required for the anaphase spindle's left-handed twist, similar to previous findings that the kinesins Eg5 and KIF18A promote left-handed twist at metaphase [71, 78]. We propose that these motors twist the spindle as a consequence of their interactions with microtubule pairs, by coiling microtubules around each other [76]. In support of this model, the *C. elegans* ortholog of MKLP1 has a left-handed stepping bias in vitro [73], although the precise configuration of its interactions with midzone microtubules is not known. Our ongoing work has demonstrated that KIF4A also steps with a left-handed bias around the microtubule track (data not shown), and it interacts with pairs of antiparallel microtubules via complex formation with the crosslinker PRC1 [150-152]. Because these motors are relocalized (KIF4A) and concentrated (KIF4A and MKLP1) at the spindle midzone in anaphase, their contributions to left-handed twist may explain why the spindle is more twisted at anaphase than at metaphase.

In addition to torques generated by motors within the spindle, our results suggest that the cortical force-generating factors LGN and dynein regulate spindle twist from the cell periphery. This mechanism could account for our previous findings in RPE1 cells, in which CRISPR-mediated NuMA-KO led to strong left-handed twist at anaphase [59], because NuMA acts in complex with LGN and dynein in cortical force generation. NuMA knockout may have had a stronger effect than that observed here with siRNA-mediated depletion of LGN or dynein heavy chain because the protein was more strongly depleted, because NuMA plays additional uncharacterized roles in regulating spindle twist, and/or because there are LGN-independent pathways that recruit NuMA to the cortex specifically in anaphase that remain intact after LGN knockdown [141-143]. Another previous study found that dynein inhibition did not increase spindle twist in metaphase HeLa or RPE1 spindles [78]. Our results may differ due to our focus on anaphase spindles, when dynein is more enriched at the cell cortex [153, 154] and when this pool of dynein may be more sensitive to perturbation, or because we depleted dynein with siRNA rather than using the drug dynarrestin.

Although LGN depletion increases spindle twist, we cannot exclude that dynein and NuMA depletion may also lead to increased twist by reducing microtubule crosslinking within the spindle body and thus allowing left-handed kinesins to twist the spindle more strongly. Our results also cannot distinguish whether the cortical force-generating machinery restrains spindle twist via active right-handed torque generation on astral microtubules or by exerting passive forces that merely resist left-handed torques by anchoring astral microtubules. Because mammalian dynein has a right-handed stepping bias *in vitro* [75], however, the former is an exciting possibility. Our demonstration

that LGN and dynein depletion increase the anaphase spindle's left-handed twist, combined with our previous finding that NuMA knockout in a different cell type increases anaphase twist, provide new insight into twist regulation by demonstrating that spindle factors influence twist in opposite directions. Although many motors generate torques that twist the spindle in a left-handed direction, these torques are opposed—whether actively or passively—by other spindle components.

Finally, we find unexpectedly that the actin cytoskeleton is required for the anaphase spindle's left-handed twist. A previous study found that actin disruption with latrunculin A did not affect twist in metaphase HeLa spindles [71], but similarly to our discussion of dynein above, this discrepancy could be due to a difference in mitotic stage (possibly related to remodeling of the actin cortex at anaphase) or due to the difference in cell type. We cannot attribute the effects of actin on spindle twist to cortical flows or cortical stiffness, because inhibiting actomyosin contractility had no effect on spindle twist. Furthermore, because actin influenced spindle twist in the opposite direction from and independently of dynein (Figures 3.3C and 3.4B), actin does not regulate twist by delocalizing NuMA and dynein from the anaphase cortex, a known consequence of latrunculin treatment [143]. Instead, we propose that the actin cytoskeleton may regulate spindle twist by controlling overall cell shape, as latrunculin A treatment disrupted monolayer integrity and cell spreading. Our results motivate further exploration of spindle twist in a multicellular epithelial context and further molecular dissection of actin-related proteins, since many myosins, formins, and actin filaments themselves are intrinsically chiral [155-158]. Although the underlying mechanisms are not yet clear, our finding that

the actin cytoskeleton affects spindle twist is exciting because it reveals that multiple cytoskeletal systems coordinately affect spindle twist.

In conclusion, our study shows that the anaphase spindle's weak left-handed twist requires both left-handed torque generators and factors that oppose them. The study of spindle twist is a recent area of inquiry, and many open questions remain. For example, it is unclear why twist differs between different cell types (even those from the same species), and it is not known how twist is affected by other potential mechanisms such as microtubule crosslinking, the spindle's torsional rigidity, or the turnover rates of microtubules and microtubule-associated proteins. Finally, it will be interesting to explore potential functions of spindle twist in future work: are there adverse consequences for chromosome segregation if the spindle is too twisted, or not twisted enough? More broadly, our work motivates the study of other cellular structures built from chiral components that co-opt this chirality for their physiological function (for example, chiral actin flows in left-right symmetry breaking [159]), that exhibit chirality that is neutral for their function (such as neutrophil polarization [160]), or that balance chiral elements to restrain asymmetry.

Figures and figure legends

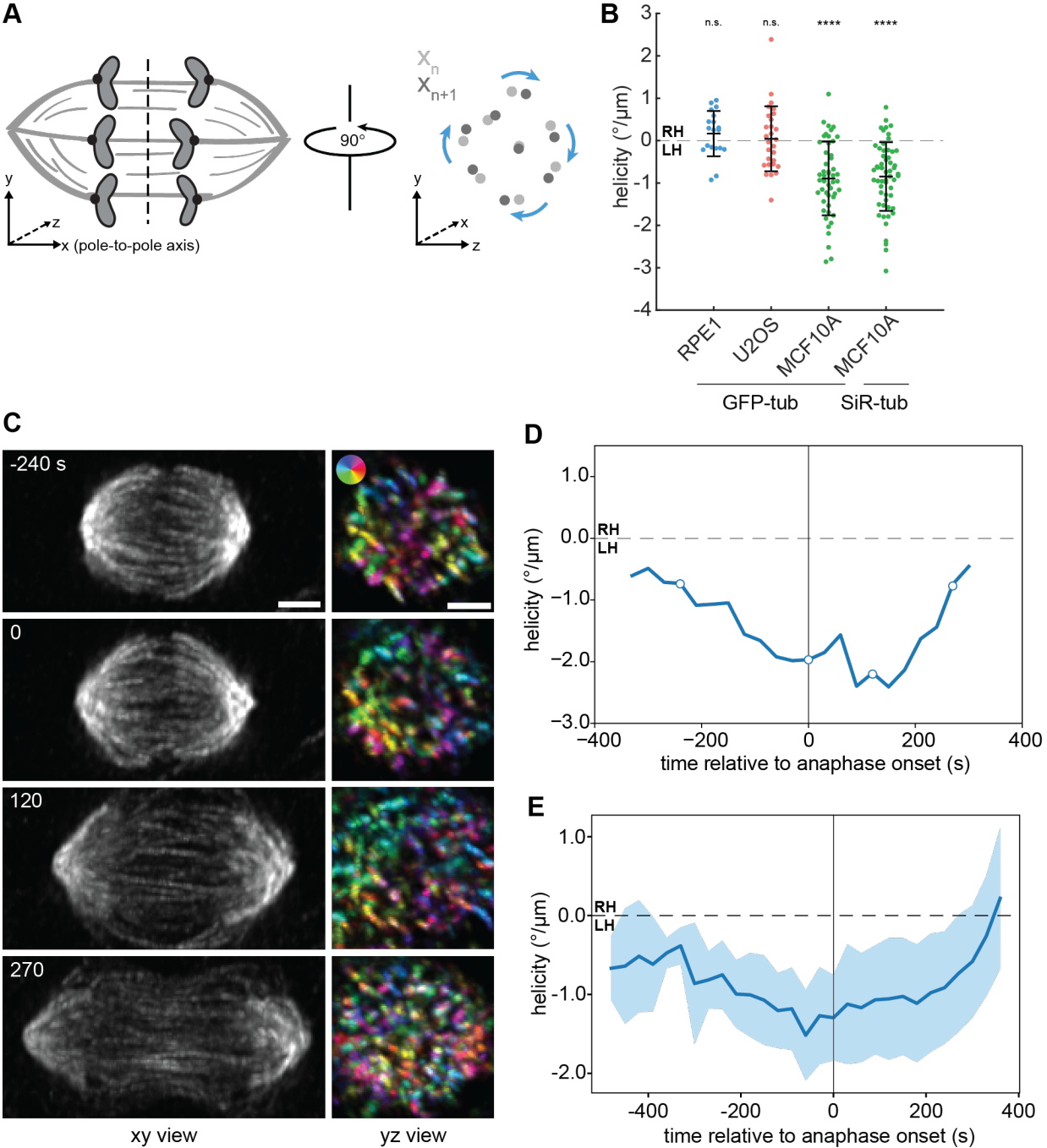


Figure 3.1. MCF10A cells exhibit high baseline twist that peaks in late metaphase and anaphase.

A) Schematic diagram of spindle twist quantification. Three-dimensional image stacks were rotated to view the spindle along the pole-to-pole axis. Farneback optical flow was computed between successive frames, and flow vectors were converted to polar coordinates and averaged for each spindle (see Materials and methods).

B) Spindle helicity (average degrees rotated around the pole-to-pole axis per μm displacement along the pole-to-pole axis) at anaphase in three human epithelial (RPE1, MCF10A) or epithelial-like (U2OS) cell lines, calculated from GFP- α -tubulin or SiR-tubulin intensity. Negative values represent left-handed helicity, and positive values represent right-handed helicity. $n = 19, 28, 49,$ and 56 spindles pooled from $N = 2, 3, 5,$ and 5 independent experiments for RPE1 GFP-tub, U2OS GFP-tub, MCF10A GFP-tub, and MCF10A SiR-tub, respectively. n.s., not significant; ****, $p = 3.44 \times 10^{-9}$ (MCF10A GFP-tubulin) or $p = 1.68 \times 10^{-10}$ (MCF10A SiR-tubulin), two-tailed one-sample t-test.

C) Lattice light-sheet images of the same MCF10A cell, labeled with SiR-tubulin, at four different timepoints. The xy view (left) shows maximum intensity projections of the entire spindle region. The yz view (right) shows maximum intensity projections between 30% and 70% of the pole-to-pole axis for the same image volumes after rotating them 90° . Colors indicate directions of Farnebäck optical flow vectors, according to the color legend shown in the top image. Scale bars = $3 \mu\text{m}$.

D) Helicity over time, calculated from lattice light-sheet images, for the MCF10A spindle shown in (C). The four timepoints in (C) are indicated by open circles.

E) Helicity over time of MCF10A spindles, calculated from time-lapse lattice light-sheet images. The center line and shaded region represent the mean \pm s.d. of 4-16 spindles, depending on the timepoint.

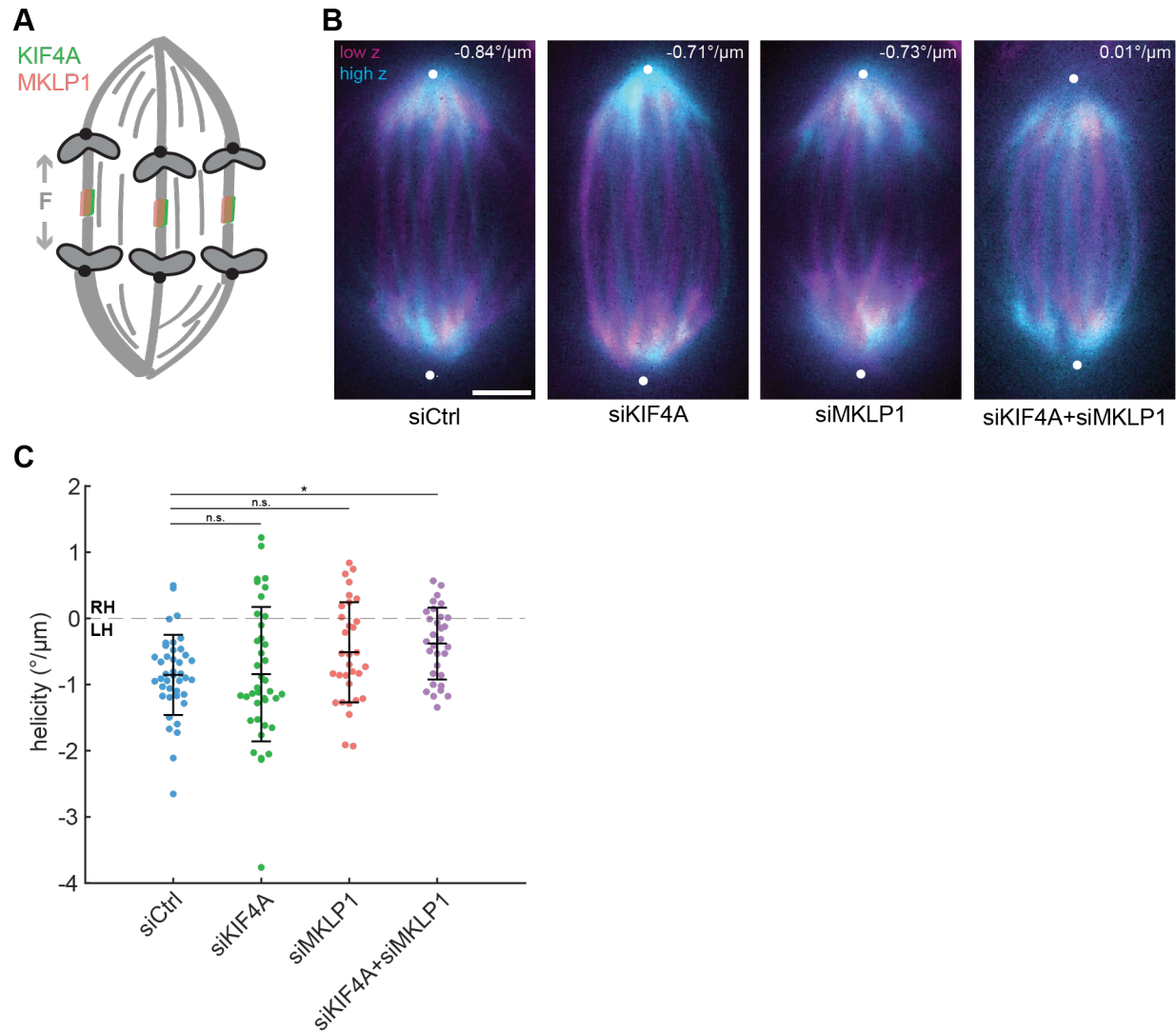


Figure 3.2. The midzone motors KIF4A and MKLP1 redundantly promote left-handed twist in the anaphase spindle.

A) Schematic diagram of KIF4A and MKLP1 localization to the anaphase spindle midzone. Gray arrows indicate outward sliding forces that drive spindle elongation.

B) Live confocal images of MCF10A anaphase spindles labeled with SiR-tubulin. Maximum intensity projections of a low region (-4.5 to -2.5 μm relative to spindle midplane, magenta) and a high region (2.5 to 4.5 μm relative to spindle midplane, cyan) are overlaid. The helicity of each spindle is indicated in the top right. Positions of spindle poles (not visible in these high and low z-planes), manually assigned based on tubulin intensity, are indicated by white circles. Scale bars = 3 μm .

C) Spindle helicity at anaphase in the indicated conditions, calculated from SiR-tubulin intensity. $n = 41, 39, 32,$ and 31 spindles pooled from $N = 4$ independent experiments each. $*p = 0.044$, one-way ANOVA with post-hoc Tukey-Kramer test.

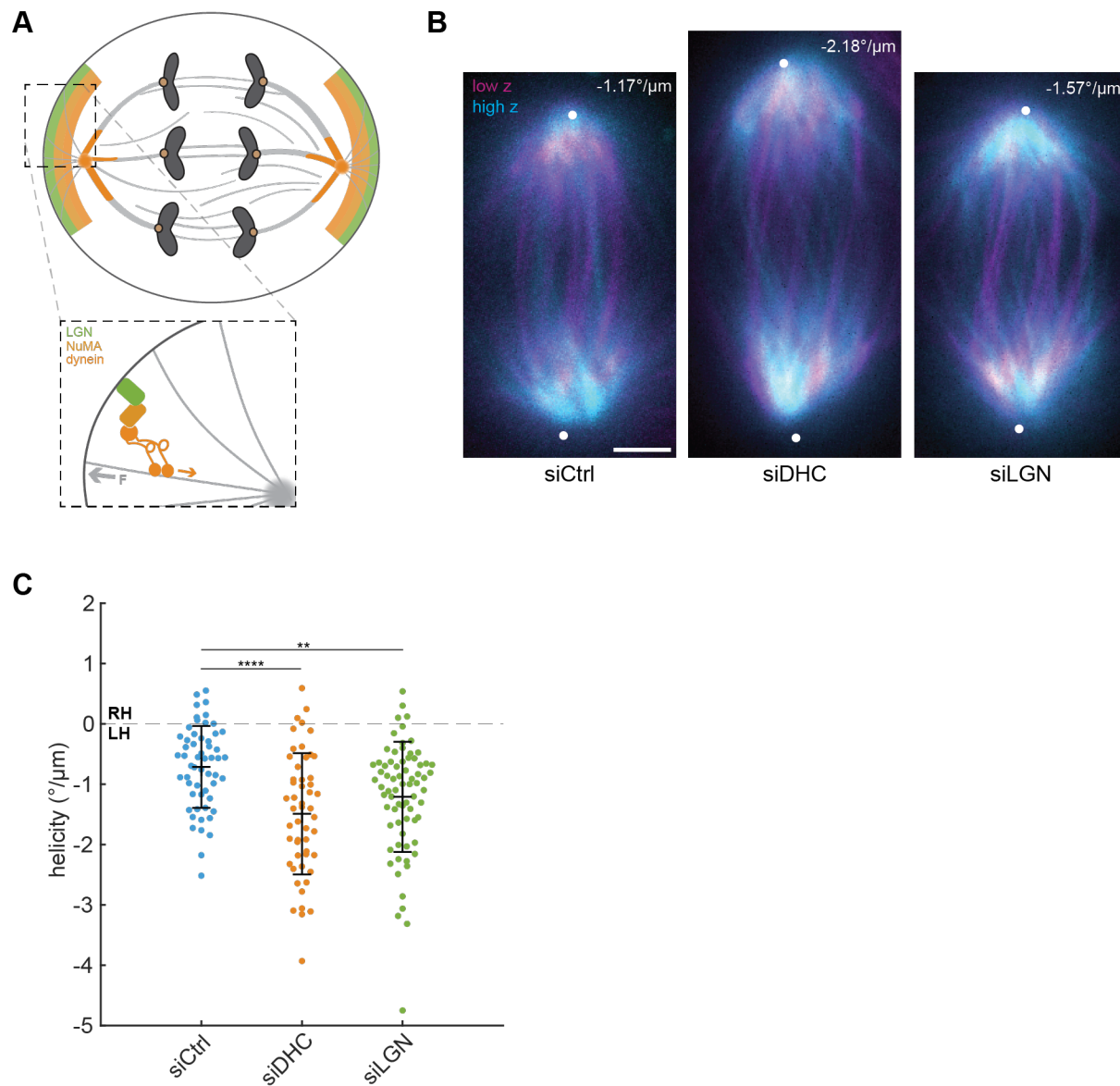


Figure 3.3. The cortical force-generating machinery counteracts left-handed twist in the anaphase spindle.

A) Schematic diagram of LGN, NuMA, and dynein localization in anaphase cells. Dynein and NuMA cluster and localize to spindle poles, while LGN-NuMA-dynein complexes localize to cortical crescents where they exert pulling forces on astral microtubules. The orange arrow indicates direction of dynein stepping, and the gray arrow indicates direction of force on astral microtubules.

B) Live confocal images of MCF10A anaphase spindles labeled with SiR-tubulin. Maximum intensity projections of a low region (-4.5 to $-2.5 \mu\text{m}$ relative to spindle midplane, magenta) and a high region (2.5 to $4.5 \mu\text{m}$ relative to spindle midplane, cyan) are overlaid. The helicity of each spindle is indicated in the top right. Positions of spindle

poles (not visible in these high and low z-planes), manually assigned based on tubulin intensity, are indicated by white circles. Scale bars = 3 μm .

C) Spindle helicity at anaphase in the indicated conditions, calculated from SiR-tubulin intensity. $n = 56, 52,$ and 72 spindles pooled from $N = 5, 4,$ and 6 independent experiments, respectively. $****p = 1.22 \times 10^{-5}; **p = 0.0043$; one-way ANOVA with post-hoc Tukey-Kramer test.

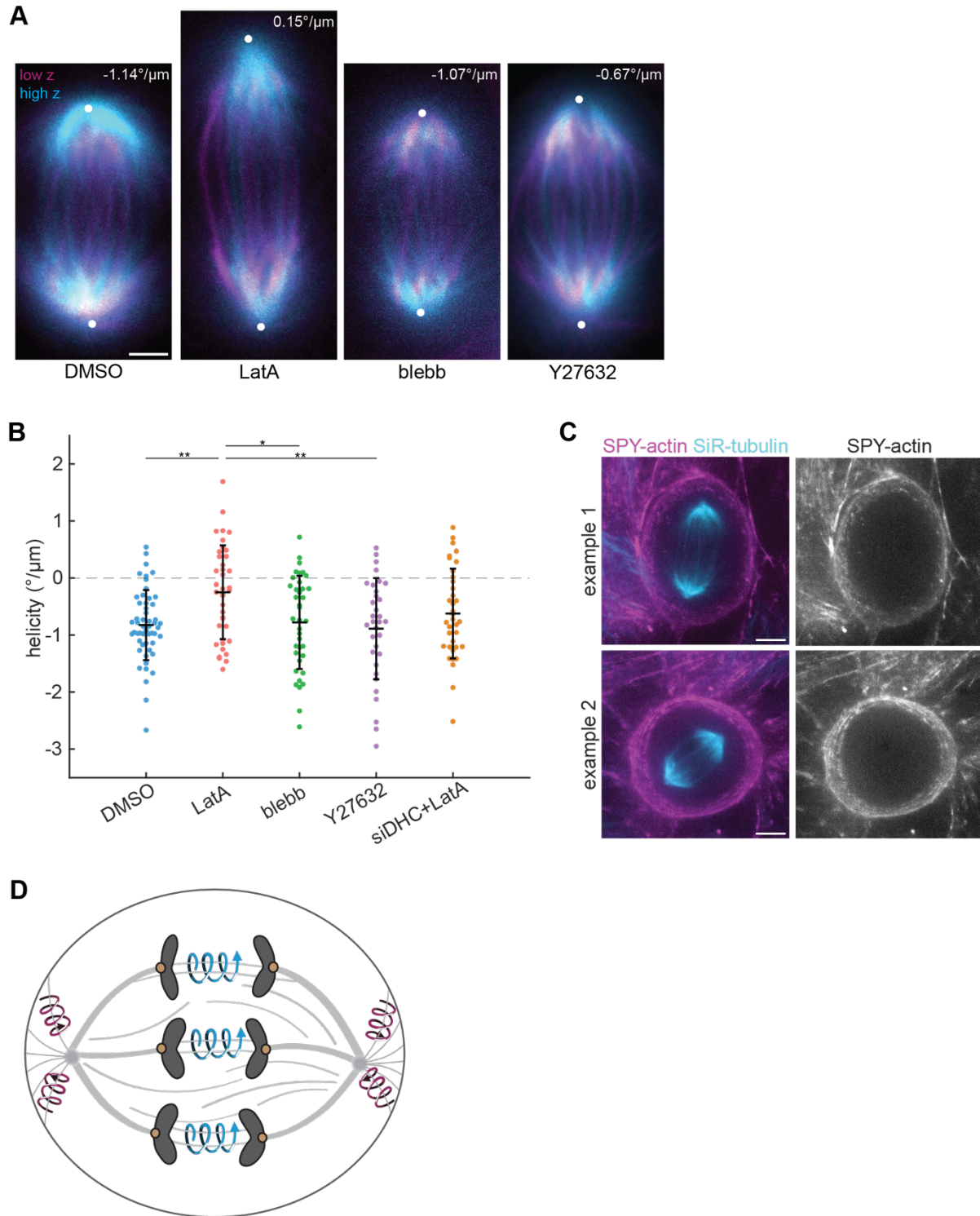


Figure 3.4. The actin cytoskeleton, but not actomyosin contractility, are required for left-handed twist at anaphase.

A) Live confocal images of MCF10A anaphase spindles labeled with SiR-tubulin. Maximum intensity projections of a low region (-4.5 to -2.5 μm relative to spindle

midplane, magenta) and a high region (2.5 to 4.5 μm relative to spindle midplane, cyan) are overlaid. The helicity of each spindle is indicated in the top right. Positions of spindle poles (not visible in these high and low z-planes), manually assigned based on tubulin intensity, are indicated by white circles. Scale bars = 3 μm .

B) Spindle helicity at anaphase in the indicated conditions, calculated from SiR-tubulin intensity. $n = 53, 39, 38, 33,$ and 36 spindles pooled from $N = 5, 4, 4, 3,$ and 4 independent experiments, respectively. $**p = 0.0040$ for DMSO vs. LatA; $*p = 0.0231$ for LatA vs. blebbistatin; $**p = 0.0045$ for LatA vs. Y27632; one-way ANOVA with post-hoc Tukey-Kramer test.

C) Live confocal images (maximum intensity projections of 10 μm z-stacks) of control anaphase MCF10A cells labeled with SPY-actin and SiR-tubulin. Scale bars = 5 μm .

D) Proposed model for twist regulation in the anaphase spindle. Motors within the spindle midzone generate left-handed torques (blue arrows), which are counteracted by LGN-NuMA-dynein complexes at the cell cortex (magenta arrows) to establish a spindle that exhibits only weak global left-handed twist.

Supplemental figures and figure legends

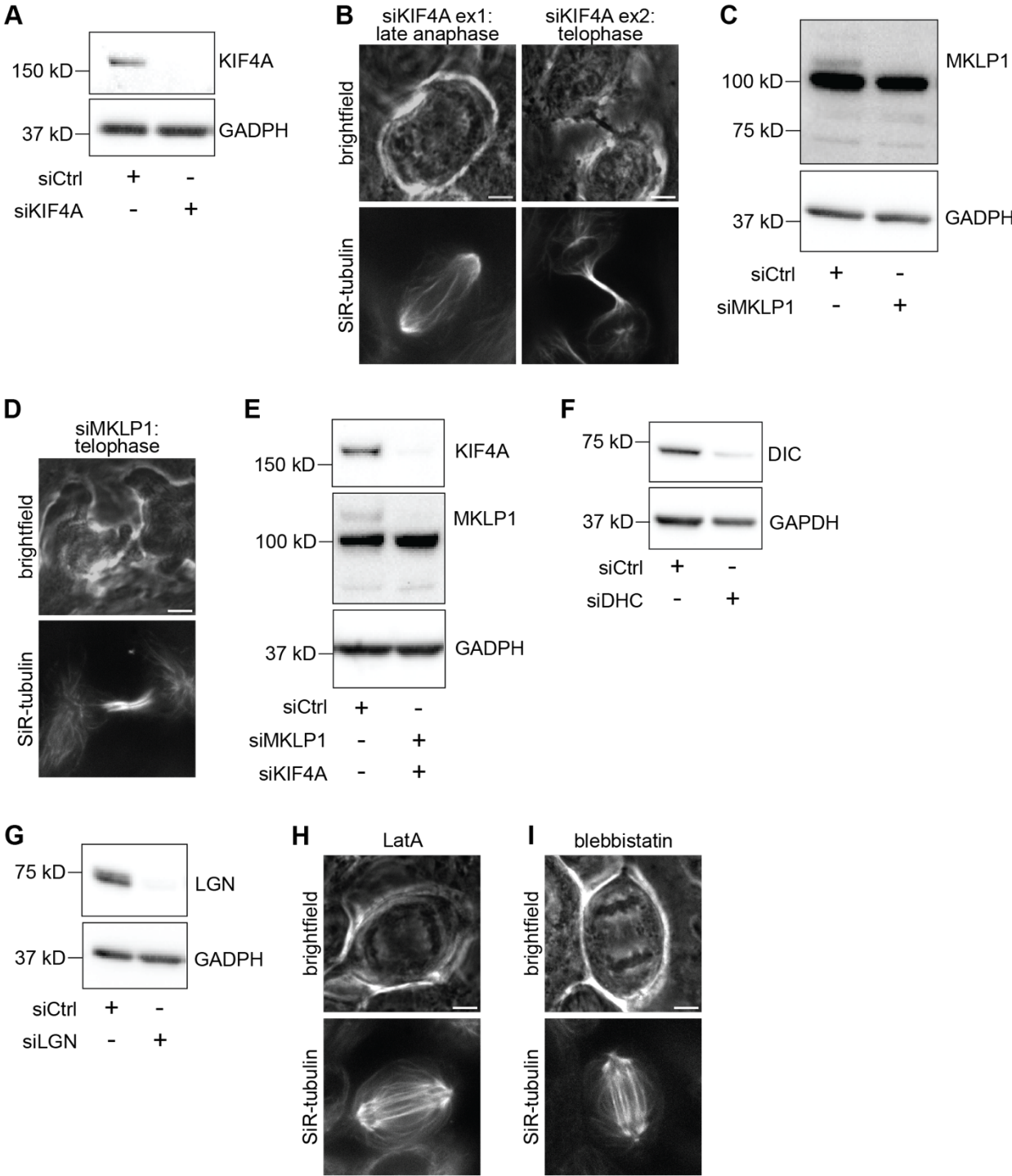


Figure 3.5. Validation of RNAi depletions and drug treatments.

A) Western blot of KIF4A levels in MCF10A cells transfected with a control (luciferase) or KIF4A siRNA for 48 hours. GAPDH is shown as a loading control.

B) Live confocal images of the KIF4A knockdown phenotype. In late anaphase, the spindle midzone elongates past its usual length, and in telophase the midbody is extended. Scale bars = 5 μ m.

C) Western blot of MKLP1 levels in MCF10A cells transfected with a control (luciferase) or MKLP1 siRNA for 48 hours. GAPDH is shown as a loading control.

D) Live confocal images of the MKLP1 knockdown phenotype. Cells fail to form a midbody during cytokinesis. Scale bar = 5 μ m.

E) Western blot of KIF4A and MKLP1 levels in MCF10A cells transfected with a control (luciferase) or KIF4A and MKLP1 siRNAs for 48 hours. GAPDH is shown as a loading control.

F) Western blot of dynein intermediate chain (DIC) levels in MCF10A cells transfected with siRNA targeting luciferase (control) or dynein heavy chain for 48 hours. DIC depletion is correlated with DHC depletion [161]. GAPDH is shown as a loading control.

G) Western blot of LGN levels in MCF10A cells transfected with a control (luciferase) or LGN siRNA for 48 hours. GAPDH is shown as a loading control.

H) Live confocal images of the phenotype after addition of latrunculin A to a concentration of 500 nM. No furrow formation is visible even at late anaphase. Scale bar = 5 μ m.

I) Live confocal images of the phenotype after addition of blebbistatin to a concentration of 25 μ M. No furrow formation is visible even at late anaphase. Scale bar = 5 μ m.

Materials and methods

Cell culture

U2OS cells (female human osteosarcoma cells) were a gift from Samara Reck-Peterson, and hTERT-RPE1 cells (female human retinal epithelial cells) were a gift from Bo Huang. Both cell lines were cultured in DMEM/F12 (Thermo Fisher 11320) supplemented with 10% fetal bovine serum (Gibco 10438026). MCF10A cells (female human mammary epithelial cells) were purchased from ATCC (CRL-10317) and cultured as recommended by ATCC in MEGM (Lonza CC-3150) supplemented with bovine pituitary extract, insulin, hydrocortisone, and human epidermal growth factor according to the manufacturer's instructions, and 100 ng/ml cholera toxin (Sigma-Aldrich C8052). All cells were maintained at 37° and 5% CO₂.

Transfection and small molecule treatments

For siRNA knockdowns, cells were transfected with siRNA targeting luciferase as a negative control (5'-CGUACGCGGAAUACUUCGA-3', 50 pmol), LGN (Dharmacon ON-TARGETplus SMARTpool, L-004092-00-0005, 100 pmol), dynein heavy chain (5'-AAGGATCAAACATGACGGAAT-3', 50 pmol) [97, 162], MKLP1 (pool of 3 sequences, Santa Cruz Biotechnology sc-35936, 50 pmol), or siKIF4A (pool of 3 sequences, Santa Cruz Biotechnology sc-60888, 50 pmol) for 48 hours using Lipofectamine RNAiMAX (Thermo Fisher 13778075) according to the manufacturer's recommendations. GFP- α -tubulin was expressed in RPE1, U2OS, and MCF10A cells by infection with BacMam virus. The GFP- α -tubulin coding sequence was cloned into the pEG BacMam vector (a gift from Eric Gouaux, Addgene plasmid #160451), recombinant bacmid DNA was

generated in DH10Bac cells (Thermo Fisher 10361012), and isolated bacmid DNA was transfected into Sf9 cells (a gift from Yifan Cheng) using Cellfectin II (Thermo Fisher 10362100) for production and amplification of BacMam virus according to a previously described protocol [163]. P2 BacMam virus was added to cells 2 days prior to imaging. Alternatively, tubulin was labeled by adding 100 nM SiR-tubulin and 10 μ M verapamil for 30-60 minutes prior to imaging (Cytoskeleton, Inc. CY-SC002). For acute drug treatments, latrunculin A was added to a final concentration of 500 nM for 20 minutes prior to imaging, blebbistatin was added to a final concentration of 25 μ M for 30 minutes prior to imaging, Y27632 was added to a final concentration of 10 μ M for 30 minutes prior to imaging, and DMSO was added to a final concentration of 0.1% (v/v) for 30 minutes prior to imaging.

Microscopy

For live confocal imaging, cells were plated onto #1.5 glass-bottom 35 mm dishes coated with poly-D-lysine (MatTek Life Sciences P35G-1.5-20-C) 2-3 days prior to imaging, and imaged in a humidified stage-top incubator maintained at 37° and 5% CO₂ (Tokai Hit). Cells were imaged on a spinning disk (CSU-X1, Yokogawa) confocal inverted microscope (Eclipse Ti-E, Nikon Instruments) with the following components: 100 \times 1.45 NA Ph3 oil objective (Nikon); Di01-T405/488/568/647 head dichroic (Semrock); 405 nm (100 mW), 488 nm (150 mW), 561 nm (100 mW) and 642 nm (100 mW) diode lasers; ET455/50M, ET525/50M, ET630/75M, and ET690/50M emission filters (Chroma Technology); and a Zyla 4.2 sCMOS camera (Andor Technology).

For lattice light-sheet microscopy, cells were plated on 25 mm coverslips coated with 200 nm fluorescent beads (Invitrogen FluoSpheres Carboxylate-Modified

Microspheres, Ex/Em 660/680, F8807) to measure point spread functions for deconvolution and to align the lattice light sheet. The coverslip, excitation objective (Thorlabs water dipping lens, 0.65 NA), and detection objective (Zeiss water dipping lens, 1.0 NA) were immersed in approximately 50 ml of culture medium maintained at 37°C and 5% CO₂. The microscope was a modified version of the microscope described in [164] and was controlled with custom LabVIEW software. Cells were labeled with 100 nM SiR-tubulin and 10 μM verapamil, and imaged using a 642 nm laser operating with 200 μW input power at the back pupil of the excitation objective. A dithered harmonic-balanced hexagonal lattice light-sheet pattern [165] with a numerical aperture of 0.35 was used. Each cell was imaged every 30 sec. Emission light was filtered by a Semrock 685 nm band pass filter and captured by a Hamamatsu ORCA-Fusion sCMOS camera. Images were deconvolved, deskewed and rotated on a high performance computing cluster using code available at <https://github.com/abcucberkeley/LLSM5DTools/>.

Western blotting

Cells grown in 6-well plates were lysed, and protein extracts were collected after centrifugation at 4°C for 30 min. Protein concentrations were measured using a Bradford assay kit (Bio-Rad), and equal concentrations of each sample were separated on 4-12% Bis-Tris gels (Invitrogen) by SDS-PAGE and transferred to a nitrocellulose membrane. Membranes were blocked with 4% milk in TBST (TBS + 0.1% Tween 20), incubated in primary antibodies overnight at 4°C, and incubated with HRP-conjugated secondary antibodies for 45 minutes. Proteins were detected using SuperSignal West Pico or Femto chemiluminescent substrates. The following primary antibodies were used: mouse

monoclonal anti-GAPDH (1:1,000, clone 258, Thermo Fisher 437000, RRID:AB_2532218), rabbit anti-KIF4A (1:1,000, Bethyl A301-074A, RRID:AB_2280904), rabbit anti-KIF23 (1:1,000, Thermo Fisher PA5-31773, RRID:AB_2549246), rabbit anti-LGN (1:1,000, Bethyl A303-032A, RRID:AB_10749181), and mouse monoclonal anti-dynein intermediate chain (1:500, clone 74.1, MilliporeSigma MAB1618, RRID:AB_2246059). The following secondary antibodies were used at a 1:10,000 dilution: mouse anti-rabbit IgG-HRP (Santa Cruz Biotechnology sc-2357, RRID:AB_628497) and mouse IgGκ BP-HRP (Santa Cruz Biotechnology sc-516102, RRID:AB_2687626).

Quantification of spindle helicity

Spindles in mid-anaphase, with two clearly separated chromosome masses but before the onset of furrowing, were chosen for analysis. Spindles were rotated so that the pole-to-pole axis was horizontal and cropped using the rectangle tool in FIJI. The positions of the two poles were manually assigned. Spindles were resliced along the pole-to-pole axis by permuting the [x,y,z] coordinates to [y,z,x] in MATLAB (MathWorks, version R2022b). Images were pre-processed in Python by subtracting an image blurred with a Gaussian kernel of standard deviation 30 pixels (`scipy.ndimage.gaussian_filter1d`), followed by despeckling with a 3 pixel median filter (`scipy.ndimage.median_filter`). Helicity was quantified using a previously published optical flow method (<https://gitlab.com/IBarisic/detecting-microtubules-helicity-in-microscopic-3d-images>, [78]). Briefly, Farneäck optical flow [166] was calculated between each pair of successive frames lying between 30% and 70% of the pole-to-pole axis. Flow vectors

were converted to polar coordinates, weighted by pixel intensities using the “All pixels weighted helicities” method, and averaged for each spindle.

Statistical analysis

In Figure 3.1, distributions were assessed for a significant difference from 0 twist with two-tailed one-sample t-tests, using the `ttest` function in MATLAB. In Figures 3.2, 3.3, and 3.4, experimental conditions were compared using one-way ANOVA with post-hoc Tukey-Kramer tests, using the `anova1` and `multcompare` functions in MATLAB, based on the assumption that spindle twist is approximately normally distributed within each condition. We used $p < 0.05$ as a threshold for statistical significance. Sample sizes (number of cells and number of independent experiments, ≥ 3) are provided in figure legends.

Acknowledgements

The work presented in Chapter 3 was done under the guidance of Sophie Dumont, PhD (UCSF), in collaboration with Nathan Cho and Caleb Rux (UCSF). We collaborated with Gaoxiang Liu, PhD and Srigokul Upadhyayula, PhD (UC Berkeley) to perform the lattice light-sheet imaging. In vitro experiments on the motor KIF4A, aspects of this work not included in this dissertation, were performed by Yifei He under the supervision of Ahmet Yildiz, PhD (UC Berkeley), using reagents provided by Radhika Subramanian, PhD (Harvard). We thank Stefan Diez, PhD (TU Dresden), Laura Meissner (TU Dresden), and members of the Dumont, Yildiz, and Mehta labs for helpful discussions. We thank Jonathan Fernandes (UC Berkeley) for experimental advice. We thank Ivan Ivanov, PhD, Talon Chandler, PhD, and Shalin Mehta, PhD for assistance with preliminary polarization microscopy imaging. This work was supported by the Fannie and John Hertz Foundation Fellowship (L.N.); American Heart Association Predoctoral Fellowship (N.C.); UCSF Discovery Fellows Program (L.N. and N.C.); the NSF Graduate Research Fellowship (L.N. and C.J.R.); and NIH R35GM136420, NSF 1548297 Center for Cellular Construction, Chan Zuckerberg Biohub, and the UCSF Byers Award (S.D.).

**Chapter 4: The oncogene cyclin D1 promotes bipolar spindle integrity under
compressive force**

Abstract

The mitotic spindle is the bipolar, microtubule-based structure that segregates chromosomes at each cell division. Aberrant spindles are frequently observed in cancer cells, but how oncogenic transformation affects spindle mechanics and function, particularly in the context of the stiffened tumor microenvironment, remains poorly understood. Here, we constitutively overexpress the oncogene cyclin D1 in human MCF10A cells to probe its effects on spindle architecture and response to compressive force. We find that cyclin D1 overexpression increases the incidence of spindles with extra poles, centrioles, and chromosomes. However, it also protects spindle poles from fracturing under compressive forces, a deleterious outcome linked to multipolar cell divisions. Our findings suggest that cyclin D1 overexpression may be adaptive in stiff solid tumors, contributing to its prevalence in cancers such as breast cancer by allowing continued proliferation in mechanically challenging environments.

Introduction

The spindle is the macromolecular machine that segregates chromosomes at each cell division. In mammalian cells, mitotic spindles are bipolar structures with one centrosome at each spindle pole. Errors in cell division are associated with genomic instability and disease, and aberrant spindles are hallmarks of cancer [167]. Extra centrosomes [168-170], continuously evolving karyotypes known as chromosomal instability [171, 172], and multipolar spindles are elevated in tumors across many tissues of origin and diverse cancer genotypes. Oncogenes can also induce defects in spindle assembly even in the absence of gross spindle abnormalities; for example, MYC overexpression prolongs mitosis and increases chromosome segregation errors [173]. Paradoxically, while such multipolar, clustered pseudo-bipolar, or otherwise aberrant spindles are generally adverse for mitotic outcomes [39, 174], they can promote tumorigenesis by increasing genetic diversity [167] and potentially other unknown mechanisms. How oncogenic transformation affects spindle assembly remains poorly understood.

Dividing cells in solid tumors are subject to dramatically different mechanical environments than their counterparts in healthy tissue [175-177]. Spindles in dividing cultured cells often fracture under compressive force, leading to mitotic delays, multipolar anaphases, and subsequent cell death [116, 178-180]. Tumors have been shown to increase in stiffness due to their increased cell density, elevated interstitial fluid pressure [181], and increased extracellular matrix deposition and crosslinking [182], raising the question of how cells in stiff tumors continue to divide. In breast tumors, compressive stress is high enough to deform and damage interphase nuclei [183], and nearby mitotic

cells presumably experience similarly high forces that may interfere with mitotic rounding or spindle assembly. In multicellular tumor spheroid models, compressive stress reduces cell proliferation [184-187] and has been shown to disrupt bipolar spindle assembly in cells that continue to divide [188]. Due to the challenges of making controlled mechanical perturbations at the cellular scale, little is known about whether and how the spindles of transformed cells mechanically differ from wild-type spindles as they adapt to the tumor environment.

Cyclin D1, overexpressed in 50-70% of breast cancers [189], is an oncogene that causes pleiotropic effects in the cell. Acute overexpression of cyclin D1 leads to spindle and karyotypic defects [190], and long-term overexpression is sufficient to drive breast cancer in mice [191]. In addition to its canonical role in complex with CDK4/6 in controlling cell cycle progression at the G1/S transition, cyclin D1 may contribute to tumorigenesis through its roles in cytoskeletal remodeling and CDK-independent transcriptional programs [189]. Many other oncogenes commonly dysregulated in breast cancer, such as Ras and ErbB2, are upstream of cyclin D1 [192-194], making cyclin D1 overexpression a good model to probe changes in spindle mechanics after oncogenic transformation.

Here, we compare control and cyclin D1-overexpressing breast epithelial cells to investigate their spindle architectures and responses to compressive stress. We find that cyclin D1 increases the proportion of spindles containing extra poles, chromosomes, and centrosomes. However, cyclin D1 overexpression also promotes bipolar spindle integrity during cell compression, preventing spindle pole fracture that results in multipolar cell divisions. We propose that cyclin D1 mechanically adapts cell division to the tumor

context, potentially contributing to its prevalence in cancer despite the aberrant spindles it induces.

Results

Constitutive cyclin D1 overexpression promotes aberrant spindle architectures

To determine the effects of cyclin D1 overexpression on spindle architecture, we compared MCF10A breast epithelial cell lines stably overexpressing cyclin D1 or a puromycin resistance gene as a control (Figure 4.1A) [195]. The parental MCF10A cells are diploid and non-transformed, but are sensitive to transformation by a variety of oncogenes [138, 195, 196]. We confirmed overexpression of cyclin D1 by western blot (Figure 4.1B), and used immunofluorescence to quantify spindle pole, centriole, and kinetochore numbers by staining for α -tubulin, centrin, and CREST respectively (Figure 4.1C). While most (94%) control spindles had 2 centrioles at each of 2 spindle poles, supernumerary centrioles were more common in the cyclin D1-expressing cells (20% of cells; Figures 4.1C and 4.2A). These centrioles were either associated with multipolar spindles or clustered into pseudo-bipolar spindles, a known mechanism by which cancer cells adapt to extra centrosomes in order to avoid multipolar divisions [111, 197, 198].

We next counted the kinetochores in each spindle to gain insight into cyclin D1's effect on genomic integrity. Several mechanisms, including the clustering of extra centrosomes [39, 174] and reduced kinetochore-microtubule dynamics [199], have been shown to give rise to aneuploidy and chromosomal instability in cancer cells, while cytokinesis failure leads to larger-scale genomic duplications. Cyclin D1 overexpression was associated with a broader range of chromosome numbers than in controls, with only a small number of cells containing a near-doubling of chromosome number, indicating that it induces aneuploidy (Figure 4.2B). In summary, constitutive overexpression of the oncogene cyclin D1 leads to an increased incidence of spindles with extra poles,

centrioles, and chromosomes, even when cells are allowed to adapt to elevated cyclin D1 over many passages.

Cyclin D1 overexpression promotes bipolar spindle integrity under compressive stress

Although cyclin D1 overexpression gave rise to higher rates of spindle defects (Figures 4.1 and 4.2), it is overexpressed in many tumors such as breast cancers where dividing cells are subject to increased compressive stress [177, 183, 189]. To account for its high prevalence as an oncogene, we hypothesized that cyclin D1 overexpression may alter the spindle's biophysical properties in a manner that is adaptive in the tumor environment. We compared the mechanical robustness of control versus cyclin D1-overexpressing spindles by compressing cells in PDMS-based microfluidic devices and performing live imaging (Figure 4.3A) [200]. Cells were pre-treated with the proteasome inhibitor MG132 to prevent anaphase entry, allowing us to focus on the metaphase spindle's response to compressive stress, and gradually compressed to a final height of 5 μm via a computer-controlled vacuum pump over 4 minutes. Compression was then sustained for an additional 70 minutes. This perturbation was reproducible from cell to cell, reducing spindle height from an average of $10.55 \pm 1.54 \mu\text{m}$ to $4.72 \pm 0.31 \mu\text{m}$ (mean \pm standard deviation of all cells) (Figures 4.3B-C). Spindles in control and cyclin D1-overexpressing cells had indistinguishable average heights prior to compression and were compressed to a similar final height (Figure 4.3C). Spindles also widened and elongated as compression was applied, consistent with previous work [59, 64, 115]. Spindle lengths before compression were similar between the control and cyclin D1 cells, as were spindle lengths at 10 minutes post-compression onset, when spindle shape had

stabilized (Figure 4.3D). Spindles were significantly wider in control cells vs. cyclin D1-overexpressing cells, both before and after compression, but the difference was slight (Figure 4.3E). Thus, our assay directly probes the spindle's intrinsic ability to adapt to a confined geometry, rather than probing the cell's ability to shield the spindle from shape changes under compression.

Control spindle poles fractured into multiple foci within 70 minutes of compression onset 47.4% of the time, with k-fibers detaching and splaying laterally from the original spindle pole (Figures 4.4A-B). Interestingly, bipolar spindles in the cyclin D1-overexpressing line fractured significantly less often, in just 20.8% of compressions (Figure 4.4B). Although these spindles experienced similar compression-induced deformations, most spindles maintained all k-fibers focused into the two original spindle poles.

To probe the consequences of spindle fracture, we imaged cell compression experiments without the addition of MG132 to follow spindles into late mitosis. Fractured spindles were still able to progress to anaphase, but they segregated chromosomes into three or more masses, depending on the number of new poles created by fracture (Figure 4.4C; note the example shown was compressed using 4 μm micropillars). Interestingly, poles that separated from each other as a result of fracture were directly connected by few or no microtubules (Figure 4.4C, white arrow), and cytokinetic furrowing between these fractured poles was disrupted (Figure 4.4C, red arrow). Our results suggest that compressive force on mitotic MCF10A cells often causes spindle poles to fracture, leading to abnormal chromosome segregation at anaphase, but that overexpression of the oncogene cyclin D1 is protective against spindle fracture.

Discussion

Many oncogenes induce aberrant spindle architectures, yet they also promote uncontrolled cell proliferation in tumorigenesis. One explanation for this apparent paradox is that the elevated rate of chromosome mis-segregation in these spindles accelerates karyotype evolution and gives some cells a selective advantage [201]. Here, we describe another mechanism that could contribute to the proliferative advantage induced by some oncogenes. Overexpression of cyclin D1 increases the prevalence of mitotic cells containing extra poles, centrioles, and chromosomes (Figures 4.1 and 4.2), but also reduces the frequency of spindle fracture under compressive stress (Figure 4.4). Our assay was conducted in two-dimensional culture and with compressive force that may differ in magnitude and direction from that experienced by cells in vivo. Indeed, a recent study using HeLa cells found that while confinement-induced cell flattening led to increased pole fracturing, confining cells into elongated, narrow channels was protective against pole fracturing [180]. However, an increase in spindle multipolarity has also been observed in confined HCT116 colorectal cancer cell spheroids [188], suggesting that our assay mimics compressive forces that exist in a crowded three-dimensional environment.

Although the fractured spindles we followed into anaphase segregated chromosomes into more than two masses (Figure 4.4C), many of these mitoses presumably resolved into two daughter cells due to the lack of an anaphase central spindle competent to recruit the cytokinetic machinery between the newly separated poles. However, rapid nuclear envelope reformation at mitotic exit may prevent these multiple DNA masses from merging and lead to genomic instability or cell cycle arrest. Because cyclin D1 overexpression has a protective effect on bipolar spindle integrity

under compressive force, we propose that it helps to prevent multipolar anaphases and may allow cells to continue proliferating in the stiff tumor context. Intriguingly, the cyclin D1 interactors pRb, p27, and p21 have been shown to mediate a G1 arrest in cells subjected to compressive stress [186, 187, 202], suggesting that cyclin D1 levels may affect the likelihood both that cells will continue to divide under compression and that they will complete these divisions successfully.

The mechanisms by which cyclin D1 overexpression protects against spindle fracture remain to be elucidated. Cyclin D1 could regulate other factors involved in the cell's or the spindle's response to compression through its kinase-dependent or transcriptional roles [189]. Frustrated mitotic rounding has been shown to lead to pole fracturing [116], and oncogenic h-Ras^{G12V} has been shown to prevent pole fracture in MCF10A cells by enhancing mitotic rounding under stiff gels [179]. We propose that different mechanisms are at play in the protective effect we observe here, because spindles in cyclin D1-overexpressing cells underwent fewer fractures despite being compressed to the same flattened height as spindles in control cells (Figure 4.3C). Supernumerary centrioles could contribute to the protective effect of cyclin D1 by increasing the density of microtubules and/or pericentriolar material at poles [168, 203, 204]. Indeed, the proportion of bipolar spindles containing extra centrioles was increased from 1.3% of controls to 13.1% in the cyclin D1 cell line (Figure 4.2A), but it remains to be determined whether the pole-protective effect of cyclin D1 occurs specifically in cells with centriole amplification. Finally, other proteins that are differentially regulated during oncogenic transformation (but not specifically downstream of cyclin D1) could affect pole integrity. For example, TPX2 and chTOG, proteins required for spindle pole integrity, are

commonly upregulated in cancer [205-207]. Future work dissecting the mechanism(s) by which cyclin D1 promotes bipolar spindle integrity under compression will be important to predict how generalizable this phenomenon is likely to be among tumors with diverse driver oncogenes.

The biochemical hallmarks of cancer, including anti-apoptotic signaling, metabolic reprogramming, and cell cycle dysregulation, are well-established [208]. By contrast, our knowledge of the biophysical hallmarks of cancer lags behind, and addressing this gap could reveal new insights into disease progression. Our application of controlled, cellular-scale force suggests that cyclin D1 overexpression may adapt dividing cells to the mechanical burdens of the tumor environment. Better understanding the biophysical adaptations of cancer cells could lead to new ways to selectively target these cells for therapeutic gain.

Figures and figure legends

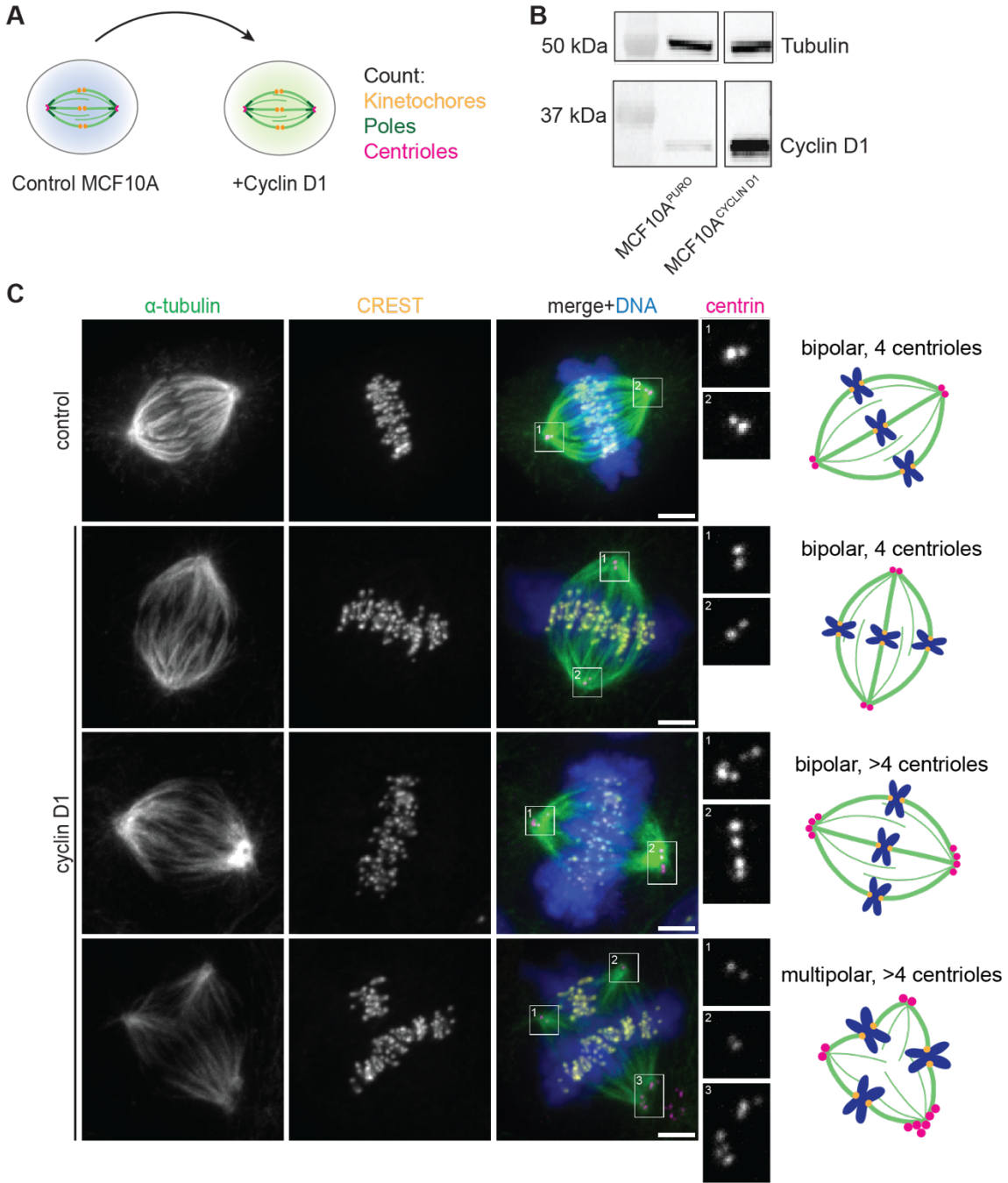


Figure 4.1. Characterization of cells overexpressing cyclin D1.
 A) Schematic diagram of assay. MCF10A cells stably expressing a puromycin resistance gene (control) or cyclin D1 with puromycin resistance were examined by immunofluorescence for changes to metaphase spindle pole, centriole, or kinetochore number.

B) Western blot of α -tubulin and cyclin D1 levels in MCF10A^{PURO} and MCF10A^{CYCLIN D1} cell lines. All images are from the same blot, with intervening lanes removed.

C) Representative confocal immunofluorescence images (maximum intensity projections) of spindles stained for α -tubulin (green), CREST (yellow), centrin (magenta), and Hoechst (blue), with spindle phenotypes cartooned (right). Magnifications of the centrioles at each spindle pole are shown at right. Scale bars = 3 μ m.

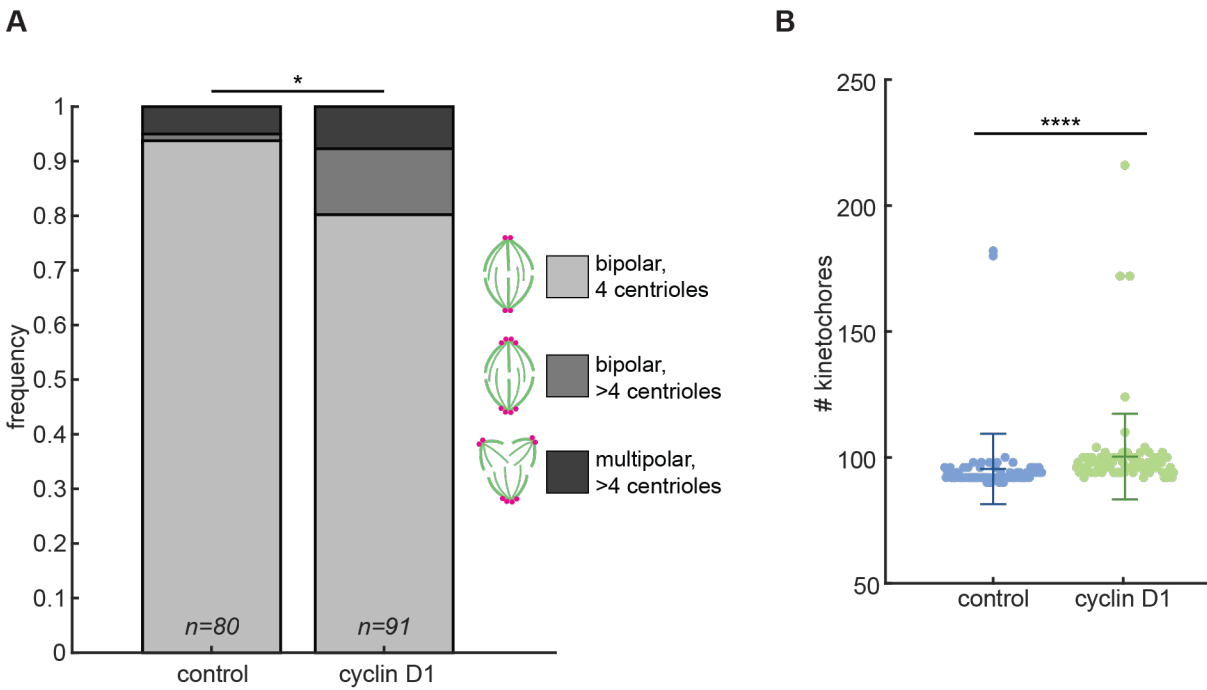


Figure 4.2. Cyclin D1 overexpression promotes aberrant spindle architectures.

A) Frequency of the three observed metaphase spindle phenotypes in each MCF10A cell lines. The distribution of phenotypes differs between cyclin D1 and control cells ($p = 0.010$, Fisher's exact test), with cyclin D1 cells enriched in cells with supernumerary centrioles.

B) Number of kinetochores per spindle. Metaphase spindles in the cyclin D1 cell line had significantly more kinetochores (representing the number of chromatids) than the control line ($p = 2.32 \times 10^{-14}$, Mann-Whitney U test). Lines indicate mean \pm standard deviation. For A and B, $n = 80$ control spindles and 91 cyclin D1 spindles, each pooled from 3 independent experiments.

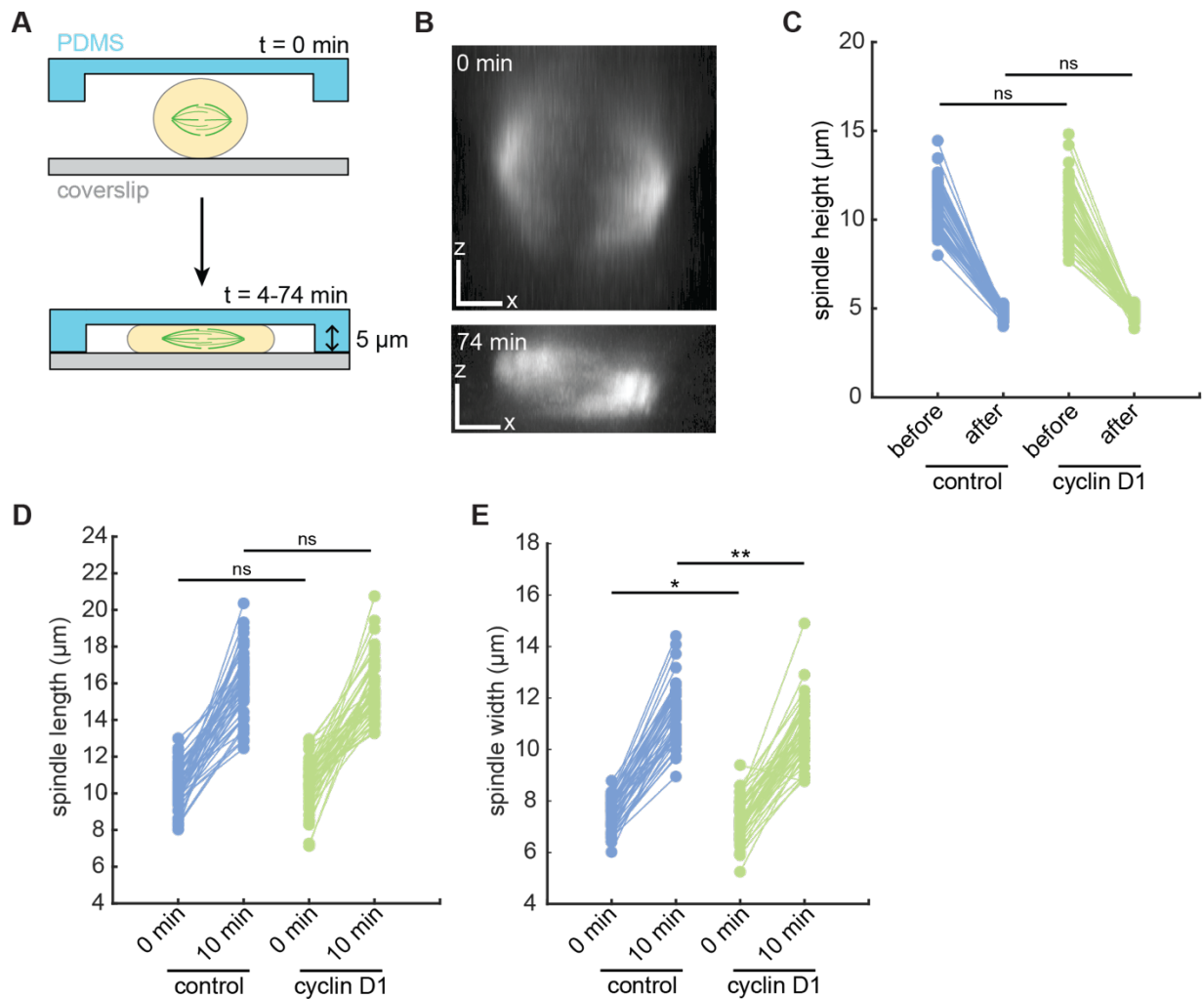


Figure 4.3. The cell compression assay is quantitatively reproducible.

A) Schematic diagram of cell compression assay using a microfluidic device. Cells were compressed to a height of 5 μm using computer-controlled negative pressure over 4 minutes, and compression was sustained for 70 additional minutes. Cells were live-imaged throughout to monitor changes in spindle architecture.

B) Side (XZ) views of a control spindle, labeled with SiR-tubulin, before and after compression. X and Z scale bars = 3 μm .

C) Between the control and cyclin D1 cell lines, spindle heights did not significantly differ before compression, and spindles were compressed to a similar final height (ns, not significant).

D) Spindle lengths before and 10 minutes after compression onset (ns, not significant).

E) Spindle widths before and 10 minutes after compression onset (* $p = 0.028$, ** $p = 0.00066$). For C-E, two-tailed two-sample t-tests were performed with $n = 57$ control and 53 cyclin D1 spindles (C) or $n = 48$ control and 52 cyclin D1 spindles (D and E). Spindles were excluded from length and width analysis if both poles were not in focus in the same z-plane.

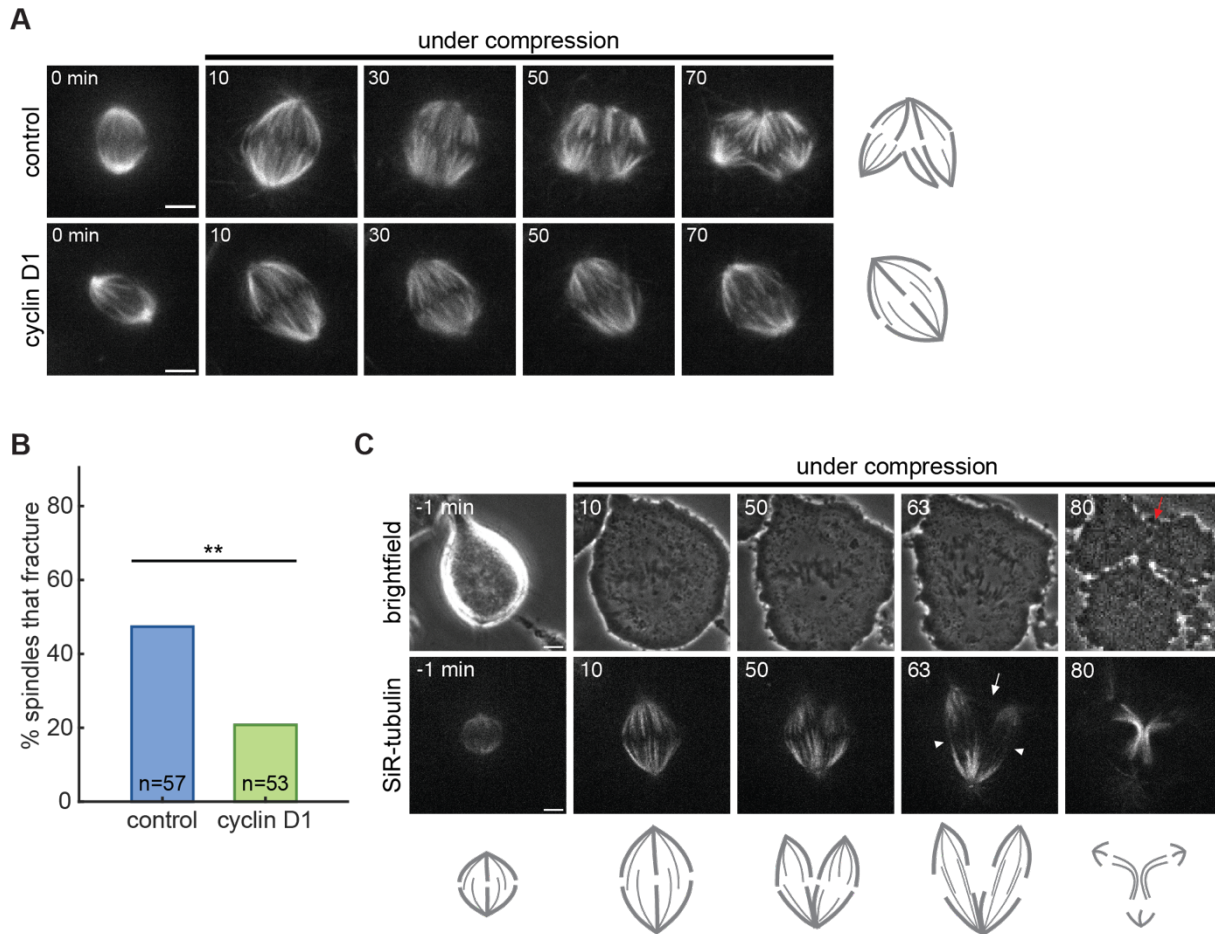


Figure 4.4. Cyclin D1 overexpression protects against spindle fracture during compression.

A) Confocal time-lapse images of control and cyclin D1-overexpressing cells undergoing compression, where the control spindle fractures between the 30:00 and 50:00 time points (cartooned at right). Tubulin is labeled with SiR-tubulin. Scale bars = 5 μ m.

B) Spindles in cyclin D1-overexpressing cells fractured less often than control spindles during the first 70 minutes of compression ($p = 0.0048$, Fisher's exact test). $n = 57$ control and 53 cyclin D1 spindles.

C) Confocal time-lapse images of a control spindle undergoing compression to a height of 4 μ m, without the addition of MG132. After the spindle fractures between the 10 and 50 minute time points, the cell enters anaphase and segregates chromosomes into 3 masses (cartooned below). Inter-polar microtubule bundles connect the original pole to each of the fractured poles (white arrowheads), while no inter-polar bundles connect the two poles resulting from the fracture (white arrow). The cytokinetic furrow is disrupted between the two fractured poles by the final 80 min timepoint (red arrow). Scale bars = 5 μ m.

Materials and methods

Cell culture

MCF10A^{Puro} and MCF10A^{Cyclin D1} cells were created in a previous study [195]. Both cell lines were cultured at 37°C and 5% CO₂, and maintained in DMEM/F12 (Invitrogen) supplemented with 5% horse serum (Gibco), 20 ng/ml epidermal growth factor, 10 µg/ml insulin, 0.5 µg/ml hydrocortisone, 100 ng/ml cholera toxin, 100 U/ml penicillin, and 100 U/ml streptomycin. For immunofluorescence experiments, cells were plated on 25 mm round #1.5 coverslips, coated with poly-L-lysine and 0.1% gelatin solution, two days prior to fixation. For compression experiments, cells were plated in 35 mm petri dishes containing 23 mm #1.5 poly-D-lysine-coated coverslips (World Precision Instruments) two days prior to imaging. Cells were plated to achieve a confluency of ~40-50% at imaging, to allow space for cells to expand under compression.

Western blotting

Cells in 6-well plates were lysed, and protein extracts were collected after centrifugation at 4°C for 30 min. Protein concentrations were measured using a Bradford assay, and equal concentrations of each sample were separated on a 4-12% Bis-Tris gel (Invitrogen) by SDS-PAGE and transferred to a nitrocellulose membrane. Membranes were blocked with 4% milk, incubated in primary antibodies overnight at 4°C, and incubated with HRP-conjugated secondary antibodies for 1 h. Proteins were detected using SuperSignal West Pico or Femto chemiluminescent substrates (Thermo Fisher). The following primary antibodies were used: mouse anti- α -tubulin DM1 α (1:5000, Sigma-Aldrich T6199) and rabbit anti-cyclin D1 SP4 (1:1000, Abcam ab16663). The following

secondary antibodies were used at a 1:10,000 dilution: goat anti-mouse IgG-HRP (Santa Cruz Biotechnology sc-2005) and mouse anti-rabbit IgG-HRP (Santa Cruz Biotechnology sc-2357).

Immunofluorescence

Cells were fixed in cold methanol for 2 minutes at -20°C. Cells were washed in TBST (0.05% Triton-X 100 in TBS) and blocked with 2% BSA in TBST. Primary and secondary antibodies were diluted in TBST + 2% BSA and incubated for one hour at room temperature (primary antibodies) or 50 minutes at room temperature (secondary antibodies). DNA was labeled with 1 µg/ml Hoechst 33342 prior to mounting on slides with ProLong Gold Antifade Mountant (Thermo Fisher P36934). The following primary antibodies were used: mouse anti- α -tubulin DM1 α conjugated to Alexa Fluor 488 (1:100, Cell Signaling Technologies 8058S), mouse anti-centrin clone 20H5 (1:200, Sigma-Aldrich 04-1624), and human anti-centromere protein CREST antibody (1:25, Antibodies Incorporated 15-234). Normal mouse IgG (1:100, Santa Cruz Biotechnology sc-2025) was used as a block before incubating in pre-conjugated mouse anti- α -tubulin DM1 α Alexa Fluor 488. The following secondary antibodies were used: goat anti-mouse conjugated to Alexa Fluor 488 and 568 (1:400, Invitrogen A11001 and A11004) and goat anti-human conjugated to Alexa Fluor 647 (1:400, Invitrogen A21445).

Cell compression

Cell compressions were performed using a 1-well dynamic cell confiner with 5 µm PDMS micropillars, or 4 µm micropillars for the example shown in Figure 4.4C (4DCell).

The device was attached to an AF1 Dual vacuum/pressure controller (Elveflow) and negative pressure was controlled using the Elveflow ESI software. Prior to imaging, a seal was established between the compression device and the dish of cells by applying a negative pressure of -10 mbar. At the start of imaging, a linear pressure ramp was applied from -10 to -150 mbar over a period of 4 minutes to lower the pillared coverslip onto the cells. Once the PDMS pillars contacted the dish, compression was maintained for 70 minutes. Z-stacks were acquired before each compression and after each timelapse acquisition to determine spindle height before and after each compression and quantitatively compare compression outcomes.

Imaging

Live imaging experiments were conducted in a stage-top humidified incubation chamber (Tokai Hit WSKM) maintained at 37°C and 5% CO₂. In compression experiments, microtubules were labeled with 100 nM SiR-tubulin (Cytoskeleton, Inc.) and 10 μM verapamil for 30-60 minutes prior to imaging. For all compression experiments shown except for the example in Figure 4.4C, the proteasome inhibitor MG132 was added to a final concentration of 10 μM 10 minutes prior to imaging to prevent anaphase entry during compressions. All live and immunofluorescence imaging was performed on an inverted spinning disk confocal (CSU-X1, Yokogawa Electric Corporation) microscope (Eclipse Ti-E, Nikon) with the following components: head dichroic Semrock Di01-T405/488/568/647; 405 nm (100 mW), 488 nm (150 mW), 561 nm (100 mW), and 642 nm (100 mW) diode lasers; ET455/50M, ET525/50M, ET600/50M, ET690/50M, and ET705/72M emission filters (Chroma Technology); and a Zyla camera (Andor

Technology). Exposures of 50-200 ms were used for fluorescence. Images were acquired with a 100× 1.45 NA Ph3 oil objective using MetaMorph 7.7.8.0 (Molecular Devices).

Data and statistical analysis

Immunofluorescence images show maximum intensity projections (Figure 4.1C) and time strip images show single spinning disk confocal Z-slices (Figure 4.4). All images were formatted for publication using FIJI [209]. The brightness/contrast for each channel was scaled identically for immunofluorescence images. The brightness/contrast for time strips were scaled individually to account for variations in tubulin labeling efficiency. Kinetochores were counted using the multi-point tool in FIJI. For compression experiments, spindle heights were measured from XZ views generated from z-stacks (see Figure 4.3B) in a vertical direction perpendicular to the coverslip. A fracture was defined as the development of a clear gap in tubulin intensity between a k-fiber minus-end and the main spindle pole within 70 minutes of compression onset (Figure 4.4). Fisher's exact test was used to compare categorical datasets (Figures 4.2A and 4.4B), a two-tailed two-sample t-test was used to compare the numerical data in Figure 4.3C based on the assumption that spindle heights are approximately normally distributed, and a Mann-Whitney U test was used to compare the numerical data in Figure 4.2B due to kinetochore number distributions that deviated from a normal distribution. Statistical tests were performed using the `ttest2`, `ranksum`, and `fishertest` functions in MATLAB R2022b, and the `fisher.test` function in R for the 2x3 comparison in Figure 4.2A. P-values are given in the figure legends.

Acknowledgements

The work described in Chapter 4 was performed under the supervision of Sophie Dumont, PhD and Andrei Goga, PhD (UCSF) in collaboration with Renaldo Sutanto, Andrea Serra Marques, PhD, and Seda Kilinic, PhD (UCSF). We thank Rachel Nakagawa and Julia Rohrberg for experimental advice, and other members of the Goga and Dumont labs for helpful discussions. Work was supported by NIH R35GM136420, NSF CAREER 1554139, NSF 1548297 Center for Cellular Construction, the Chan Zuckerberg Biohub, and the UCSF Byers Award (S.D.); the Mark Foundation and Atwater Family Foundation (A.G.); NIH 5T32CA108462 (S.K.); and an NSF Graduate Research Fellowship, Fannie and John Hertz Foundation Fellowship, and William K. Bowes, Jr. and Ute Bowes Discovery Fellowship (L.N.).

Chapter 5: Conclusions and future directions

The spindle's ability to accurately segregate chromosomes despite biochemical and mechanical noise is critical during development and tissue maintenance. Understanding how such a robust structure self-organizes from hundreds of thousands of component parts provides an excellent model for studying both disease mechanisms and the engineering design principles that biological structures employ to faithfully execute their functions. In this dissertation, I ask how opposing mitotic motors give rise to the spindle's emergent architecture, mechanics, and function, and how these properties can be rewired by oncogenic transformation.

In Chapter 2, I asked what roles the opposing motor activities of NuMA/dynein and Eg5 play, given that they are dispensable for the assembly of bipolar spindles. I investigated this question in human cells, taking advantage of inducible CRISPR knockouts to reproducibly generate doubly inhibited spindles, although this balance of contractile and extensile motor activity is highly conserved from yeast to mammalian cells [11, 99-101]. I found that NuMA- and Eg5-inhibited spindles establish bipolarity due to the partially redundant motors HSET and KIF15 and due to the passive crosslinker PRC1. However, these doubly inhibited spindles had homogenized internal microtubule organization, reduced poleward flux, and compromised structural integrity under compression, and they made more chromosome segregation errors at anaphase. Thus, the motor activities of NuMA/dynein and Eg5 are essential to the spindle's mechanical and functional robustness.

Several open questions remain about the balance between contractile and extensile activity in the spindle. A quantitative description of how microtubule nucleation is distributed in doubly inhibited spindles, and how microtubule turnover is altered, would

provide a more complete view of how the spindle is assembled and maintained. The motors inhibited in this study mediate both active stresses and crosslinking between pairs of microtubules, and decoupling these functions would provide insight into the contributions of active and passive forces to the phenotypes observed. Finally, doubly inhibited spindles were generated using complete genetic deletion or near-saturating inhibition, but exploring a full range of extensile and contractile motor activity may be fruitful in understanding the limits of robust spindle assembly.

The unexpected finding that NuMA- and Eg5-inhibited spindles were strongly twisted at anaphase led me to ask how the human spindle achieves a largely untwisted architecture despite being built by chiral force generators. While it was known that spindles in several human cell types exhibit a weak left-handed twist on average [71, 78], and while it was known that many mitotic motors have a short helical pitch as they walk around microtubule tracks in vitro [72, 74-76], it remained unclear whether torques must be balanced to allow the spindle to achieve its relatively untwisted shape. In Chapter 3, I found that the MCF10A cell line exhibited detectable left-handed twist, and characterized factors contributing to spindle twist in each direction. Twist was strongest in the final few minutes of metaphase and the first few minutes of anaphase, before sharply disappearing later in anaphase. The motors KIF4A and MKLP1, each of which contributes to outward microtubule sliding at anaphase, were redundantly required for left-handed twist in the anaphase spindle, as was the actin cytoskeleton. Depleting either dynein heavy chain or LGN had the opposite effect, suggesting that the cortical spindle positioning machinery counteracts left-handed twist at anaphase. Together these results indicate that there are

competing torques, operating from both inside the spindle and from the cell periphery, that maintain the spindle's relatively untwisted architecture.

The study of spindle twist is a new area of inquiry, and much remains to be learned about its mechanisms and functions. It is unknown why baseline spindle twist differs between cell types, even between those from the same species, and gene expression data may offer clues into the factors that set twist. While links between microtubule motors and spindle twist have been established previously [71, 78], the work described above establishes two new classes of twist regulators—the actin cytoskeleton and spindle positioning machinery—whose mechanisms remain to be discovered. For example, actin may influence spindle twist via cortical actin flows, regulation of cell shape, or other mechanisms, and it is unclear whether LGN-NuMA-dynein complexes resist left-handed twist by generating active right-handed torques or by passively resisting the torques generated by other motors. The contributions of passive crosslinkers within the anaphase spindle midzone, such as PRC1, are unknown, but are interesting candidates for future study as crosslinking likely alters the spindle's torsional rigidity. Finally, the peak in spindle twist that occurs in the minutes surrounding anaphase onset begs the question of whether twist is functionally relevant for chromosome segregation. It is possible that spindle twist that is too weak and/or too strong could be associated with an increase in segregation errors, and the molecular conditions for manipulating twist established in this dissertation provide tools to address this question in the future.

Finally, in Chapter 4, I asked how spindle architecture and mechanics are affected by oncogenic transformation. Cyclin D1 overexpression resulted in elevated rates of spindle multipolarity, aneuploidy, and supernumerary centrosomes, defects that are

observed in a wide array of tumor types. However, spindles in cyclin D1-overexpressing cells were more resistant to pole fracturing upon cell compression, protecting them from multipolar divisions that have been previously shown to lead to daughter cell death. This finding raises the prospect that cyclin D1 overexpression could be mechanically adaptive in stiff tumor environments, and may help explain its prevalence in cancer despite the aberrant spindle architectures it promotes. Looking forward, it will be valuable to determine the pathways downstream of cyclin D1 that mediate this pole-protective effect, and to test whether other oncogenes fulfill the same role. Because this study was carried out in two-dimensional cell culture, it will also be important to compare the compressive forces applied here to forces from cellular crowding experienced in a three-dimensional culture system or a tumor.

Failsafe mechanisms have been identified at many length scales that make the mammalian spindle robust to fluctuations and perturbations, an emergent property that is central to its physiological role of accurately dividing the genome. At the level of individual kinetochores, biochemical and mechanical signals are integrated to ensure that chromosomes are correctly attached [210]. At the cellular scale, redundant motors [35, 47, 48], specialized k-fiber reinforcements [7, 10], and force-sensitive feedbacks [64, 68] ensure that the spindle accommodates deformations locally while preserving global connectivity. This work describes new cellular-scale features to add to this growing list: opposing contractile and extensile motor activities promote mechanical and functional robustness, while opposing torques are required to set the spindle's global twist. At larger length scales, the role of the tissue environment in ensuring robust cell division is just beginning to be understood. A recent study found that chromosome segregation errors

are elevated in epithelial cells grown as a monolayer compared to the same cell types grown in three-dimensional culture, although the underlying mechanisms are not yet known [211].

Recently developed approaches make many questions regarding spindle robustness newly accessible. Biophysical approaches including cell compression (used in Chapters 2 & 4), microneedle manipulation in molecularly tractable mammalian cells [10, 68], and laser ablation [7, 8, 84] have been employed to test the spindle's response to mechanical challenge. New imaging modalities like lattice light sheet microscopy (used in Chapter 3) that can perform volumetric imaging with minimal phototoxicity enable us to follow events in the spindle through their entire lifetimes. Optogenetic tools, such as an optogenetically removable PRC1 [212], may enable us to investigate the roles of crosslinking in spindle robustness with improved spatiotemporal control. Finally, three-dimensional culture models provide exciting opportunities to understand how the tissue context can influence cell division. An improved understanding of the mechanical environment in which cells divide may reveal design principles of how the spindle achieves robust chromosome segregation, and lead to new therapeutic strategies for diseases in which cell division plays a prominent role.

References

1. Flemming W. Zellsubstanz, kern und zelltheilung: Vogel; 1882.
2. Neumann B, Walter T, Heriche JK, Bulkescher J, Erfle H, Conrad C, et al. Phenotypic profiling of the human genome by time-lapse microscopy reveals cell division genes. *Nature*. 2010;464(7289):721-7. doi: 10.1038/nature08869.
3. Weinberg RA. *The biology of cancer*. Second edition. ed. New York: Garland Science, Taylor & Francis Group; 2014. xx, 876, A 6, G 30, I 28 pages p.
4. Hassold T, Hunt P. To err (meiotically) is human: the genesis of human aneuploidy. *Nat Rev Genet*. 2001;2(4):280-91. doi: 10.1038/35066065.
5. Rajagopalan H, Lengauer C. Aneuploidy and cancer. *Nature*. 2004;432(7015):338-41. doi: 10.1038/nature03099.
6. Umbreit NT, Zhang CZ, Lynch LD, Blaine LJ, Cheng AM, Tourdot R, et al. Mechanisms generating cancer genome complexity from a single cell division error. *Science*. 2020;368(6488). doi: 10.1126/science.aba0712.
7. Elting MW, Hueschen CL, Udy DB, Dumont S. Force on spindle microtubule minus ends moves chromosomes. *J Cell Biol*. 2014;206(2):245-56. Epub 20140714. doi: 10.1083/jcb.201401091.
8. Sikirzhyski V, Magidson V, Steinman JB, He J, Le Berre M, Tikhonenko I, et al. Direct kinetochore-spindle pole connections are not required for chromosome segregation. *J Cell Biol*. 2014;206(2):231-43. Epub 20140714. doi: 10.1083/jcb.201401090.
9. Yu CH, Redemann S, Wu HY, Kiewisz R, Yoo TY, Conway W, et al. Central-spindle microtubules are strongly coupled to chromosomes during both anaphase A and

- anaphase B. *Mol Biol Cell*. 2019;30(19):2503-14. Epub 20190724. doi: 10.1091/mbc.E19-01-0074.
10. Suresh P, Long AF, Dumont S. Microneedle manipulation of the mammalian spindle reveals specialized, short-lived reinforcement near chromosomes. *Elife*. 2020;9. Epub 20200319. doi: 10.7554/eLife.53807.
 11. Ferenz NP, Paul R, Fagerstrom C, Mogilner A, Wadsworth P. Dynein antagonizes eg5 by crosslinking and sliding antiparallel microtubules. *Curr Biol*. 2009;19(21):1833-8. doi: 10.1016/j.cub.2009.09.025.
 12. Prosser SL, Pelletier L. Mitotic spindle assembly in animal cells: a fine balancing act. *Nat Rev Mol Cell Biol*. 2017;18(3):187-201. Epub 20170208. doi: 10.1038/nrm.2016.162.
 13. Matthies HJ, McDonald HB, Goldstein LS, Theurkauf WE. Anastral meiotic spindle morphogenesis: role of the non-claret disjunctional kinesin-like protein. *J Cell Biol*. 1996;134(2):455-64. doi: 10.1083/jcb.134.2.455.
 14. Heald R, Tournebize R, Blank T, Sandaltzopoulos R, Becker P, Hyman A, et al. Self-organization of microtubules into bipolar spindles around artificial chromosomes in *Xenopus* egg extracts. *Nature*. 1996;382(6590):420-5. doi: 10.1038/382420a0.
 15. Schuh M, Ellenberg J. Self-organization of MTOCs replaces centrosome function during acentrosomal spindle assembly in live mouse oocytes. *Cell*. 2007;130(3):484-98. doi: 10.1016/j.cell.2007.06.025.
 16. Khodjakov A, Cole RW, Oakley BR, Rieder CL. Centrosome-independent mitotic spindle formation in vertebrates. *Curr Biol*. 2000;10(2):59-67. doi: 10.1016/s0960-9822(99)00276-6.

17. Basto R, Lau J, Vinogradova T, Gardiol A, Woods CG, Khodjakov A, et al. Flies without centrioles. *Cell*. 2006;125(7):1375-86. doi: 10.1016/j.cell.2006.05.025.
18. Hornick JE, Mader CC, Tribble EK, Bagne CC, Vaughan KT, Shaw SL, et al. Amphiastral mitotic spindle assembly in vertebrate cells lacking centrosomes. *Curr Biol*. 2011;21(7):598-605. doi: 10.1016/j.cub.2011.02.049.
19. Sir JH, Putz M, Daly O, Morrison CG, Dunning M, Kilmartin JV, et al. Loss of centrioles causes chromosomal instability in vertebrate somatic cells. *J Cell Biol*. 2013;203(5):747-56. Epub 20131202. doi: 10.1083/jcb.201309038.
20. Wong YL, Anzola JV, Davis RL, Yoon M, Motamedi A, Kroll A, et al. Cell biology. Reversible centriole depletion with an inhibitor of Polo-like kinase 4. *Science*. 2015;348(6239):1155-60. Epub 20150430. doi: 10.1126/science.aaa5111.
21. Chinen T, Yamamoto S, Takeda Y, Watanabe K, Kuroki K, Hashimoto K, et al. NuMA assemblies organize microtubule asters to establish spindle bipolarity in acentrosomal human cells. *EMBO J*. 2020;39(2):e102378. Epub 20191129. doi: 10.15252/embj.2019102378.
22. Surrey T, Nedelec F, Leibler S, Karsenti E. Physical properties determining self-organization of motors and microtubules. *Science*. 2001;292(5519):1167-71. doi: 10.1126/science.1059758.
23. Verde F, Berrez JM, Antony C, Karsenti E. Taxol-induced microtubule asters in mitotic extracts of *Xenopus* eggs: requirement for phosphorylated factors and cytoplasmic dynein. *J Cell Biol*. 1991;112(6):1177-87. doi: 10.1083/jcb.112.6.1177.

24. Gaglio T, Saredi A, Compton DA. NuMA is required for the organization of microtubules into aster-like mitotic arrays. *J Cell Biol.* 1995;131(3):693-708. doi: 10.1083/jcb.131.3.693.
25. Merdes A, Heald R, Samejima K, Earnshaw WC, Cleveland DW. Formation of spindle poles by dynein/dynactin-dependent transport of NuMA. *J Cell Biol.* 2000;149(4):851-62. doi: 10.1083/jcb.149.4.851.
26. Goshima G, Nedelec F, Vale RD. Mechanisms for focusing mitotic spindle poles by minus end-directed motor proteins. *J Cell Biol.* 2005;171(2):229-40. doi: 10.1083/jcb.200505107.
27. Hueschen CL, Galstyan V, Amouzgar M, Phillips R, Dumont S. Microtubule End-Clustering Maintains a Steady-State Spindle Shape. *Curr Biol.* 2019;29(4):700-8 e5. Epub 20190207. doi: 10.1016/j.cub.2019.01.016.
28. Echeverri CJ, Paschal BM, Vaughan KT, Vallee RB. Molecular characterization of the 50-kD subunit of dynactin reveals function for the complex in chromosome alignment and spindle organization during mitosis. *J Cell Biol.* 1996;132(4):617-33. doi: 10.1083/jcb.132.4.617.
29. Hueschen CL, Kenny SJ, Xu K, Dumont S. NuMA recruits dynein activity to microtubule minus-ends at mitosis. *Elife.* 2017;6. Epub 20171129. doi: 10.7554/eLife.29328.
30. Okumura M, Natsume T, Kanemaki MT, Kiyomitsu T. Dynein-Dynactin-NuMA clusters generate cortical spindle-pulling forces as a multi-arm ensemble. *Elife.* 2018;7. Epub 20180531. doi: 10.7554/eLife.36559.

31. Renna C, Rizzelli F, Carminati M, Gaddoni C, Pirovano L, Cecatiello V, et al. Organizational Principles of the NuMA-Dynein Interaction Interface and Implications for Mitotic Spindle Functions. *Structure*. 2020;28(7):820-9 e6. Epub 20200514. doi: 10.1016/j.str.2020.04.017.
32. Harborth J, Wang J, Gueth-Hallonet C, Weber K, Osborn M. Self assembly of NuMA: multiarm oligomers as structural units of a nuclear lattice. *EMBO J*. 1999;18(6):1689-700. doi: 10.1093/emboj/18.6.1689.
33. Sun M, Jia M, Ren H, Yang B, Chi W, Xin G, et al. NuMA regulates mitotic spindle assembly, structural dynamics and function via phase separation. *Nat Commun*. 2021;12(1):7157. Epub 20211209. doi: 10.1038/s41467-021-27528-6.
34. Ma H, Qi F, Ji L, Xie S, Ran J, Liu M, et al. NuMA forms condensates through phase separation to drive spindle pole assembly. *J Mol Cell Biol*. 2022;14(1). doi: 10.1093/jmcb/mjab081.
35. Mountain V, Simerly C, Howard L, Ando A, Schatten G, Compton DA. The kinesin-related protein, HSET, opposes the activity of Eg5 and cross-links microtubules in the mammalian mitotic spindle. *J Cell Biol*. 1999;147(2):351-66. doi: 10.1083/jcb.147.2.351.
36. Cai S, Weaver LN, Ems-McClung SC, Walczak CE. Kinesin-14 family proteins HSET/XCTK2 control spindle length by cross-linking and sliding microtubules. *Mol Biol Cell*. 2009;20(5):1348-59. Epub 20081230. doi: 10.1091/mbc.E08-09-0971.
37. Lecland N, Luders J. The dynamics of microtubule minus ends in the human mitotic spindle. *Nat Cell Biol*. 2014;16(8):770-8. Epub 20140629. doi: 10.1038/ncb2996.

38. Petry S, Pugieux C, Nedelec FJ, Vale RD. Augmin promotes meiotic spindle formation and bipolarity in *Xenopus* egg extracts. *Proc Natl Acad Sci U S A*. 2011;108(35):14473-8. Epub 20110815. doi: 10.1073/pnas.1110412108.
39. Ganem NJ, Godinho SA, Pellman D. A mechanism linking extra centrosomes to chromosomal instability. *Nature*. 2009;460(7252):278-82. Epub 20090607. doi: 10.1038/nature08136.
40. Sawin KE, LeGuellec K, Philippe M, Mitchison TJ. Mitotic spindle organization by a plus-end-directed microtubule motor. *Nature*. 1992;359(6395):540-3. doi: 10.1038/359540a0.
41. Blangy A, Lane HA, d'Herin P, Harper M, Kress M, Nigg EA. Phosphorylation by p34cdc2 regulates spindle association of human Eg5, a kinesin-related motor essential for bipolar spindle formation in vivo. *Cell*. 1995;83(7):1159-69. doi: 10.1016/0092-8674(95)90142-6.
42. Kashina AS, Scholey JM, Leszyk JD, Saxton WM. An essential bipolar mitotic motor. *Nature*. 1996;384(6606):225. doi: 10.1038/384225a0.
43. Kapitein LC, Peterman EJ, Kwok BH, Kim JH, Kapoor TM, Schmidt CF. The bipolar mitotic kinesin Eg5 moves on both microtubules that it crosslinks. *Nature*. 2005;435(7038):114-8. doi: 10.1038/nature03503.
44. Raaijmakers JA, van Heesbeen RG, Meaders JL, Geers EF, Fernandez-Garcia B, Medema RH, et al. Nuclear envelope-associated dynein drives prophase centrosome separation and enables Eg5-independent bipolar spindle formation. *EMBO J*. 2012;31(21):4179-90. Epub 20121002. doi: 10.1038/emboj.2012.272.

45. Toso A, Winter JR, Garrod AJ, Amaro AC, Meraldi P, McAinsh AD. Kinetochore-generated pushing forces separate centrosomes during bipolar spindle assembly. *J Cell Biol.* 2009;184(3):365-72. doi: 10.1083/jcb.200809055.
46. Sturgill EG, Ohi R. Kinesin-12 differentially affects spindle assembly depending on its microtubule substrate. *Curr Biol.* 2013;23(14):1280-90. Epub 20130620. doi: 10.1016/j.cub.2013.05.043.
47. Tanenbaum ME, Macurek L, Janssen A, Geers EF, Alvarez-Fernandez M, Medema RH. Kif15 cooperates with eg5 to promote bipolar spindle assembly. *Curr Biol.* 2009;19(20):1703-11. Epub 20091008. doi: 10.1016/j.cub.2009.08.027.
48. Vanneste D, Takagi M, Imamoto N, Vernos I. The role of Hk1p2 in the stabilization and maintenance of spindle bipolarity. *Curr Biol.* 2009;19(20):1712-7. Epub 20091008. doi: 10.1016/j.cub.2009.09.019.
49. Drechsler H, McHugh T, Singleton MR, Carter NJ, McAinsh AD. The Kinesin-12 Kif15 is a processive track-switching tetramer. *Elife.* 2014;3:e01724. Epub 20140325. doi: 10.7554/eLife.01724.
50. Reinemann DN, Sturgill EG, Das DK, Degen MS, Voros Z, Hwang W, et al. Collective Force Regulation in Anti-parallel Microtubule Gliding by Dimeric Kif15 Kinesin Motors. *Curr Biol.* 2017;27(18):2810-20 e6. Epub 20170914. doi: 10.1016/j.cub.2017.08.018.
51. Mitchison TJ. Polewards microtubule flux in the mitotic spindle: evidence from photoactivation of fluorescence. *J Cell Biol.* 1989;109(2):637-52. doi: 10.1083/jcb.109.2.637.

52. Miyamoto DT, Perlman ZE, Burbank KS, Groen AC, Mitchison TJ. The kinesin Eg5 drives poleward microtubule flux in *Xenopus laevis* egg extract spindles. *J Cell Biol.* 2004;167(5):813-8. doi: 10.1083/jcb.200407126.
53. Cameron LA, Yang G, Cimini D, Canman JC, Kisurina-Evgenieva O, Khodjakov A, et al. Kinesin 5-independent poleward flux of kinetochore microtubules in PtK1 cells. *J Cell Biol.* 2006;173(2):173-9. doi: 10.1083/jcb.200601075.
54. Steblyanko Y, Rajendraprasad G, Osswald M, Eibes S, Jacome A, Geley S, et al. Microtubule poleward flux in human cells is driven by the coordinated action of four kinesins. *EMBO J.* 2020;39(23):e105432. Epub 20201019. doi: 10.15252/emj.2020105432.
55. Wandke C, Barisic M, Sigl R, Rauch V, Wolf F, Amaro AC, et al. Human chromokinesins promote chromosome congression and spindle microtubule dynamics during mitosis. *J Cell Biol.* 2012;198(5):847-63. doi: 10.1083/jcb.201110060.
56. Matos I, Pereira AJ, Lince-Faria M, Cameron LA, Salmon ED, Maiato H. Synchronizing chromosome segregation by flux-dependent force equalization at kinetochores. *J Cell Biol.* 2009;186(1):11-26. Epub 20090706. doi: 10.1083/jcb.200904153.
57. Maddox P, Straight A, Coughlin P, Mitchison TJ, Salmon ED. Direct observation of microtubule dynamics at kinetochores in *Xenopus* extract spindles: implications for spindle mechanics. *J Cell Biol.* 2003;162(3):377-82. doi: 10.1083/jcb.200301088.
58. Ganem NJ, Upton K, Compton DA. Efficient mitosis in human cells lacking poleward microtubule flux. *Curr Biol.* 2005;15(20):1827-32. doi: 10.1016/j.cub.2005.08.065.

59. Neahring L, Cho NH, Dumont S. Opposing motors provide mechanical and functional robustness in the human spindle. *Dev Cell*. 2021;56(21):3006-18 e5. Epub 20211005. doi: 10.1016/j.devcel.2021.09.011.
60. Nicklas RB, Koch CA. Chromosome micromanipulation. 3. Spindle fiber tension and the reorientation of mal-oriented chromosomes. *J Cell Biol*. 1969;43(1):40-50. doi: 10.1083/jcb.43.1.40.
61. Miller MP, Asbury CL, Biggins S. A TOG Protein Confers Tension Sensitivity to Kinetochore-Microtubule Attachments. *Cell*. 2016;165(6):1428-39. Epub 20160505. doi: 10.1016/j.cell.2016.04.030.
62. Chen GY, Renda F, Zhang H, Gokden A, Wu DZ, Chenoweth DM, et al. Tension promotes kinetochore-microtubule release by Aurora B kinase. *J Cell Biol*. 2021;220(6). doi: 10.1083/jcb.202007030.
63. Begg DA, Ellis GW. Micromanipulation studies of chromosome movement. I. Chromosome-spindle attachment and the mechanical properties of chromosomal spindle fibers. *J Cell Biol*. 1979;82(2):528-41. doi: 10.1083/jcb.82.2.528.
64. Dumont S, Mitchison TJ. Compression regulates mitotic spindle length by a mechanochemical switch at the poles. *Curr Biol*. 2009;19(13):1086-95. Epub 2009/06/23. doi: 10.1016/j.cub.2009.05.056.
65. Itabashi T, Takagi J, Shimamoto Y, Onoe H, Kuwana K, Shimoyama I, et al. Probing the mechanical architecture of the vertebrate meiotic spindle. *Nat Methods*. 2009;6(2):167-72. Epub 20090118. doi: 10.1038/nmeth.1297.

66. Shimamoto Y, Maeda YT, Ishiwata S, Libchaber AJ, Kapoor TM. Insights into the micromechanical properties of the metaphase spindle. *Cell*. 2011;145(7):1062-74. doi: 10.1016/j.cell.2011.05.038.
67. Takagi J, Sakamoto R, Shiratsuchi G, Maeda YT, Shimamoto Y. Mechanically Distinct Microtubule Arrays Determine the Length and Force Response of the Meiotic Spindle. *Dev Cell*. 2019;49(2):267-78 e5. Epub 20190411. doi: 10.1016/j.devcel.2019.03.014.
68. Long AF, Suresh P, Dumont S. Individual kinetochore-fibers locally dissipate force to maintain robust mammalian spindle structure. *J Cell Biol*. 2020;219(8). doi: 10.1083/jcb.201911090.
69. Brugues J, Needleman D. Physical basis of spindle self-organization. *Proc Natl Acad Sci U S A*. 2014;111(52):18496-500. Epub 20141202. doi: 10.1073/pnas.1409404111.
70. Roostalu J, Rickman J, Thomas C, Nedelec F, Surrey T. Determinants of Polar versus Nematic Organization in Networks of Dynamic Microtubules and Mitotic Motors. *Cell*. 2018;175(3):796-808 e14. doi: 10.1016/j.cell.2018.09.029.
71. Novak M, Polak B, Simunic J, Boban Z, Kuzmic B, Thomae AW, et al. The mitotic spindle is chiral due to torques within microtubule bundles. *Nat Commun*. 2018;9(1):3571. Epub 20180903. doi: 10.1038/s41467-018-06005-7.
72. Yajima J, Mizutani K, Nishizaka T. A torque component present in mitotic kinesin Eg5 revealed by three-dimensional tracking. *Nat Struct Mol Biol*. 2008;15(10):1119-21. Epub 20080921. doi: 10.1038/nsmb.1491.

73. Maruyama Y, Sugawa M, Yamaguchi S, Davies T, Osaki T, Kobayashi T, et al. CYK4 relaxes the bias in the off-axis motion by MKLP1 kinesin-6. *Commun Biol.* 2021;4(1):180. Epub 20210210. doi: 10.1038/s42003-021-01704-2.
74. Bormuth V, Nitzsche B, Ruhnnow F, Mitra A, Storch M, Rammner B, et al. The highly processive kinesin-8, Kip3, switches microtubule protofilaments with a bias toward the left. *Biophys J.* 2012;103(1):L4-6. doi: 10.1016/j.bpj.2012.05.024.
75. Elshenawy MM, Canty JT, Oster L, Ferro LS, Zhou Z, Blanchard SC, et al. Cargo adaptors regulate stepping and force generation of mammalian dynein-dynactin. *Nat Chem Biol.* 2019;15(11):1093-101. Epub 20190909. doi: 10.1038/s41589-019-0352-0.
76. Mitra A, Meissner L, Gandhimathi R, Renger R, Ruhnnow F, Diez S. Kinesin-14 motors drive a right-handed helical motion of antiparallel microtubules around each other. *Nat Commun.* 2020;11(1):2565. Epub 20200522. doi: 10.1038/s41467-020-16328-z.
77. Nitzsche B, Dudek E, Hajdo L, Kasprzak AA, Vilfan A, Diez S. Working stroke of the kinesin-14, ncd, comprises two substeps of different direction. *Proc Natl Acad Sci U S A.* 2016;113(43):E6582-E9. Epub 20161011. doi: 10.1073/pnas.1525313113.
78. Trupinic M, Kokanovic B, Ponjavic I, Barisic I, Segvic S, Ivec A, et al. The chirality of the mitotic spindle provides a mechanical response to forces and depends on microtubule motors and augmin. *Curr Biol.* 2022. Epub 20220504. doi: 10.1016/j.cub.2022.04.035.
79. Velle KB, Kennard AS, Trupinic M, Ivec A, Swafford AJM, Nolton E, et al. Naegleria's mitotic spindles are built from unique tubulins and highlight core spindle features.

- Curr Biol. 2022;32(6):1247-61 e6. Epub 20220208. doi: 10.1016/j.cub.2022.01.034.
80. van Heesbeen RG, Tanenbaum ME, Medema RH. Balanced activity of three mitotic motors is required for bipolar spindle assembly and chromosome segregation. *Cell Rep.* 2014;8(4):948-56. Epub 20140807. doi: 10.1016/j.celrep.2014.07.015.
81. Sturgill EG, Norris SR, Guo Y, Ohi R. Kinesin-5 inhibitor resistance is driven by kinesin-12. *J Cell Biol.* 2016;213(2):213-27. Epub 20160418. doi: 10.1083/jcb.201507036.
82. Maiato H, Rieder CL, Khodjakov A. Kinetochore-driven formation of kinetochore fibers contributes to spindle assembly during animal mitosis. *J Cell Biol.* 2004;167(5):831-40. Epub 20041129. doi: 10.1083/jcb.200407090.
83. Kajtez J, Solomatina A, Novak M, Polak B, Vukusic K, Rudiger J, et al. Overlap microtubules link sister k-fibres and balance the forces on bi-oriented kinetochores. *Nat Commun.* 2016;7:10298. Epub 20160105. doi: 10.1038/ncomms10298.
84. Elting MW, Prakash M, Udy DB, Dumont S. Mapping Load-Bearing in the Mammalian Spindle Reveals Local Kinetochore Fiber Anchorage that Provides Mechanical Isolation and Redundancy. *Curr Biol.* 2017;27(14):2112-22 e5. Epub 20170706. doi: 10.1016/j.cub.2017.06.018.
85. Franck AD, Powers AF, Gestaut DR, Gonen T, Davis TN, Asbury CL. Tension applied through the Dam1 complex promotes microtubule elongation providing a direct mechanism for length control in mitosis. *Nat Cell Biol.* 2007;9(7):832-7. Epub 20070617. doi: 10.1038/ncb1609.

86. Akiyoshi B, Sarangapani KK, Powers AF, Nelson CR, Reichow SL, Arellano-Santoyo H, et al. Tension directly stabilizes reconstituted kinetochore-microtubule attachments. *Nature*. 2010;468(7323):576-9. doi: 10.1038/nature09594.
87. Skibbens RV, Salmon ED. Micromanipulation of chromosomes in mitotic vertebrate tissue cells: tension controls the state of kinetochore movement. *Exp Cell Res*. 1997;235(2):314-24. doi: 10.1006/excr.1997.3691.
88. Nicklas RB, Staehly CA. Chromosome micromanipulation. I. The mechanics of chromosome attachment to the spindle. *Chromosoma*. 1967;21(1):1-16. doi: 10.1007/BF00330544.
89. McIntosh JR, Molodtsov MI, Ataullakhanov FI. Biophysics of mitosis. *Q Rev Biophys*. 2012;45(2):147-207. Epub 2012/02/11. doi: 10.1017/S0033583512000017.
90. Elting MW, Suresh P, Dumont S. The Spindle: Integrating Architecture and Mechanics across Scales. *Trends Cell Biol*. 2018;28(11):896-910. Epub 2018/08/11. doi: 10.1016/j.tcb.2018.07.003.
91. Hueschen CL, Kenny SJ, Xu K, Dumont S. NuMA recruits dynein activity to microtubule minus-ends at mitosis. *eLife*. 2017;6:e29328. Epub 2017/12/01. doi: 10.7554/eLife.29328.
92. Foster PJ, Furthauer S, Shelley MJ, Needleman DJ. Active contraction of microtubule networks. *eLife*. 2015;4:e10837. Epub 2015/12/25. doi: 10.7554/eLife.10837.
93. Gaglio T, Saredi A, Bingham JB, Hasbani MJ, Gill SR, Schroer TA, et al. Opposing motor activities are required for the organization of the mammalian mitotic spindle pole. *J Cell Biol*. 1996;135(2):399-414. Epub 1996/10/01. doi: 10.1083/jcb.135.2.399.

94. Shimamoto Y, Forth S, Kapoor TM. Measuring Pushing and Braking Forces Generated by Ensembles of Kinesin-5 Crosslinking Two Microtubules. *Dev Cell*. 2015;34(6):669-81. Epub 2015/09/30. doi: 10.1016/j.devcel.2015.08.017.
95. Tan R, Foster PJ, Needleman DJ, McKenney RJ. Cooperative Accumulation of Dynein-Dynactin at Microtubule Minus-Ends Drives Microtubule Network Reorganization. *Dev Cell*. 2018;44(2):233-47 e4. doi: 10.1016/j.devcel.2017.12.023.
96. Mayer TU, Kapoor TM, Haggarty SJ, King RW, Schreiber SL, Mitchison TJ. Small molecule inhibitor of mitotic spindle bipolarity identified in a phenotype-based screen. *Science*. 1999;286(5441):971-4. Epub 1999/11/05. doi: 10.1126/science.286.5441.971.
97. Tanenbaum ME, Macurek L, Galjart N, Medema RH. Dynein, Lis1 and CLIP-170 counteract Eg5-dependent centrosome separation during bipolar spindle assembly. *EMBO J*. 2008;27(24):3235-45. Epub 20081120. doi: 10.1038/emboj.2008.242.
98. Florian S, Mayer TU. The functional antagonism between Eg5 and dynein in spindle bipolarization is not compatible with a simple push-pull model. *Cell Rep*. 2012;1(5):408-16. Epub 2012/07/27. doi: 10.1016/j.celrep.2012.03.006.
99. Saunders WS, Hoyt MA. Kinesin-related proteins required for structural integrity of the mitotic spindle. *Cell*. 1992;70(3):451-8. Epub 1992/08/07. doi: 10.1016/0092-8674(92)90169-d.

100. Sharp DJ, Yu KR, Sisson JC, Sullivan W, Scholey JM. Antagonistic microtubule-sliding motors position mitotic centrosomes in *Drosophila* early embryos. *Nat Cell Biol.* 1999;1(1):51-4. Epub 1999/11/13. doi: 10.1038/9025.
101. Mitchison TJ, Maddox P, Gaetz J, Groen A, Shirasu M, Desai A, et al. Roles of polymerization dynamics, opposed motors, and a tensile element in governing the length of *Xenopus* extract meiotic spindles. *Mol Biol Cell.* 2005;16(6):3064-76. Epub 20050323. doi: 10.1091/mbc.e05-02-0174.
102. Rincon SA, Lamson A, Blackwell R, Syrovatkina V, Fraiser V, Paoletti A, et al. Kinesin-5-independent mitotic spindle assembly requires the antiparallel microtubule crosslinker Ase1 in fission yeast. *Nat Commun.* 2017;8:15286. Epub 2017/05/18. doi: 10.1038/ncomms15286.
103. Bruges J, Nuzzo V, Mazur E, Needleman DJ. Nucleation and transport organize microtubules in metaphase spindles. *Cell.* 2012;149(3):554-64. doi: 10.1016/j.cell.2012.03.027.
104. Raaijmakers JA, Medema RH. Function and regulation of dynein in mitotic chromosome segregation. *Chromosoma.* 2014;123(5):407-22. Epub 2014/05/30. doi: 10.1007/s00412-014-0468-7.
105. Howell BJ, McEwen BF, Canman JC, Hoffman DB, Farrar EM, Rieder CL, et al. Cytoplasmic dynein/dynactin drives kinetochore protein transport to the spindle poles and has a role in mitotic spindle checkpoint inactivation. *J Cell Biol.* 2001;155(7):1159-72. Epub 2002/01/05. doi: 10.1083/jcb.200105093.
106. McKinley KL, Cheeseman IM. Large-Scale Analysis of CRISPR/Cas9 Cell-Cycle Knockouts Reveals the Diversity of p53-Dependent Responses to Cell-Cycle

- Defects. *Dev Cell*. 2017;40(4):405-20 e2. Epub 20170216. doi: 10.1016/j.devcel.2017.01.012.
107. Sanchez T, Chen DT, DeCamp SJ, Heymann M, Dogic Z. Spontaneous motion in hierarchically assembled active matter. *Nature*. 2012;491(7424):431-4. Epub 2012/11/09. doi: 10.1038/nature11591.
108. Gassmann R, Holland AJ, Varma D, Wan X, Civril F, Cleveland DW, et al. Removal of Spindly from microtubule-attached kinetochores controls spindle checkpoint silencing in human cells. *Genes Dev*. 2010;24(9):957-71. Epub 2010/05/05. doi: 10.1101/gad.1886810.
109. Polak B, Risteski P, Lesjak S, Tolic IM. PRC1-labeled microtubule bundles and kinetochore pairs show one-to-one association in metaphase. *EMBO Rep*. 2017;18(2):217-30. Epub 20161227. doi: 10.15252/embr.201642650.
110. DeLuca JG, Moree B, Hickey JM, Kilmartin JV, Salmon ED. hNuf2 inhibition blocks stable kinetochore-microtubule attachment and induces mitotic cell death in HeLa cells. *J Cell Biol*. 2002;159(4):549-55. Epub 2002/11/20. doi: 10.1083/jcb.200208159.
111. Kwon M, Godinho SA, Chandhok NS, Ganem NJ, Azioune A, Thery M, et al. Mechanisms to suppress multipolar divisions in cancer cells with extra centrosomes. *Genes Dev*. 2008;22(16):2189-203. Epub 2008/07/30. doi: 10.1101/gad.1700908.
112. Crowder ME, Strzelecka M, Wilbur JD, Good MC, von Dassow G, Heald R. A comparative analysis of spindle morphometrics across metazoans. *Curr Biol*. 2015;25(11):1542-50. Epub 20150521. doi: 10.1016/j.cub.2015.04.036.

113. Steblyanko Y, Rajendraprasad G, Osswald M, Eibes S, Jacome A, Geley S, et al. Microtubule poleward flux in human cells is driven by the coordinated action of four kinesins. *EMBO J.* 2020;39:e105432. Epub 2020/10/20. doi: 10.15252/emj.2020105432.
114. Le Berre M, Aubertin J, Piel M. Fine control of nuclear confinement identifies a threshold deformation leading to lamina rupture and induction of specific genes. *Integr Biol (Camb).* 2012;4(11):1406-14. Epub 2012/10/06. doi: 10.1039/c2ib20056b.
115. Guild J, Ginzberg MB, Hueschen CL, Mitchison TJ, Dumont S. Increased lateral microtubule contact at the cell cortex is sufficient to drive mammalian spindle elongation. *Mol Biol Cell.* 2017;28(14):1975-83. Epub 20170503. doi: 10.1091/mbc.E17-03-0171.
116. Lancaster OM, Le Berre M, Dimitracopoulos A, Bonazzi D, Zlotek-Zlotkiewicz E, Picone R, et al. Mitotic rounding alters cell geometry to ensure efficient bipolar spindle formation. *Dev Cell.* 2013;25(3):270-83. Epub 20130425. doi: 10.1016/j.devcel.2013.03.014.
117. Aist JR, Liang H, Berns MW. Astral and spindle forces in PtK2 cells during anaphase B: a laser microbeam study. *J Cell Sci.* 1993;104 (Pt 4):1207-16. Epub 1993/04/01.
118. Grill SW, Gonczy P, Stelzer EH, Hyman AA. Polarity controls forces governing asymmetric spindle positioning in the *Caenorhabditis elegans* embryo. *Nature.* 2001;409(6820):630-3. doi: 10.1038/35054572.
119. Vukusic K, Ponjavic I, Buda R, Risteski P, Tolic IM. Microtubule-sliding modules based on kinesins EG5 and PRC1-dependent KIF4A drive human spindle

- elongation. *Dev Cell*. 2021;56(9):1253-67 e10. Epub 2021/04/29. doi: 10.1016/j.devcel.2021.04.005.
120. Norris SR, Jung S, Singh P, Strothman CE, Erwin AL, Ohi MD, et al. Microtubule minus-end aster organization is driven by processive HSET-tubulin clusters. *Nat Commun*. 2018;9(1):2659. Epub 20180709. doi: 10.1038/s41467-018-04991-2.
121. Ma N, Tulu US, Ferenz NP, Fagerstrom C, Wilde A, Wadsworth P. Poleward transport of TPX2 in the mammalian mitotic spindle requires dynein, Eg5, and microtubule flux. *Mol Biol Cell*. 2010;21(6):979-88. Epub 20100128. doi: 10.1091/mbc.E09-07-0601.
122. Suresh P, Long AF, Dumont S. Microneedle manipulation of the mammalian spindle reveals specialized, short-lived reinforcement near chromosomes. *eLife*. 2020;9:e53807. Epub 2020/03/20. doi: 10.7554/eLife.53807.
123. Gatlin JC, Matov A, Danuser G, Mitchison TJ, Salmon ED. Directly probing the mechanical properties of the spindle and its matrix. *J Cell Biol*. 2010;188(4):481-9. Epub 2010/02/24. doi: 10.1083/jcb.200907110.
124. Vukusic K, Buda R, Bosilj A, Milas A, Pavin N, Tolic IM. Microtubule Sliding within the Bridging Fiber Pushes Kinetochore Fibers Apart to Segregate Chromosomes. *Dev Cell*. 2017;43(1):11-23 e6. doi: 10.1016/j.devcel.2017.09.010.
125. Can S, Dewitt MA, Yildiz A. Bidirectional helical motility of cytoplasmic dynein around microtubules. *Elife*. 2014;3:e03205. Epub 20140728. doi: 10.7554/eLife.03205.
126. Mitra A, Ruhnnow F, Girardo S, Diez S. Directionally biased sidestepping of Kip3/kinesin-8 is regulated by ATP waiting time and motor-microtubule interaction

- strength. *Proc Natl Acad Sci U S A*. 2018;115(34):E7950-E9. Epub 2018/08/11. doi: 10.1073/pnas.1801820115.
127. Trupinic M, Ponjavic I, Kokanovic B, Barisic I, Segvic S, Ivec A, et al. Twist of the mitotic spindle culminates at anaphase onset and depends on microtubule-associated proteins along with external forces. *bioRxiv*. 2020. doi: 10.1101/2020.12.27.424486.
128. Rodenfels J, Neugebauer KM, Howard J. Heat Oscillations Driven by the Embryonic Cell Cycle Reveal the Energetic Costs of Signaling. *Dev Cell*. 2019;48(5):646-58 e6. Epub 2019/02/05. doi: 10.1016/j.devcel.2018.12.024.
129. Cao Y, Wang H, Ouyang Q, Tu Y. The free energy cost of accurate biochemical oscillations. *Nat Phys*. 2015;11(9):772-8. Epub 2015/11/14. doi: 10.1038/nphys3412.
130. Forth S, Hsia KC, Shimamoto Y, Kapoor TM. Asymmetric friction of nonmotor MAPs can lead to their directional motion in active microtubule networks. *Cell*. 2014;157(2):420-32. Epub 2014/04/15. doi: 10.1016/j.cell.2014.02.018.
131. DeLuca JG, Howell BJ, Canman JC, Hickey JM, Fang G, Salmon ED. Nuf2 and Hec1 are required for retention of the checkpoint proteins Mad1 and Mad2 to kinetochores. *Curr Biol*. 2003;13(23):2103-9. doi: 10.1016/j.cub.2003.10.056.
132. Pamula MC, Carlini L, Forth S, Verma P, Suresh S, Legant WR, et al. High-resolution imaging reveals how the spindle midzone impacts chromosome movement. *J Cell Biol*. 2019;218(8):2529-44. Epub 20190627. doi: 10.1083/jcb.201904169.
133. Liu D, Ding X, Du J, Cai X, Huang Y, Ward T, et al. Human NUF2 interacts with centromere-associated protein E and is essential for a stable spindle microtubule-

- kinetochore attachment. *J Biol Chem.* 2007;282(29):21415-24. Epub 2007/05/31. doi: 10.1074/jbc.M609026200.
134. Thévenaz P, Ruttimann UE, Unser M. A pyramid approach to subpixel registration based on intensity. *IEEE Trans Image Process.* 1998;7(1):27-41. Epub 2008/02/13. doi: 10.1109/83.650848.
135. Meijering E, Dzyubachyk O, Smal I. Methods for cell and particle tracking. *Methods Enzymol.* 2012;504:183-200. Epub 2012/01/24. doi: 10.1016/B978-0-12-391857-4.00009-4.
136. Cross RA, McAinsh A. Prime movers: the mechanochemistry of mitotic kinesins. *Nat Rev Mol Cell Biol.* 2014;15(4):257-71. doi: 10.1038/nrm3768.
137. Canty JT, Tan R, Kusakci E, Fernandes J, Yildiz A. Structure and Mechanics of Dynein Motors. *Annu Rev Biophys.* 2021;50:549-74. doi: 10.1146/annurev-biophys-111020-101511.
138. Soule HD, Maloney TM, Wolman SR, Peterson WD, Jr., Brenz R, McGrath CM, et al. Isolation and characterization of a spontaneously immortalized human breast epithelial cell line, MCF-10. *Cancer Res.* 1990;50(18):6075-86.
139. Lechler T, Mapelli M. Spindle positioning and its impact on vertebrate tissue architecture and cell fate. *Nat Rev Mol Cell Biol.* 2021;22(10):691-708. Epub 20210622. doi: 10.1038/s41580-021-00384-4.
140. Du Q, Macara IG. Mammalian Pins is a conformational switch that links NuMA to heterotrimeric G proteins. *Cell.* 2004;119(4):503-16. doi: 10.1016/j.cell.2004.10.028.

141. Kiyomitsu T, Cheeseman IM. Cortical dynein and asymmetric membrane elongation coordinately position the spindle in anaphase. *Cell*. 2013;154(2):391-402. doi: 10.1016/j.cell.2013.06.010.
142. Seldin L, Poulson ND, Foote HP, Lechler T. NuMA localization, stability, and function in spindle orientation involve 4.1 and Cdk1 interactions. *Mol Biol Cell*. 2013;24(23):3651-62. Epub 20131009. doi: 10.1091/mbc.E13-05-0277.
143. Kotak S, Busso C, Gonczy P. NuMA interacts with phosphoinositides and links the mitotic spindle with the plasma membrane. *EMBO J*. 2014;33(16):1815-30. Epub 20140704. doi: 10.15252/emj.201488147.
144. Naganathan SR, Furthauer S, Nishikawa M, Julicher F, Grill SW. Active torque generation by the actomyosin cell cortex drives left-right symmetry breaking. *Elife*. 2014;3:e04165. Epub 20141217. doi: 10.7554/eLife.04165.
145. Shibazaki Y, Shimizu M, Kuroda R. Body handedness is directed by genetically determined cytoskeletal dynamics in the early embryo. *Curr Biol*. 2004;14(16):1462-7. doi: 10.1016/j.cub.2004.08.018.
146. Davison A, McDowell GS, Holden JM, Johnson HF, Koutsovoulos GD, Liu MM, et al. Formin Is Associated with Left-Right Asymmetry in the Pond Snail and the Frog. *Curr Biol*. 2016;26(5):654-60. Epub 20160225. doi: 10.1016/j.cub.2015.12.071.
147. Kuroda R, Fujikura K, Abe M, Hosoiri Y, Asakawa S, Shimizu M, et al. Diaphanous gene mutation affects spiral cleavage and chirality in snails. *Sci Rep*. 2016;6:34809. Epub 20161006. doi: 10.1038/srep34809.

148. Tee YH, Shemesh T, Thiagarajan V, Hariadi RF, Anderson KL, Page C, et al. Cellular chirality arising from the self-organization of the actin cytoskeleton. *Nat Cell Biol.* 2015;17(4):445-57. Epub 20150323. doi: 10.1038/ncb3137.
149. Farina F, Ramkumar N, Brown L, Samandar Eweis D, Anstatt J, Waring T, et al. Local actin nucleation tunes centrosomal microtubule nucleation during passage through mitosis. *EMBO J.* 2019;38(11). Epub 20190423. doi: 10.15252/emboj.201899843.
150. Zhu C, Jiang W. Cell cycle-dependent translocation of PRC1 on the spindle by Kif4 is essential for midzone formation and cytokinesis. *Proc Natl Acad Sci U S A.* 2005;102(2):343-8. Epub 20041229. doi: 10.1073/pnas.0408438102.
151. Bieling P, Telley IA, Surrey T. A minimal midzone protein module controls formation and length of antiparallel microtubule overlaps. *Cell.* 2010;142(3):420-32. doi: 10.1016/j.cell.2010.06.033.
152. Wijeratne S, Subramanian R. Geometry of antiparallel microtubule bundles regulates relative sliding and stalling by PRC1 and Kif4A. *Elife.* 2018;7. Epub 20181024. doi: 10.7554/eLife.32595.
153. Collins ES, Balchand SK, Faraci JL, Wadsworth P, Lee WL. Cell cycle-regulated cortical dynein/dynactin promotes symmetric cell division by differential pole motion in anaphase. *Mol Biol Cell.* 2012;23(17):3380-90. Epub 20120718. doi: 10.1091/mbc.E12-02-0109.
154. Kotak S, Busso C, Gonczy P. NuMA phosphorylation by CDK1 couples mitotic progression with cortical dynein function. *EMBO J.* 2013;32(18):2517-29. Epub 20130806. doi: 10.1038/emboj.2013.172.

155. Depue RH, Jr., Rice RV. F-Actin Is a Right-Handed Helix. *J Mol Biol.* 1965;12:302-3. doi: 10.1016/s0022-2836(65)80306-0.
156. Lebreton G, Geminard C, Lapraz F, Pырpassopoulos S, Cerezo D, Speder P, et al. Molecular to organismal chirality is induced by the conserved myosin 1D. *Science.* 2018;362(6417):949-52. doi: 10.1126/science.aat8642.
157. Ali MY, Uemura S, Adachi K, Itoh H, Kinoshita K, Jr., Ishiwata S. Myosin V is a left-handed spiral motor on the right-handed actin helix. *Nat Struct Biol.* 2002;9(6):464-7. doi: 10.1038/nsb803.
158. Mizuno H, Higashida C, Yuan Y, Ishizaki T, Narumiya S, Watanabe N. Rotational movement of the formin mDia1 along the double helical strand of an actin filament. *Science.* 2011;331(6013):80-3. Epub 20101209. doi: 10.1126/science.1197692.
159. Naganathan SR, Middelkoop TC, Furthauer S, Grill SW. Actomyosin-driven left-right asymmetry: from molecular torques to chiral self organization. *Curr Opin Cell Biol.* 2016;38:24-30. Epub 20160130. doi: 10.1016/j.ceb.2016.01.004.
160. Xu J, Van Keymeulen A, Wakida NM, Carlton P, Berns MW, Bourne HR. Polarity reveals intrinsic cell chirality. *Proc Natl Acad Sci U S A.* 2007;104(22):9296-300. Epub 20070517. doi: 10.1073/pnas.0703153104.
161. Levy JR, Holzbaur EL. Dynein drives nuclear rotation during forward progression of motile fibroblasts. *J Cell Sci.* 2008;121(Pt 19):3187-95. Epub 20080909. doi: 10.1242/jcs.033878.
162. Draviam VM, Shapiro I, Aldridge B, Sorger PK. Misorientation and reduced stretching of aligned sister kinetochores promote chromosome missegregation in EB1- or

- APC-depleted cells. *EMBO J.* 2006;25(12):2814-27. Epub 20060608. doi: 10.1038/sj.emboj.7601168.
163. Goehring A, Lee CH, Wang KH, Michel JC, Claxton DP, Bacongus I, et al. Screening and large-scale expression of membrane proteins in mammalian cells for structural studies. *Nat Protoc.* 2014;9(11):2574-85. Epub 20141009. doi: 10.1038/nprot.2014.173.
164. Liu TL, Upadhyayula S, Milkie DE, Singh V, Wang K, Swinburne IA, et al. Observing the cell in its native state: Imaging subcellular dynamics in multicellular organisms. *Science.* 2018;360(6386). doi: 10.1126/science.aaq1392.
165. Liu G, Ruan X, Milkie DE, Gorlitz F, Mueller M, Hercule W, et al. Characterization, comparison, and optimization of lattice light sheets. *Sci Adv.* 2023;9(13):eade6623. Epub 20230331. doi: 10.1126/sciadv.ade6623.
166. Farneböck G, editor *Two-Frame Motion Estimation Based on Polynomial Expansion* 2003; Berlin, Heidelberg: Springer Berlin Heidelberg.
167. Holland AJ, Cleveland DW. Boveri revisited: chromosomal instability, aneuploidy and tumorigenesis. *Nat Rev Mol Cell Biol.* 2009;10(7):478-87. doi: 10.1038/nrm2718.
168. Lingle WL, Lutz WH, Ingle JN, Maihle NJ, Salisbury JL. Centrosome hypertrophy in human breast tumors: implications for genomic stability and cell polarity. *Proc Natl Acad Sci U S A.* 1998;95(6):2950-5. doi: 10.1073/pnas.95.6.2950.
169. Pihan GA, Purohit A, Wallace J, Knecht H, Woda B, Quesenberry P, et al. Centrosome defects and genetic instability in malignant tumors. *Cancer Res.* 1998;58(17):3974-85.

170. Chan JY. A clinical overview of centrosome amplification in human cancers. *Int J Biol Sci.* 2011;7(8):1122-44. Epub 20111016. doi: 10.7150/ijbs.7.1122.
171. Lengauer C, Kinzler KW, Vogelstein B. Genetic instability in colorectal cancers. *Nature.* 1997;386(6625):623-7. doi: 10.1038/386623a0.
172. Drews RM, Hernando B, Tarabichi M, Haase K, Lesluyes T, Smith PS, et al. A pan-cancer compendium of chromosomal instability. *Nature.* 2022;606(7916):976-83. Epub 20220615. doi: 10.1038/s41586-022-04789-9.
173. Rohrberg J, Van de Mark D, Amouzgar M, Lee JV, Taileb M, Corella A, et al. MYC Dysregulates Mitosis, Revealing Cancer Vulnerabilities. *Cell Rep.* 2020;30(10):3368-82 e7. doi: 10.1016/j.celrep.2020.02.041.
174. Silkworth WT, Nardi IK, Scholl LM, Cimini D. Multipolar spindle pole coalescence is a major source of kinetochore mis-attachment and chromosome mis-segregation in cancer cells. *PLoS One.* 2009;4(8):e6564. Epub 20090810. doi: 10.1371/journal.pone.0006564.
175. Kumar S, Weaver VM. Mechanics, malignancy, and metastasis: the force journey of a tumor cell. *Cancer Metastasis Rev.* 2009;28(1-2):113-27. doi: 10.1007/s10555-008-9173-4.
176. Plodinec M, Loparic M, Monnier CA, Obermann EC, Zanetti-Dallenbach R, Oertle P, et al. The nanomechanical signature of breast cancer. *Nat Nanotechnol.* 2012;7(11):757-65. Epub 20121021. doi: 10.1038/nnano.2012.167.
177. Nia HT, Liu H, Seano G, Datta M, Jones D, Rahbari N, et al. Solid stress and elastic energy as measures of tumour mechanopathology. *Nat Biomed Eng.* 2016;1. Epub 20161128. doi: 10.1038/s41551-016-0004.

178. Tse HT, Weaver WM, Di Carlo D. Increased asymmetric and multi-daughter cell division in mechanically confined microenvironments. *PLoS One*. 2012;7(6):e38986. Epub 20120625. doi: 10.1371/journal.pone.0038986.
179. Matthews HK, Ganguli S, Plak K, Taubenberger AV, Win Z, Williamson M, et al. Oncogenic Signaling Alters Cell Shape and Mechanics to Facilitate Cell Division under Confinement. *Dev Cell*. 2020;52(5):563-73 e3. Epub 20200206. doi: 10.1016/j.devcel.2020.01.004.
180. Cheng L, Li J, Sun H, Jiang H. Appropriate mechanical confinement inhibits multipolar cell division via pole-cortex interaction. *Physical Review X*. 2023;13(1). doi: 10.1103/PhysRevX.13.011036.
181. Heldin CH, Rubin K, Pietras K, Ostman A. High interstitial fluid pressure - an obstacle in cancer therapy. *Nat Rev Cancer*. 2004;4(10):806-13. doi: 10.1038/nrc1456.
182. Levental KR, Yu H, Kass L, Lakins JN, Egeblad M, Ertler JT, et al. Matrix crosslinking forces tumor progression by enhancing integrin signaling. *Cell*. 2009;139(5):891-906. doi: 10.1016/j.cell.2009.10.027.
183. Nader GPF, Aguera-Gonzalez S, Routet F, Gratia M, Maurin M, Cancila V, et al. Compromised nuclear envelope integrity drives TREX1-dependent DNA damage and tumor cell invasion. *Cell*. 2021;184(20):5230-46 e22. Epub 20210921. doi: 10.1016/j.cell.2021.08.035.
184. Helmlinger G, Netti PA, Lichtenbeld HC, Melder RJ, Jain RK. Solid stress inhibits the growth of multicellular tumor spheroids. *Nat Biotechnol*. 1997;15(8):778-83. doi: 10.1038/nbt0897-778.

185. Cheng G, Tse J, Jain RK, Munn LL. Micro-environmental mechanical stress controls tumor spheroid size and morphology by suppressing proliferation and inducing apoptosis in cancer cells. *PLoS One*. 2009;4(2):e4632. Epub 20090227. doi: 10.1371/journal.pone.0004632.
186. Delarue M, Montel F, Vignjevic D, Prost J, Joanny JF, Cappello G. Compressive stress inhibits proliferation in tumor spheroids through a volume limitation. *Biophys J*. 2014;107(8):1821-8. doi: 10.1016/j.bpj.2014.08.031.
187. Taubenberger AV, Girardo S, Traber N, Fischer-Friedrich E, Krater M, Wagner K, et al. 3D Microenvironment Stiffness Regulates Tumor Spheroid Growth and Mechanics via p21 and ROCK. *Adv Biosyst*. 2019;3(9):e1900128. Epub 20190724. doi: 10.1002/adbi.201900128.
188. Desmaison A, Frongia C, Grenier K, Ducommun B, Lobjois V. Mechanical stress impairs mitosis progression in multi-cellular tumor spheroids. *PLoS One*. 2013;8(12):e80447. Epub 20131203. doi: 10.1371/journal.pone.0080447.
189. Musgrove EA, Caldon CE, Barraclough J, Stone A, Sutherland RL. Cyclin D as a therapeutic target in cancer. *Nat Rev Cancer*. 2011;11(8):558-72. Epub 20110707. doi: 10.1038/nrc3090.
190. Nelsen CJ, Kuriyama R, Hirsch B, Negron VC, Lingle WL, Goggin MM, et al. Short term cyclin D1 overexpression induces centrosome amplification, mitotic spindle abnormalities, and aneuploidy. *J Biol Chem*. 2005;280(1):768-76. Epub 20041026. doi: 10.1074/jbc.M407105200.

191. Wang TC, Cardiff RD, Zukerberg L, Lees E, Arnold A, Schmidt EV. Mammary hyperplasia and carcinoma in MMTV-cyclin D1 transgenic mice. *Nature*. 1994;369(6482):669-71. doi: 10.1038/369669a0.
192. Lee RJ, Albanese C, Fu M, D'Amico M, Lin B, Watanabe G, et al. Cyclin D1 is required for transformation by activated Neu and is induced through an E2F-dependent signaling pathway. *Mol Cell Biol*. 2000;20(2):672-83. doi: 10.1128/MCB.20.2.672-683.2000.
193. Yu Q, Geng Y, Sicinski P. Specific protection against breast cancers by cyclin D1 ablation. *Nature*. 2001;411(6841):1017-21. doi: 10.1038/35082500.
194. Desai KV, Xiao N, Wang W, Gangi L, Greene J, Powell JI, et al. Initiating oncogenic event determines gene-expression patterns of human breast cancer models. *Proc Natl Acad Sci U S A*. 2002;99(10):6967-72. doi: 10.1073/pnas.102172399.
195. Martins MM, Zhou AY, Corella A, Horiuchi D, Yau C, Rakhshandehroo T, et al. Linking tumor mutations to drug responses via a quantitative chemical-genetic interaction map. *Cancer Discov*. 2015;5(2):154-67. Epub 20141212. doi: 10.1158/2159-8290.CD-14-0552.
196. Debnath J, Mills KR, Collins NL, Reginato MJ, Muthuswamy SK, Brugge JS. The role of apoptosis in creating and maintaining luminal space within normal and oncogene-expressing mammary acini. *Cell*. 2002;111(1):29-40. doi: 10.1016/s0092-8674(02)01001-2.
197. Ring D, Hubble R, Kirschner M. Mitosis in a cell with multiple centrioles. *J Cell Biol*. 1982;94(3):549-56. doi: 10.1083/jcb.94.3.549.

198. Quintyne NJ, Reing JE, Hoffelder DR, Gollin SM, Saunders WS. Spindle multipolarity is prevented by centrosomal clustering. *Science*. 2005;307(5706):127-9. doi: 10.1126/science.1104905.
199. Bakhoun SF, Thompson SL, Manning AL, Compton DA. Genome stability is ensured by temporal control of kinetochore-microtubule dynamics. *Nat Cell Biol*. 2009;11(1):27-35. Epub 20081207. doi: 10.1038/ncb1809.
200. Le Berre M, Zlotek-Zlotkiewicz E, Bonazzi D, Lautenschlaeger F, Piel M. Methods for two-dimensional cell confinement. *Methods Cell Biol*. 2014;121:213-29. doi: 10.1016/B978-0-12-800281-0.00014-2.
201. Ben-David U, Amon A. Context is everything: aneuploidy in cancer. *Nat Rev Genet*. 2020;21(1):44-62. Epub 20190923. doi: 10.1038/s41576-019-0171-x.
202. Nam S, Gupta VK, Lee HP, Lee JY, Wisdom KM, Varma S, et al. Cell cycle progression in confining microenvironments is regulated by a growth-responsive TRPV4-PI3K/Akt-p27(Kip1) signaling axis. *Sci Adv*. 2019;5(8):eaaw6171. Epub 20190807. doi: 10.1126/sciadv.aaw6171.
203. Godinho SA, Picone R, Burute M, Dagher R, Su Y, Leung CT, et al. Oncogene-like induction of cellular invasion from centrosome amplification. *Nature*. 2014;510(7503):167-71. Epub 20140413. doi: 10.1038/nature13277.
204. Cosenza MR, Cazzola A, Rossberg A, Schieber NL, Konotop G, Bausch E, et al. Asymmetric Centriole Numbers at Spindle Poles Cause Chromosome Missegregation in Cancer. *Cell Rep*. 2017;20(8):1906-20. doi: 10.1016/j.celrep.2017.08.005.

205. Garrett S, Auer K, Compton DA, Kapoor TM. hTPX2 is required for normal spindle morphology and centrosome integrity during vertebrate cell division. *Curr Biol.* 2002;12(23):2055-9. doi: 10.1016/s0960-9822(02)01277-0.
206. Gergely F, Draviam VM, Raff JW. The ch-TOG/XMAP215 protein is essential for spindle pole organization in human somatic cells. *Genes Dev.* 2003;17(3):336-41. doi: 10.1101/gad.245603.
207. Carter SL, Eklund AC, Kohane IS, Harris LN, Szallasi Z. A signature of chromosomal instability inferred from gene expression profiles predicts clinical outcome in multiple human cancers. *Nat Genet.* 2006;38(9):1043-8. Epub 20060820. doi: 10.1038/ng1861.
208. Hanahan D, Weinberg RA. Hallmarks of cancer: the next generation. *Cell.* 2011;144(5):646-74. doi: 10.1016/j.cell.2011.02.013.
209. Schindelin J, Arganda-Carreras I, Frise E, Kaynig V, Longair M, Pietzsch T, et al. Fiji: an open-source platform for biological-image analysis. *Nat Methods.* 2012;9(7):676-82. Epub 20120628. doi: 10.1038/nmeth.2019.
210. Godek KM, Kabeche L, Compton DA. Regulation of kinetochore-microtubule attachments through homeostatic control during mitosis. *Nat Rev Mol Cell Biol.* 2015;16(1):57-64. Epub 20141203. doi: 10.1038/nrm3916.
211. Knouse KA, Lopez KE, Bachofner M, Amon A. Chromosome Segregation Fidelity in Epithelia Requires Tissue Architecture. *Cell.* 2018;175(1):200-11 e13. Epub 2018/08/28. doi: 10.1016/j.cell.2018.07.042.

212. Jagric M, Risteski P, Martincic J, Milas A, Tolic IM. Optogenetic control of PRC1 reveals its role in chromosome alignment on the spindle by overlap length-dependent forces. *Elife*. 2021;10. Epub 20210122. doi: 10.7554/eLife.61170.

Publishing Agreement

It is the policy of the University to encourage open access and broad distribution of all theses, dissertations, and manuscripts. The Graduate Division will facilitate the distribution of UCSF theses, dissertations, and manuscripts to the UCSF Library for open access and distribution. UCSF will make such theses, dissertations, and manuscripts accessible to the public and will take reasonable steps to preserve these works in perpetuity.

I hereby grant the non-exclusive, perpetual right to The Regents of the University of California to reproduce, publicly display, distribute, preserve, and publish copies of my thesis, dissertation, or manuscript in any form or media, now existing or later derived, including access online for teaching, research, and public service purposes.

DocuSigned by:

16AEDBE12D244BA... Author Signature

5/24/2023
Date